SLAC TRANS - 68

One-Pion Photo Production of Positively Charged Pi-Mesons
Between 1.2 and 3 GeV in the Laboratory Angular Range from 8° to 20°

(Photoeinfachproduktion positiv geladener Pi-Mesonen
zwischen 1.2 und 3 GeV im Laborwinkelbereich von 8° - 20°)

by

P. Schmuser
State Institute of Physics
Second Institute for Experimental Physics, Hamburg

TRANSLATED FOR
STANFORD LINEAR ACCELERATOR CENTER

One-Pion Photo Production of Positively Charged Pi-Mesons

between 1.2 and 3 GeV in the Laboratory Angular Range from 8° to 20° *

by

P. Schmuser

State Institute of Physics

Second Institute for Experimental Physics, Hamburg

Abstract

The reaction $\gamma + p \rightarrow \pi^{+} + n$ has been investigated for incident photon energies between 1.2 and 3 GeV and pion production angles between 8 and 20 degrees in the lab system. The differential cross sections $d\sigma/d\Omega^{*}$ show resonance structure in the energy region corresponding to the nucleon isobars $N^{*}_{3/2}(1920)$ and $N^{*}_{1/2}(2190)$. At photon energies above 1.7 GeV, the cross sections $d\sigma/dt$ drop nearly exponentially as functions of four-momentum transfer.

Presently existing theoretical models are only partly successful in describing the experimental behaviour. The simple peripheral model (gauge invariant one-pion exchange) predicts a t-dependence with strictly disagrees with the results of this experiment. If final-state absorption is taken into account the situation is considerably improved, but still the decrease of $d\sigma/dt$ with $|t|$ is less rapid than experimentally observed. However, this absorption model gives the correct order of magnitude for the cross sections.

Interpretation in terms of Regge-π-exchange does not seem to be adequate since there is still resonance structure in the energy region considered.

The vector-meson dominance model predicts values for the total cross sections which agree with the experimental results within a factor of two. Also a predicted t-dependence at 1.7 GeV is in qualitative agreement with this experiment.

Index

I. Introduction

Pion photo production in the low energy range between the 150 MeV threshold and about 800 to 1000 MeV is substantially dominated by pion nucleon resonances [1]. Specifically, the first resonance $N^*_{3/2}$ (1236) with spin and isospin 3/2 manifests itself in a very large total effective cross section of π^+ and π^0 photo production at photon energies in the vicinity of 300 to 330 MeV. The behavior up to these energy levels is described satisfactorily by the dispersion theory proposed by Chew, Goldberger, Low and Nambu [2]. Measurements at higher energy levels [3, 4] also show advantage factors in the π^+ effective cross section near higher resonance values, specifically of the N*(1518), however much less pronounced. Yet, one may expect that as the energy increases, the effect of the resonances decreases since the maximum classical angular momentum possible $L \approx kR$ (where k = photon energy, R = range of interaction) is large with respect to unity, so that the probability that the photon-nucleon system be found in a defined angular momentum state decreases. It is furthermore shown experimentally that in photo production in the GeV range the pions are produced primarily at small angles near the forward direction. This is not compatible with the angular decay distribution of a resonance and is difficult to understand due to the interference of several resonances. In contrast, the preference for a small production angle becomes quite plausible if peripheral interactions with large impact parameters and low pulse transmissions to the nucleon are assumed. Therefore, the

peripheral model which approaches the scattering amplitude by contributions of single particle exchanges, is said to provide a reasonable description. Specifically, the one-pion exchange should play a major role since the pion, as the lightest exchangeable particle, provides the greatest range of the interaction.

Photo production measurements in the GeV range heretofore were only available from groups working at Caltech [5,6,7] and CEA [Central Electricity Authority] [8. 9. 10]. The measurements made by Walker et al [5,6] terminate at an energy of 1.4 GeV. For a small series of energy values, these authors photographed complete angular distributions. For the theoretical interpretation of their data, Walker et al used a method indicated by Moravcsik [11] in which the effective cross sections are matched following the separation of a resonance denominator by a polynomial in $\cos \theta^*$ (θ^* is the production angle of the pion in the center-of-mass system). In this way, an interference between the one-pion exchange terms and other terms can be detected, for example, nucleon pole terms; furthermore, by extrapolating the polynomial series toward the pole of the one-pion exchange at $\cos \theta^* = \frac{1}{\beta}$ (β = velocity of the pion in the center-of-mass system) the pion-nucleon coupling constant can be determined. Values were thus obtained for the coupling constant which are compatible with that known from the pion-nucleon scattering but which present relatively large errors.

The measurements obtained by Osborne et al [8,9,10] were con-

ducted at considerably higher energy levels (above 3.4 GeV) however, they only cover a range of large production angles while the essential evidence provided by the peripheral model, particularly the one-pion exchange, concerns small angles. In the CEA measurements it was shown that the higher resonance values possibly play a role, but that they are only visible as a small structure against a background so that other mechanisms are probably required to describe photo production.

In the present study, measurements of the π^+ photo production in a photon energy range from 1.20 to 3 GeV and in a pion laboratory angular range from 8° to 20° will be described corresponding to center-of-mass angles ranging from 15° to 50°. In the discussion of the effective cross sections, results of a later study will also be referred to which continued the investigation down to very small angles (1.1° in the laboratory and 2.5° in the center-of-mass system) [12]. This is designed to provide a critical test of the evidence yielded by the peripheral model and its expansions (absorption model) as well as of the Regge Pole model for the π photo production up to energy levels of 3 GeV. Disregarding some low energy values (1.20, 1.34 GeV) in which there was an overlap with Caltech, an energy and angular range was covered which was heretofore unknown. In order to provide a connection with the Osborne measurements, several points were photographed with γ energy of 3.25 GeV and at large laboratory angles.

II. Experimental Arrangement

II.1) Summary

1.1) Principle of the Measurement Arrangement

As in most photo production measurements, the work is performed here with the continuous energy spectrum of photons produced during the moderation of mono-energetic electrons in the coulomb field of a nucleus. Since the effective cross section of the photo production reaction is to be determined for a defined photon energy value, a means to determine the energy must be found. One method consists of producing the retardation quanta for two different measurement series by means of electrons with different energy values E_1 and $E_2 > E_1$, and to subtract the pion counting rates from each other so that only the events produced in the photon energy interval $E_1 \leq E \leq E_2$ remain. As in any subtraction method, considerable chances result. It is considerably more elegant to utilize the fact that in a two-body reaction of the type

$$\gamma + p \rightarrow \pi^+ + n \tag{1}$$

the entire kinematics are defined by the two following values: the production angle Θ and impulse p of the pion (Appendix 1). If other reactions can be ruled out safely, it is thus sufficient to detect only the pion and to measure its angle and impulse. The energy of the γ quantum which triggered the reaction described in Eq. (1), can then be calculated in accordance with Appendix 1, Eq. (A5).

Competing processes which also produce π^+ mesons are mostly

multiple-production processes of the form

$$\gamma + p \rightarrow \pi^+ + n + \pi^o + \ldots$$
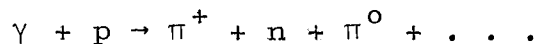
Since in this case, however, a minimum additional pion mass

must be added, the required γ energy is at least 140 MeV higher

for the same angle and impulse of the π^+, or in other words:

If we start with photons of the same energy content, the impulse

of the π^+ is at least 140 MeV / c lower in multiple production

than in one-pion production (1). Fig. 1 shows the relationship

between the impulse and the production angle of the π^+ fixed

γ energy value of 2 GeV for one-pion production (1) and the

energywise adjacent multiple reaction

$$\gamma + p \rightarrow \pi^+ + (n + \pi^o) \tag{2}$$

The curve $p(\theta)$ for the reaction shown in Eq. (2) always lies

about 150 MeV/c below that for the reaction shown in Eq. (1).

Therefore, if we assume a minimum value p_{min} of the impulse for

the pion, so that in Eq. 1 the corresponding γ energy is closer

than 150 MeV to the upper limit of the γ-ray spectrum (retar-

dation edge), the pions of Eq. 2 are no longer included since

they remain below the minimum value of the impulse $E_\gamma \leq E_{\gamma max}$

other positively charged particles as positrons, protons, K^+

mesons, may be ruled out either by electronic methods or for

kinematic reasons (cf. 5.2).

The measurement principle applied in the present experiment can
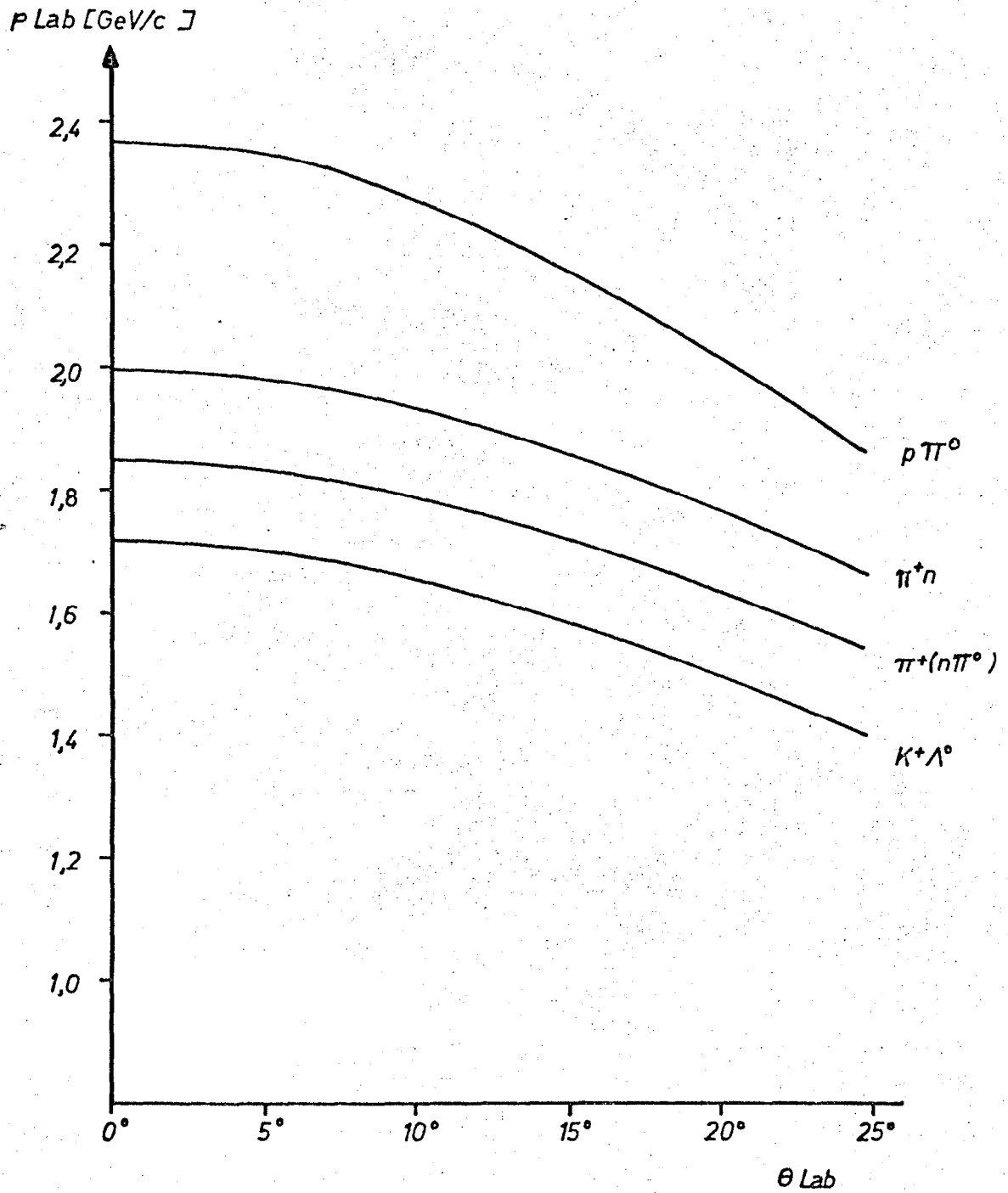
Fig. 1: Photo production kinematics for $E_\gamma = 2$ GeV

$$\gamma + p \rightarrow \begin{cases} p + \pi^0 \\ \pi^+ + n \\ \pi^+ + (n + \pi^0) \\ K^+ + \Lambda^0 \end{cases}$$
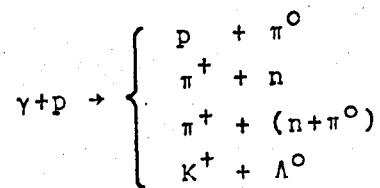
now be characterized as follows: Using a magnetic spectrometer, the impulse and production angle of the positively charged pions are measured. The spectrometer is so adjusted that the lower limit of the pulse band is still above the p_{min} value defined earlier. Consequently only on-pion production can be safely said to be involved [1] and therefore, the γ energy can be calculated exactly from the values p_π, Θ_π. In the final effect, this corresponds to a differential determination of the γ energy. A sufficiently good pulse and angle resolution capacity of the spectrometer is a prerequisite for this measurement method. Specifically, the resulting resolution in γ energy must be considerably better than the distance to the multiple production of 150 MeV.

1.2) Survey of Experimental Setup

Fig. 2 shows the experimental setup. The γ-ray produced at an internal target of the synchrotron is brought into interaction with the protons of a hydrogen target. The charged particles thus produced are detected in a magnetic spectrometer which can be swung around the hydrogen target on a mount. It is then detected by a scintillation counter and a scintillation hodoscope and classified according to production angle, impulse and type of particle. The detailed information for each particle recorded by the counters is stored by a PDP-5 computer and recorded on a magnetic tape. The arrangement shown here was used for measuring the π^+ photo one-pion production in the laboratory angular range from $8°$ to $20°$ and in the energy range from 1.2 to 3.0 GeV. The

Fig. 2: Experimental Setup

(Schematic)
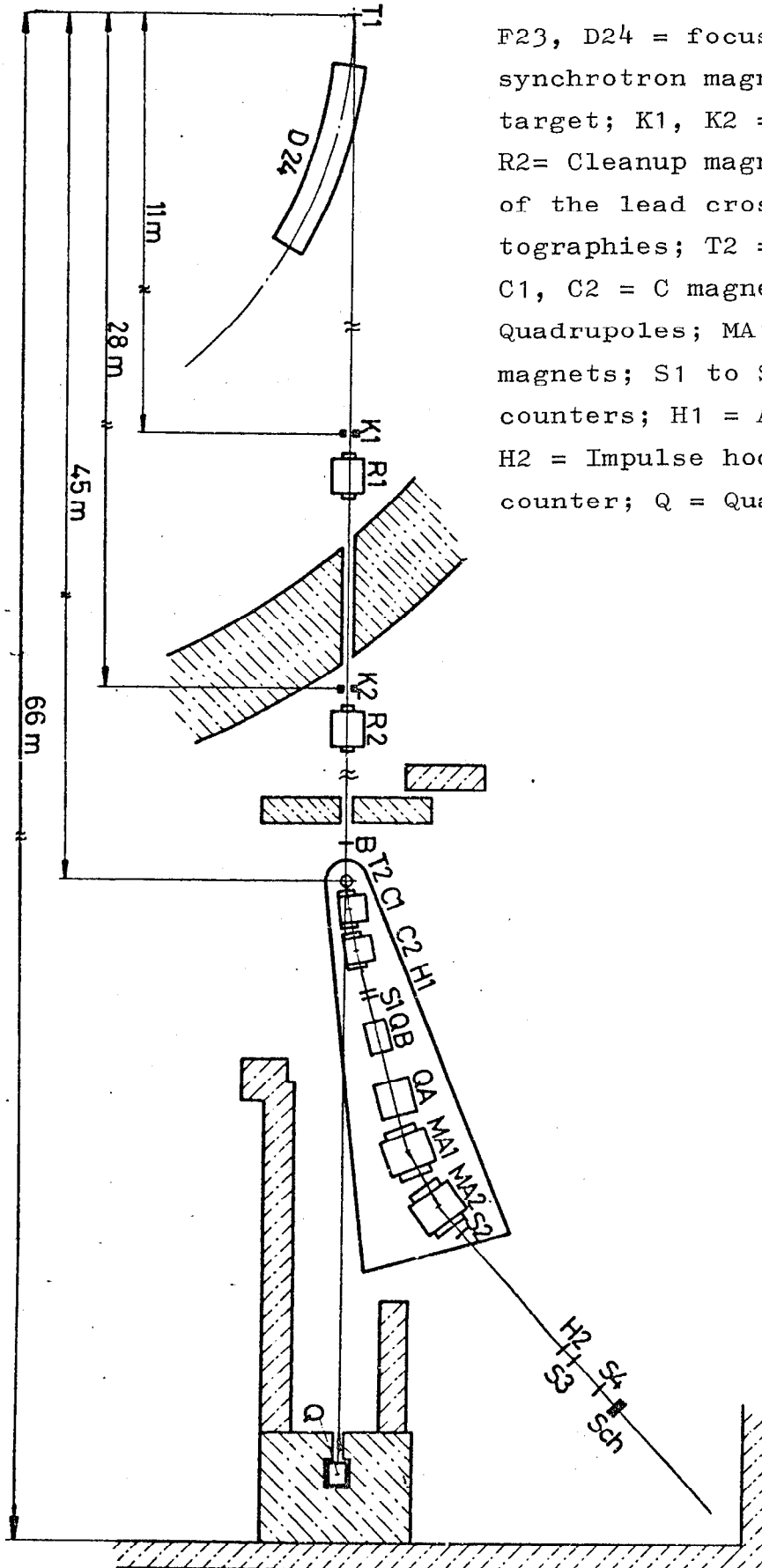
F23, D24 = focusing and defocusing synchrotron magnet; T_1 = Tantalum target; K1, K2 = Collimators; R1, R2 = Cleanup magnets; B = position of the lead cross during beam photographies; T2 = Hydrogen target; C1, C2 = C magnets; QB, QA = Quadrupoles; MA1, MA2 = Deflection magnets; S1 to S4 = Scintillation counters; H1 = Angular hodoscope; H2 = Impulse hodoscope; Sch = shower counter; Q = Quantameter.

setup used to extend the measurements to small angles is de-
scribed in detail in Reference 12. Furthermore, a spectrometer
was used to detect photo production of anti-protons [13].

II.2) The γ Beam

2.1) Setup and Beam Guidance

The electrons accelerated are guided at an energy maximum toward
a target located in the straight section 24 of the device where
they produce bremsstrahlung [retardation radiation]. In most
cases, a tantalum plate whose thickness is 0.125 or 0.06 radia-
tion lengths thich is used. The electron beam is made to turn
by the controlled deformation of the particle trajectory, using
pulse magnets (beam bump). An attempt is made to guide the beam
slowly over many electron revolutions to the target so that a γ
beam impulse (spill) of several 100 μs up to 1 ms duration is
produced. A distribution of the essentially assumed total in-
tensity over a time period which is not to be too short is there-
fore important so that the problems of accidental coincidences in
the electronics do not become excessive. The upper limit of the
γ-ray pulse is set by the energy sharpness required by the ex-
periment (see Section 2.3).

The γ-ray leaves the synchrotron through a special outlet cham-
ber with a thin titanium window and is limited by two lead
collimators K1 (K2), (Fig. 2), whose thickness is 30 cm and
whose opening is 8 mm (24 mm) wide and 4 mm (12 mm) high. The
collimators are followed by the respective cleanup magnets which

remove charged particles from the beam. Shortly before the
hydrogen target, the γ beam passes a vacuum and from there to
the quantameter it passes through air. The quantameter itself
is built into concrete to reduce back scattering and can be
reached by the beam only through a narrow channel.

2.2) γ-ray Adjustment

The target to produce the bremsstrahlung is located on the inside
of the reference trajectory of the electrons behind the focusing
synchrotron magnet F23 which bunches the electron beam into a
convergent bundle. Since the inclinations of the electron tra-
jectories increase toward the beam axis as the distance from the
reference trajectory increases, the direction of the γ beam be-
comes a function of the target position. Measurements made with
polaroid film showed a change in direction of 0.165 ± 0.02 mrad
per mn target shaft, and the theoretical value for this condi-
tion is 0.156 mrad/mm [14]. Furthermore, measurements were
made with an ionization chamber located in the ring to deter-
mine the intensity yield as a function of target position. Using
the beam bump and frequency modulation (the acceleration paths
were detuned by 40 kc with respect to the linear accelerator)
the yield became constant in a range of 41 to 29 mm in the tar-
get position [14] (distance from the reference trajectory).
This provided the possibility of changing the direction by about
2 mrad without loss of intensity so that in spite of the limited
adjustability of the mount pivot it was possible to adjust the
quantameter, the mount pivot and beam duct, using the screening

wall of the synchrotron, to the γ-ray axis obtained for the target position 30 mm. In the course of one year only small corrections of up to a maximum of 1 mm target shift was required. The collimators are adjusted symmetrically to the reference axis using X-ray films.

Fig. 3 shows a typical example of a beam photo made by the quantameter

2.3) Energy Definition of the γ Beam

Electrons which are not guided exactly at the point in time t_{max} of the maximum acceleration toward the target, have a clearly defined deviation from their maximum energy which can be computed from the time response of the field intensity in the synchrotron magnets. The retardation edge shifts at the same rate. If an energy indeterminancy of $\pm$ 0.5 % max. is tolerated, the γ-ray pulse can only be produced in a time interval of $\pm$ 700 μs-difference from t_{max}. Control over the correct time position is provided by several signals provided by the control center of the synchrotron during each experiment. An impulse defining the maximum acceleration (t_{max}) as well as count pulses per MeV energy change of the electrons permit opening up the electronics of the experiment for a given time interval difference from the t_{max} pulse and thus to reject particles with excessive energy deviation values.

2.4) Intensity Measurement

The total energy of the γ-ray is measured with a gas-filled quantameter which differs in some details [16] from the Wilson
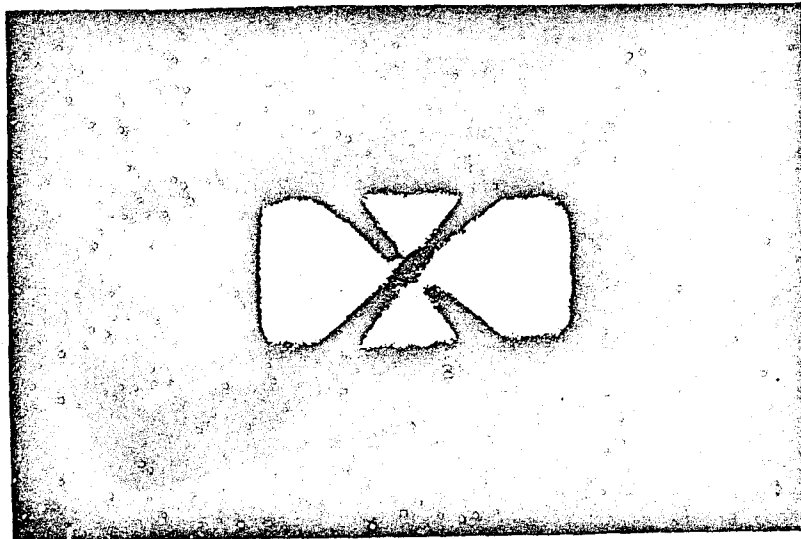
Fig. 3: Example of a Gamma-ray photograph.
Polaroid X-ray film type 3000 X, 1.5 mm Cu converter.
The film was located about 2 m ahead of the quantameter,
The rectangular edge is the picture of the 8 mm x 4 mm
collimator K1, the diagonal cross is the picture of a
lead cross located at position B in Fig. 2, which is
adjusted to the reference axis. Since the collimator
appears to be enlarged by its distance from the pro-
duction target T1 and since the lead cross is clearly
shown, it may be concluded that an almost point-shaped
source of the γ-ray is involved.

gamma-meter [15]. According to the equation

$$E_{total} = \int_0^{k_{max}} k \ N(k)dk = Q_{eff} \cdot k_{max}$$

the number of "effective quanta" can be computed. In the DESY quantameter No. 2 used, calibration measurements at the outer electron beam [16, 17] yielded a calibration constant of $3.35 \cdot 10^{18}$ MeV/Coul $\pm$ 3%. The total uncertainty in the quantameter constant must be rated at about $\pm$ 5% due to possible saturation effects produced.

The output current of the quantameter is smoothed out to prevent overload effects resulting from the short pulse width-repetion ratio with an RC member amplified in a computer amplifier and transferred to an integrating amplifier.

2.5) Monitoring Telescope

Due to the low current levels, the quantameter electronics cannot be gated similar to the electronics of the experiment for only a given time interval. If only a part of the γ intensity lies outside this interval, the quantameter integrator indicates too much charge compared to the particle rate demonstrated. In order to be able to correct this effect, a telescope was mounted ahead of the quantameter consisting of three scintillation counters. In this telescope, the electrons and positrons produced by the γ-ray in a 3 mm thick polyethylene target are detected. For a given synchrotron energy value, the coincidence count rate of the monitoring telescope should be proportional to the total charge indicated by the quantameter.

The count rate of the monitoring telescope is recorded by two electronic counters of which one is gated exactly like the spectrometer electronics while the other is open like the quantameter electronics for the duration of the entire measurement process. The ratio of these count rates is precisely the correction to be applied to the quantameter indication. In most cases, the difference in the count rate is only several thousandths.

II.3) The Hydrogen Target

The hydrogen target is mounted above the pivot of the mount. The actual reaction container is an upright cylinder whose diameter is 69.8 ± 0.2 mm and which is 14 cm high, consisting of 75 μ polyimide foil (H foil made by DuPont) cemented to end flanges made of V2A. The cement consists of a mixture of 50% Shell epikote 828 and 50% Schering versamide 125 at 80° C under pressure. The cell has separate gas exhausts and fill lines. The fill line reaches down to the bottom of the cell so that it can be emptied if helium gas is introduced under pressure in the cell gas exhaust line. This provided for consecutive full and empty target measurements without wasting time. The hydrogen reservoir and the cell are surrounded by a radiation shield cooled with liquid nitrogen. Two holes are provided for the free passage of the γ-ray and the particles to be detected. For a well-cooled target and a vacuum of $1 \cdot 10^{-6}$ torr, the hydrogen consumption was 130 cm^3/hr.

The built-in controls consist of a capacitive fill indicator

for the hydrogen reservoir as well as an acoustic warning signal which goes off whenever the vacuum goes below 10^{-5} torr or in case of power failure. The beam entrance and exit windows are made of 200 μ-thick hostaphan foil.

II.4) The Magnetic Spectrometer

4.1) Construction

The spectrometer used to measure the impulse and angle of the particle produced consists of six magnetic elements. Two C magnets, C1, C2, built on the principle of the synchrotron magnets, bend the particle beam away from the γ-ray and produce an angle focus in the horizontal plane. They are followed by two quadrupoles QB, QA, which form images of the focus produced by the C magnets and two deflection magnets MA1, MA2, for pulse dispersion. All magnets are mounted on a swinging mount which rotates about the target center.

4.2) Focusing Characteristics

The C magnets focus in the horizontal and defocus in the vertical plane. At a distance of 4 m from the hydrogen target they produce an angular focus (θ focus) i.e. particles of the same emission angle and the same impulse pass through one point, even if they were produced at different points on the target. An optical analogue would be a convergent lense (cylinder lense) which focuses parallel rays in the focus plane (Fig. 4a).

In addition to focusing, the C magnets produce a deflection of the charged particle beam from the γ-ray. For an optical analogy, it is produced by the fact that the aim is not symmet-

rical to the axis but eccentrically through the lense (Fig. 4b). This deflection effect is slightly dependent on the pulse so that a line in the Θ-p diagram of the spectrometer corresponds to a point in the angle focus, which is somewhat different from a straight-line Θ = const (see Fig. 6). The angle focus provides a major advantage in that very accurate angular measurements are obtained in spite of an enlarged primary beam and thus a non-point-shaped target, which is required in photo production based on intensity considerations.

The angle focus image is formed by the "highly" focusing doublet QB (horizontal defocusing) and QA (horizontal focusing) at a distance of 20 m from the target. In the vertical plane, there is another focus. In the horizontal plane, one obtains a twofold enlarged picture of the angle focus shifted laterally by the MA magnets which produce a total deflection of 30°.

The second focus, the impulse focus (or p focus) is simply an inverse image of the angle focus when the deflection magnets are disconnected. The deflection effect shifts this picture at different rates, depending on the particle impulse. A point in this focus therefore measures a linear combination of angle and impulse. If the particle production angle premitted to increase, its piercing point in the p focus migrates toward the γ-ray. If the old piercing point is to be re-established, the pulse must be reduced (cf. Fig. 5). A fixed point in the p focus therefore corresponds to a decaying curve in a Θ-p diagram.

a)

$\theta_o + \Delta\theta$

θ_o

$\theta_o - \Delta\theta$

target   angle focus

b)
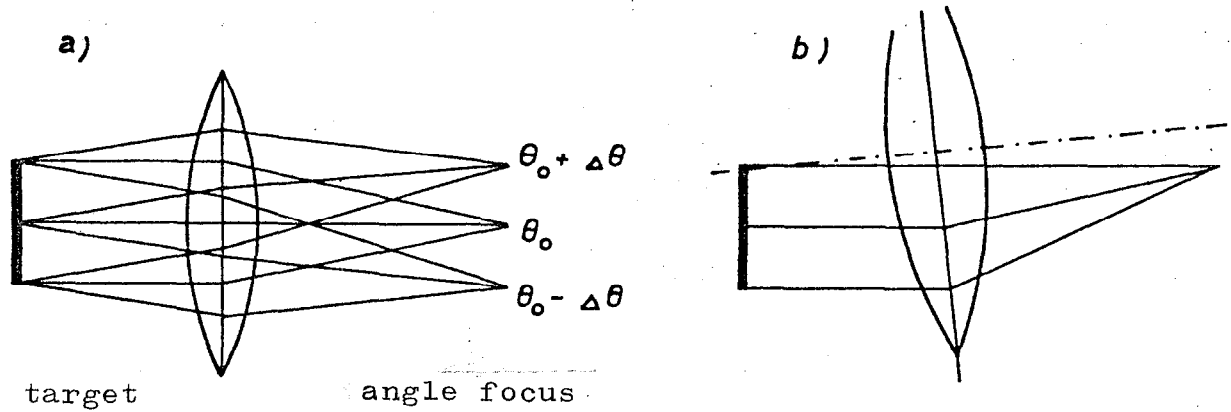
Fig. 4: a) Focusing characteristics of the C magnet in the horizontal plane

b) Focusing and deflection effect for eccentric targeting.

$P_o, \theta_o - \Delta\theta$

P_o, θ_o

$P_o - \Delta p, \theta_o + \Delta\theta$

$P_o, \theta_o + \Delta\theta$

$\theta_o + \Delta\theta$

θ_o

$\theta_o - \Delta\theta$

angle focus   Quadrupole

Impuls-fokus

deflection magnet
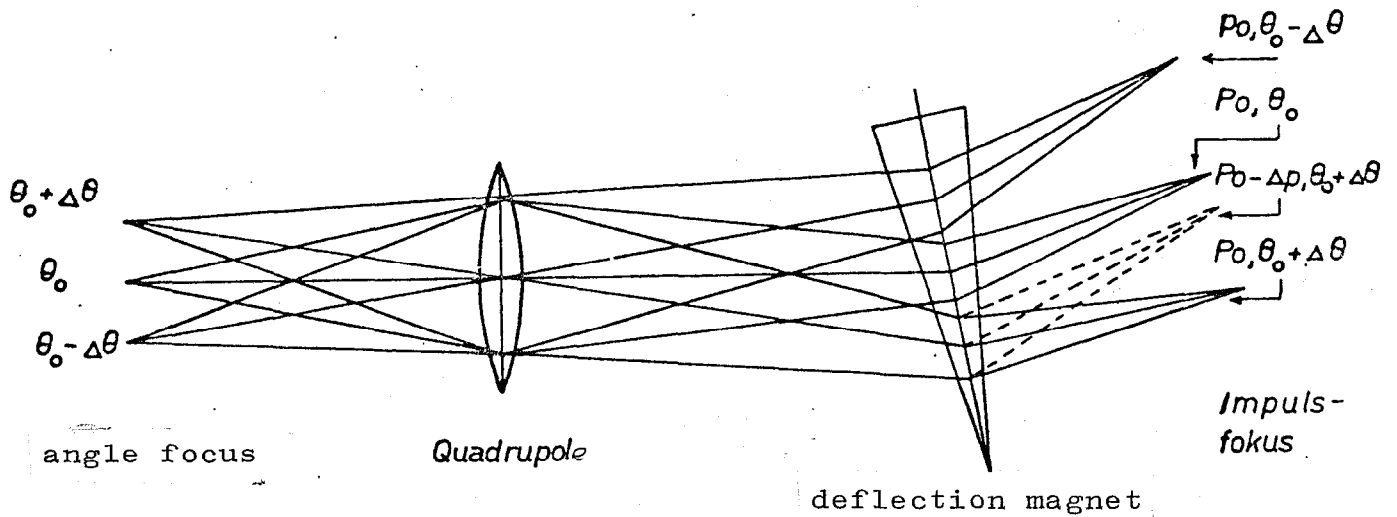
Abb. 5: Abbildung des Winkelfokus auf den "Impulsfokus". Korrelation zwischen Winkel und Impuls in diesem Fokus.

Fig. 5: Angle focus image on the impulse focus. Correlation between angle and impulse in this focus.

fixed point in the angle focus

fixed point in the impulse focus
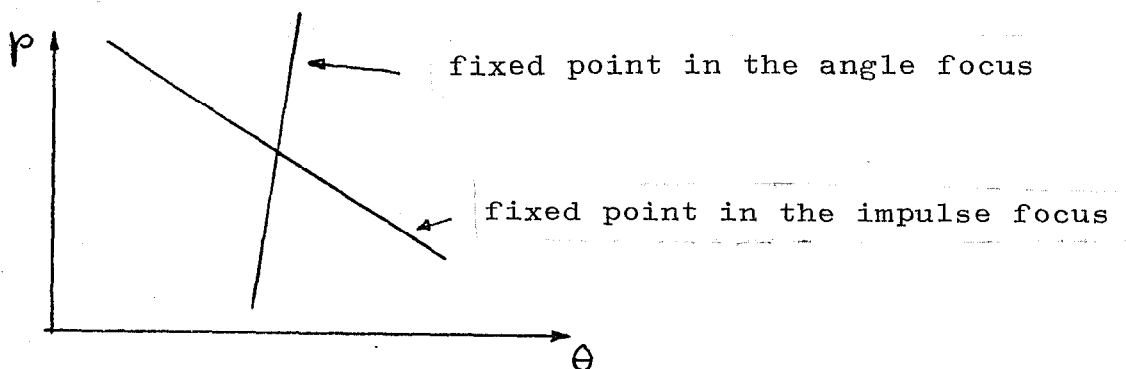
Fig. 6: θ-p Diagram of the spectrometer

If we measure the piercing points of the particle trajectory in the θ and p focus using a counter hodoscope, the angle as well as the impulse are clearly defined by these two values in accordance with Fig. 6. The slope of the curve representing the "fixed point in the p focus" in a θ-p diagram is affected by the amount of dispersion in the deflection magnets; it will evidently become flatter, the more pronounced the dispersion.

A spectrometer of the type described is called a "tilted-window spectrometer" since a tilted band is defined in the θ-p plane by a small verticle aperture (counter) in the impulse focus which characterizes the acceptance of this apperture.

From the dynamics of π^+ photo production we note that for a constant γ energy level the function p (θ) of the pion describes a
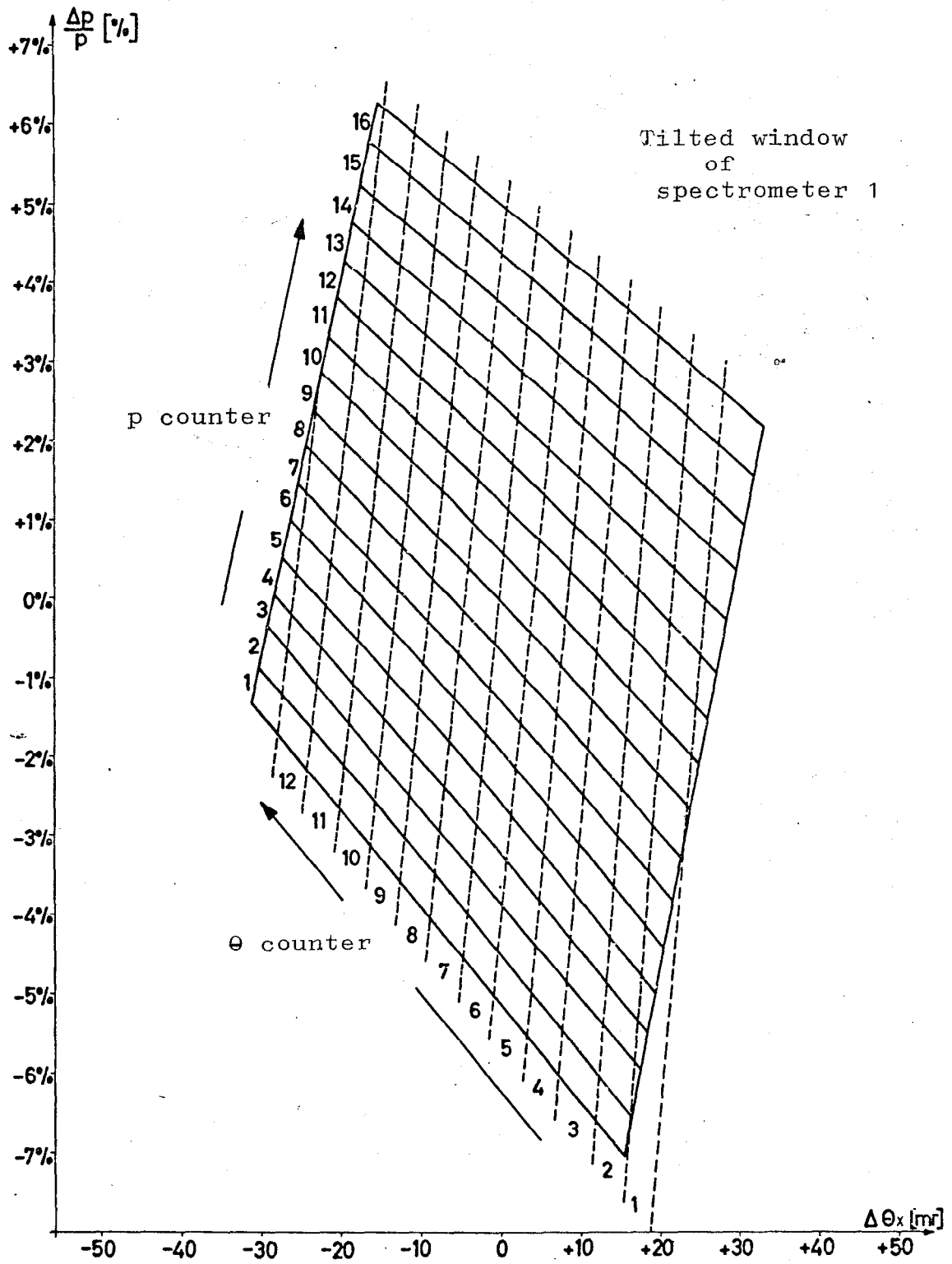
Fig. 7: Limits of the angle and impulse hodoscope counters in a Θ-p diagram

curve of similar slope for angles which are not too small (Fig. 1).
If we succeed in adapting the slope of the tilted window to that
of the dynamic curves, a minimum γ energy interval falls into a
preset aperture in the impulse focus. The impulse focus would
be described more accurately as a γ energy focus in π^+ photo pro-
duction. Despite the series connection between two deflection
magnets, however, the dispersion is insufficient to attain a
complete adaptation of the slopes, particularly for exceedingly
small angles where the dynamic curves tend to be flatter.

4.3) Resolution and Acceptance

For an accurate definition of the particle trajectories at the
angle and impulse focus, scintillation counter hodoscopes are
installed there consisting of 12 counters 1 cm wide and 16
counters 2 cm wide. Fig. 7 shows the limits of these counters
in a Θ-p diagram. A "coincidence" between a "Θ" and a "p" coun-
ter defines a rhombic "window," which covers an angular width of
$\Delta\Theta = \pm 2$ mrad and a γ energy interval $\Delta k/k = \pm 0.4\%$. The angular
acceptance in the vertical direction is given by counter S1 and
amounts to ± 13 mrad.

The acceptance of such a window, i.e. the product obtained by
multiplying the space angle $\Delta\Omega$ and the pulse band $\Delta p/p_0$, where
p_0 is the average pulse of the spectrometer, was determined
taking into account the multiple scattering in the counters
located in the spectrometer. The total acceptance of the spec-
trometer then results from the summation. It is

$$(\Delta\Omega \ \frac{\Delta p}{p_o}) \ \text{total} = 0.56 \cdot 10^{-4} (\text{sterad}).$$

This also takes into account the finite target extension. A detailed description of the spectrometer construction, the focusing characteristics, the programs for calculating the acceptance and resolution as well as experimental tests is to be found in Reference 18.

II.5) The Counter System

5.1) Definition of the Geometry of the Particle Beam

For a geometric definition of the space angle inclosed, 4 scintillation counters are used: S1 at the directional focus, S2 behind the second deflection magnet, S3 at the impulse focus and S4 1 m behind it. The counter dimensions are so selected that they are adapted to the total beam cross section at the particular point. The latter was determined by drawing the outside particle trajectories on an analogue computer and by using Monte Carlo calculations [18]. Aperture limits are given in the vertical direction by the C magnets and in the horizontal direction primarily by QB and QA. A more accurate definition of the particle trajectory is provided by the hodoscopes at the directional and the pulse focus located directly ahead of S1 and S3 respectively. The counter dimensions and the multiplier types are listed in Table 1: [see next page].

The pulse hodoscope is 4 cm wider than the aperture defining

Table 1: Dimensions of Scintillation Counters

Counters	Width	Height	Thickness	Multiplier
Θ hodoscope	12 @ 1 cm	14 cm	0.5 cm	56 AVP
S1	12	14	0.5	56 AVP
S2	19	14	0.5	56 AVP
p hodoscope	16 @ 2 cm	16	1.0	53 AVP
S3	28	16	1.0	56 AVP
S4	32	16	1.0	56 AVP

counter S3, where by control of the counter line-up is provided.
The end of the counter system is a lead scintillator shower coun-
ter. Between the counters, the beam travels in a helium atmo-
sphere.

The scintillation light is guided toward the photo multipliers in
the trigger counters via laterally mounted light guides. Type B
voltage dividers [19] were used: The high voltages, depending
on scintillator thickness, ranged from 2.2 to 2.4 kV. Output
pulses as narrow and as symmetrical as possible (about 7 nsec
base width) are attained by mounting a pulse-shaping delay cable
at the anode terminated in approximately one-half the character-
istic impedance. Overshoots are removed mainly by means of 30
to 80 ohm damping resistors inserted in the conductors leading
to the last dynodes.

5.2) Particle Discrimination

The spectrometer accepts all positively charged particles which
fall within a certain pulse band for a corresponding pole ar-
rangement. Test measurements with a threshold Cerenkov counter
show that within the angular range of 8° to 20°, the number of
positrons is less than 1% of the number of pions. Therefore, a
positron correction using the shower counter could be eliminated.
From the μ pair production, only a negligible amount of muons
may be expected. The detection probablity for muons resulting
from the π decay will be investigated in section III.3.

Photo produced K^{+} mesons cannot be included since for a given

γ energy their pulse is at least 300 MeV/c below that of the simply produced pions (see Fig. 1), so that they, like the pions obtained from multiple reactions, do not fall within the pulse acceptance of the spectrometer (cf. 1.1).

For protons and simple and multiple π^o production processes, this does not apply. They are separated from the pions by a measurement of the flight time between counters S1 and S3, where they flight time differences amount to 15.5 nsec for 1.2 GeV/c and 2.8 nsec for 2.8 GeV/c.

II.6) High-Speed Electronics

The electronics logic is shown schematically in Fig. 8. A 100 mc Chronetics Nanologic Electronics System is used.

6.1) Electronics Logic for Geometry Defining Counters

When a charged particle passes through the system, scintillation counters S1 through S4 must respond, i.e. the "main coincidence" circuit (1234) must provide an output pulse.

The special arrangement of the spectrometer is characterized by the fact that at least for angle values of 8° and 10° the counter S1 located at the directional focus and the directional hodoscope are hit by a mass of "scatter radiation" (with the background consisting of soft γ quanta and electrons) while the other counter behind the deflection magnets are barely hit.

Intelligent operation with counters at directional focus requires that these be fully screen against direct visual impact by the

a) Main coincidence circuit

Main Coincidence
HK pulse

LIM	Limiter
D	Discriminator
⌣	Coincidence
FF	Flip-flop
⊐	Delay Line

b) Delayed coincidences

$C2 = (23_v)$

$C4 = (1_v 234)$

$C5 = (1234_v)$

c) Flight time electronics

to PDP5
PDP5 reset

„reset" from PDP5
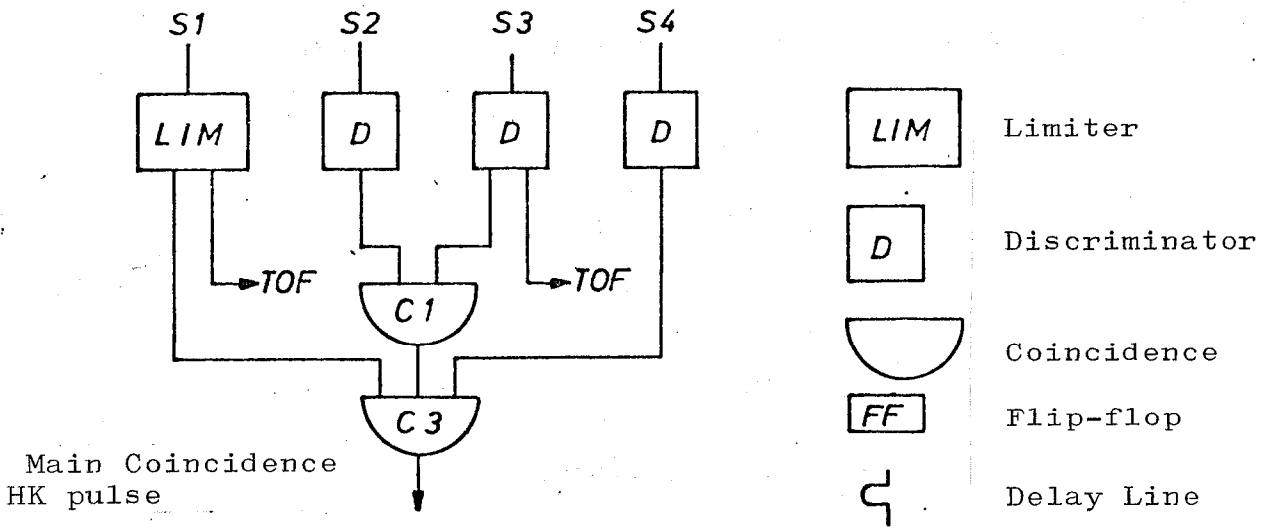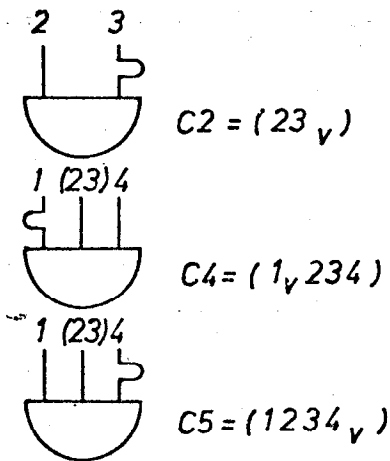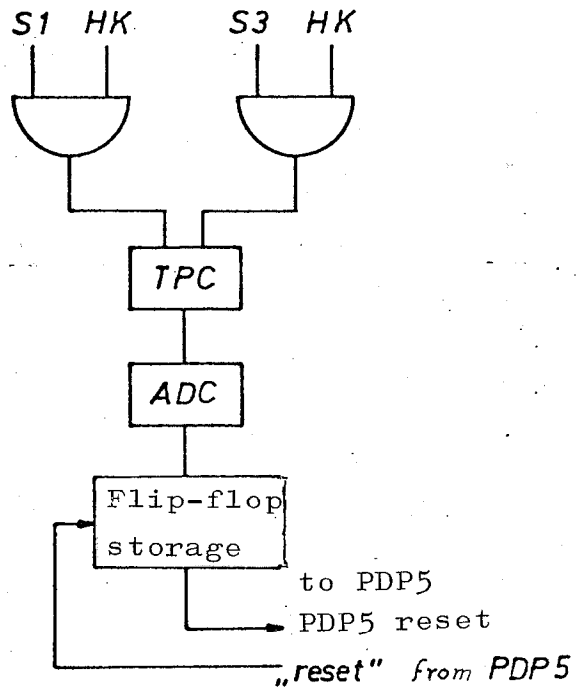
d) Hodoscope electronics

„reset" from PDP5

to PDP5

Fig. 8
Simplified
High-speed
electronics

γ-ray. Even then, a very high individual count rate remains
which requires special treatment of these counters from two view-
points. First, it must be prevented that a "real" particle (pion
or proton) fails to be recorded as a result of a blockage pro-
duced shortly before by a background particle reaching the S1,
thus blocking the electronics for the duration of its "dead time."
If a Chronetics discriminator model 101 is used, the minimum dead
time is about 10 nsec. Consequently, no discriminator is used
for S1 but rather a limitor which has no dead time insofar as it
converts to subsequent photo-multiplier pulses into a single
extended pulse instead of omitting the second pulse as the dis-
criminator would do. In this manner, as a result of the effect
produced by a background particle, the time information of S1
may suffer in quality but the subsequent "real" particle cannot
be lost. Secondly, the high count rates in the S1 and in the
directional hodoscope require sharp coincidences of the main
coincidence pulse with the pulse coming from S1 used to measure
the flight time and with the hodoscope counters, so that both
background in the flight time spectrum as well as multiple events
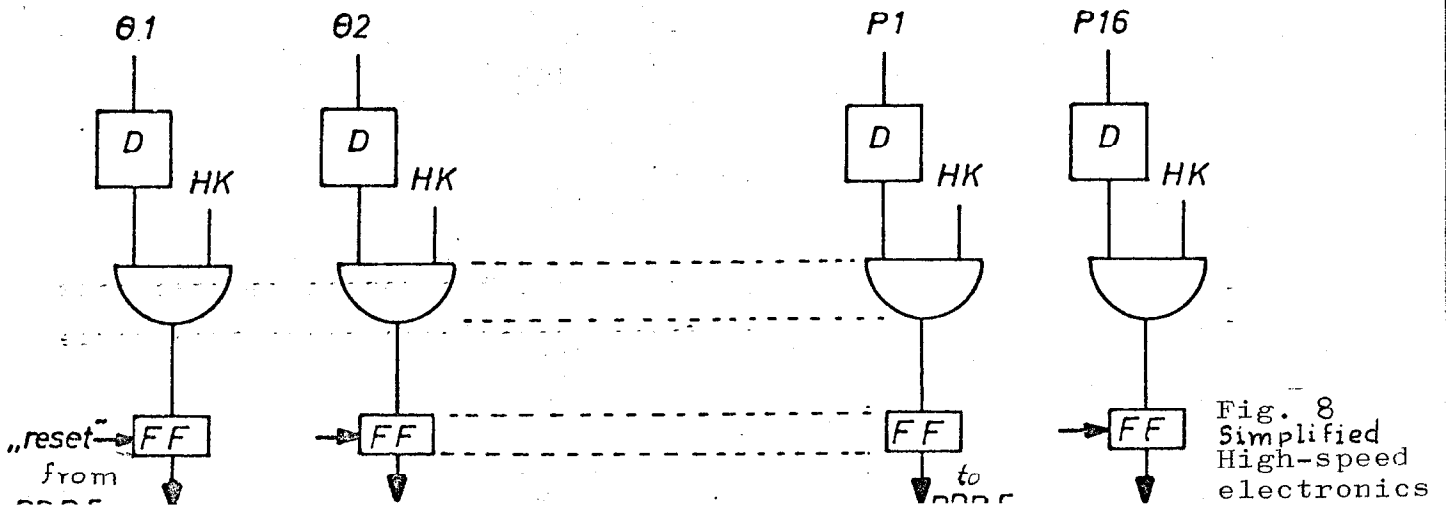in the hodoscope are minimized. This requirement is satisfied
best if the main coincidence pulse occurs at a constant time
interval following the passage of a particle through S1, regard-
less of whether it was a pion or a slow flying proton, thus, if
S1 is "time-determinate" in the main coincidence circuit. For
none-too-small pulses (above 2 Ge/V) this could be attained; be-
low 2 GeV/c, the flight time difference between pions and protons,
however, becomes rapidly so significant that the widths of the

coincidences is no longer sufficient to fully include the protons.

The high-speed coincidence circuits C1 = (23) and C3 = (1234) are made as narrow as can still be justified for the time variations of the counter pulses produced by the dimensions of the scintillator by using short clip cables at the discriminator outputs. The correct time relationships are determined by setting up the spectrometer for negative polarity so that practically only particles with the speed of light are present (e^-, π^-). The plateau of the resolution curves is about 3 nsec while the half-width is about 6 nsec.

The coincidence circuits C2, C4 and C5 (Fig. 8b) in which each time one counter is delayed by such an amount that for a real particle no response may be expected, provide a survey on the orders of magnitude of the random coincidences. The problem of "simulated" events will be discussed in section VI.2.

Each one of the hodoscope counters will be given in a sharp coincidence with the main coincidence pulse. If one of these coincidence circuits responds, the respective flip-flop is set. Together with the digitalized indication of the flight time measurement, this information is then further processed by the PDP-5 computer. The electronic circuit is then open for each γ-ray pulse but only for a clearly defined adjustable time of about 1 msec while during the rest of the time it remains blocked.

6.2) Flight Time Measurement

6.2.1) Principle

A time-amplitude converter (TPC = time to pulse height converter, Chronetics model 105) is used to convert the time overlap of two standard pulses into an analogue signal. The time sequence of the two input pulses is immaterial. The flight time of the pions and protons between the two counters S1 and S3 separated by a distance of 15 m is to be measured. Pions above 1.2 GeV/c are already so close to the speed of light that their flight time within the electronic resolution remains constant over the entire pulse range; protons, in contrast, undergo considerable changes in velocity. Since the TPC does not know how to differentiate which one of the two input pulses comes first, the electronic delay must be so selected in order to establish a clear relationship between amplitude and flight time, that for the rapid particles (e, π) the pulse of the flight-time counter 1 arrives at the TPC earlier than that of the flight-time counter 2. For protons, the second pulse then arrives even later in any case.

Counter 1   Counter 2   time position of pulses
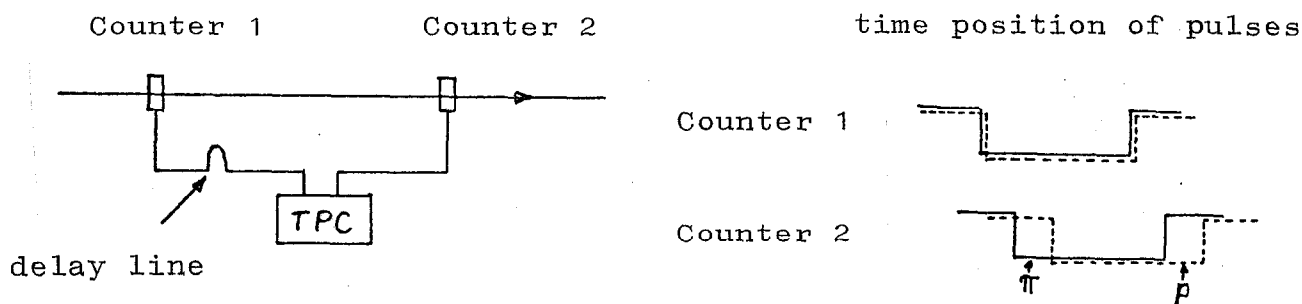

delay line

Fig. 9: Principle of flight-time measurement

We therefore obtain for the most rapid particles a higher overlap, i.e. a higher output amplitude at the TPC, while for slower

particles, a lesser overlap and amplitude are obtained.

6.2.2) Attainable Resolution

In a monochromatic particle beam, the following effects contribute to a widening of the measured flight-time spectrum:

a) Electronic instabilities: variations in amplitude and width of the standard pulses which were made to overlap, variations in the time relationships of these standard pulses to the incoming photo-multiplier pulses (time jitter); instabilities in the TPC.

b) Delay variations in the photo multiplier.

c) Variations in light collection (especially in large-area scintillators and photo-electron yield which also contribute to time jitter in the discriminators.

d) Changes in the light delay in the scintillator as a function of the point of particle passage.

a and b) are essentially given values. They can be separately determined via experiments. Electronic instability can be determined by splitting a photo-multiplier pulse and sending it to two discriminators which drive the TPC. A measurement of this type yielded a distribution with a half width of 0.35 nsec (Fig. 10a). The use of clip cables largely prevented variations in the width of the standard pulses.

Information regarding the effects of a) and b) can be obtained by measuring the flight time between two small scintillation counters. If the scintillators are selected with sufficient

thickness, large amounts of light per particle result, so that
c) becomes negligible. Measurements with two counters measur-
ing 2 cm x 2 cm x 1 cm yielded a resolution of 0.6 nsec half-
width (Fig. 10b). For large-area thin counters (14 cm x 12 cm x
0.5 cm) c) results in a deterioration of the quality of the
half-width to 1 nsec even for a well collimated particle beam
(Fig. 10c). If in addition, a beam with a large aperture and
two extended counters is used, effect d) produces its full im-
pact and degrades the resolution considerably, for example to
a half-width value of 3 nsec for counters S1 and S3 (Fig. 10d).
A good flight-time resolution with large-area scintillators and
extended particle beam can only be attained by compensating or
correcting for light delay variations resulting from the finite
extension. Fig. 11 shows the travel of the maximum in the flight-
time spectrum with the shift of a collimated particle beam over
an extended counter. There are two possibilities to largely
eliminate this effect.

(1) Determination of the particle passage point in the counter
using a finely divided hodoscope and correction of the mea-
sured flight time by using a calibration curve, Fig. 11.
This method was used in the photo production measurements
with average angles for both flight-time counters placed
immediately behind a hodoscope. It requires a recording
of the hodoscope counter information for each event and
a correction of the flight time by a computer. Fig. 13
shows a flight-time spectrum for positively charged parti-
cles without (a) and with correction (b).

(2) A more direct method was indicated by Charpak et al [20] and Ward et al [21] and in the small-angle version of the system [12] as well as during the measruement of the photo production of anti-protons [13]. It is based on the fact that the delay variations can be compensated for if the light of the counters is recorded on both sides by means of photo multipliers. Fig. 12 shows a schematic of this arrangement.

If we compare the symmetrical particle trajectory 1 and the inclined trajectory 2, we see that trajectory 2 sends a delayed signal into 1A and an early signal into 2A, i.e. an enlarged output pulse in the TPC A according to the operating principle of the TPC. On side B the inverse is true. The sum of the signals emanating from TPC A and TPC B, however, is identical for the two trajectories. The amplitude at the TPC is proportional to the overlap of the signals: for trajectory 2 we obtain

$$\text{Ampl. (TPC A)} \sim \frac{x_2}{v_2} - \frac{x_1}{v_1} + T'$$

$$\text{Ampl. (TPC B)} \sim \frac{l_2 - x_2}{v_2} - \frac{l_1 - x_1}{v_1} + T''$$

(where v_i is the speed of light in the scintillator i, T', T'' = electronic constants).

Since the proportionality constants are identical in symmetrical structures the following expression applies to the sum:

$$\text{Ampl. (A+B)} \sim \frac{l_2}{v_2} - \frac{l_1}{v_1} + T' + T''$$

a)

0.35 nsec   2 cm x 2 cm x 1 cm
             scintillator, pulse
             distributed

b)

0.6 nsec   two 2 cm x 2 cm x
            1 cm counters

c)

1.0 nsec   One 2 cm x 2 cm x
            1 cm counter, one
            14 cm x 12 cm x 0.5
            cm counter

d)

3.2 nsec   One 14 cm x 12 cm x
            0.5 cm counter, one
            .28 cm x 16 cm x 1.0
            cm counter (pion beam
            with full
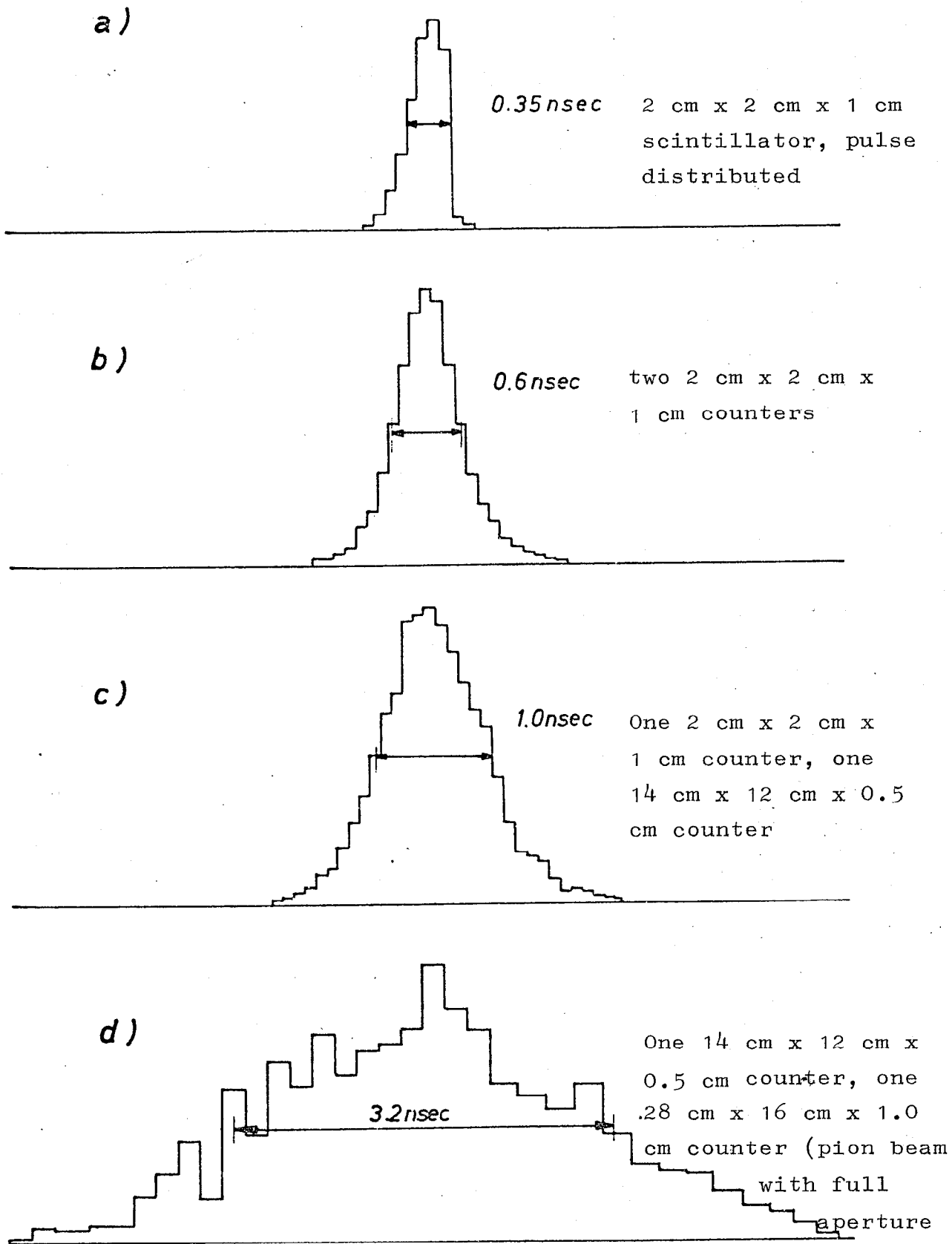   aperture

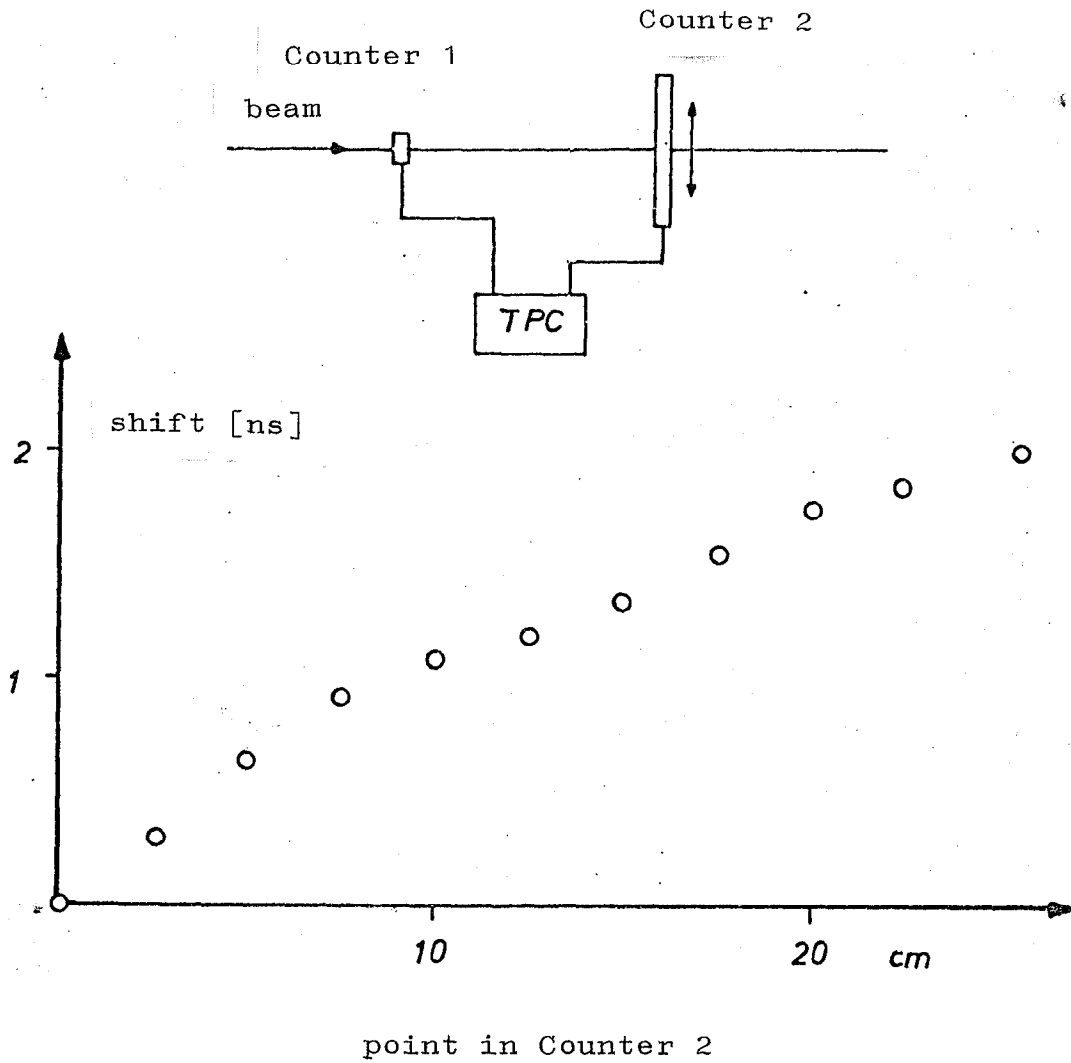Fig. 10:   Attainable resolution for flight-time measurement

Fig. 11: Shift of the flight-time distribution as a
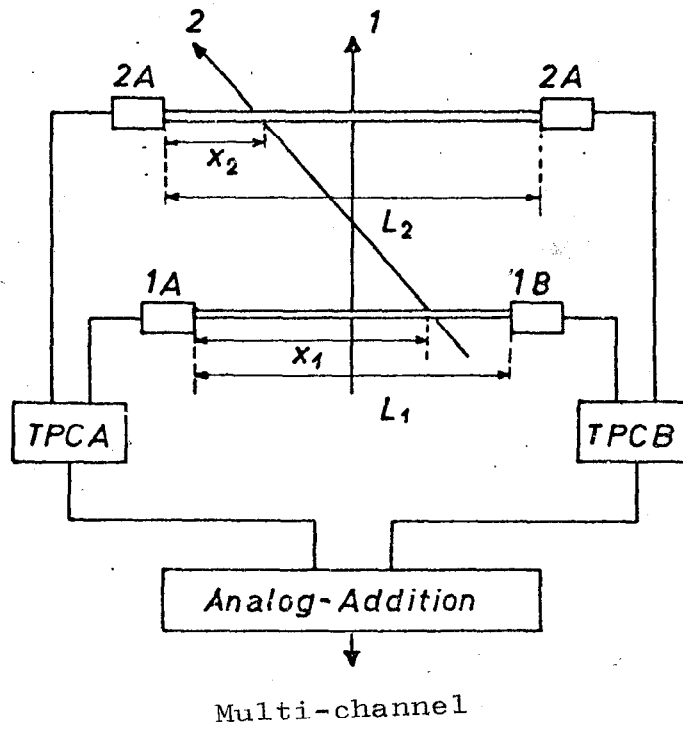function of particle passage point in the
counter.

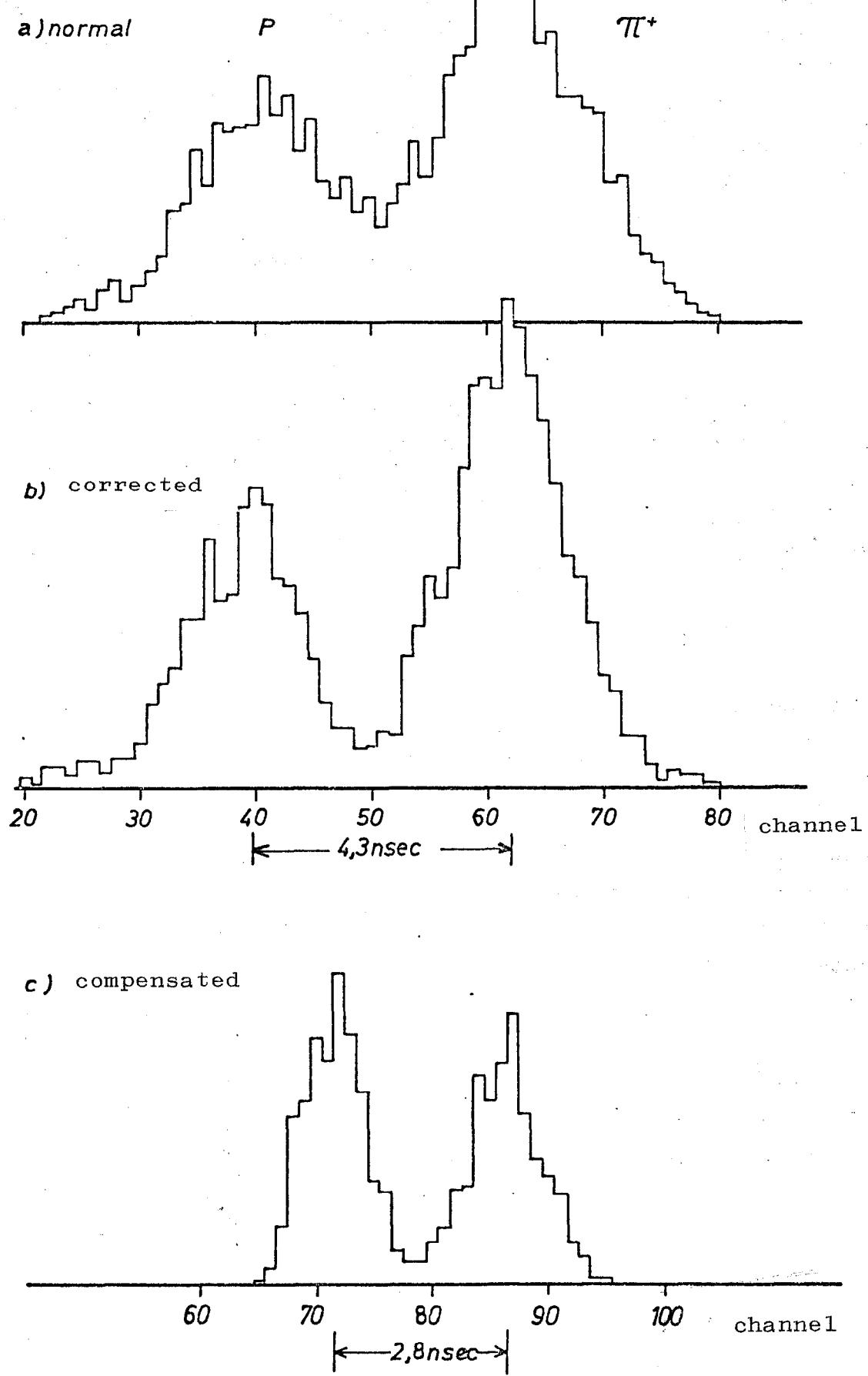Fig. 12: Compensation for finite counter dimensions.

Fig. 13: Flight-time spectrum for positively charged particles (explanation in text).

The summation amplitude is independent of x_1, x_2, i.e. it has the same value for every trajectory. Measurements with a collimated electron beam show in fact that the position of the maximum in the flight time spectrum is shifted by less than 0.3 nsec if the beam moves over the full breadth of a 30 cm counter -- as compared to more than 2 nsec in a non-compensated case (Fig. 11). As shown by Fig. 13c) the resolution in the extended particle beam is improved considerably and we obtain a half-width of 1.3 nsec.

6.2.3) Flight Time Electronics Design

Since the TPC has a long integration-time constant care must be taken that the flight-time electronics are opened only for the event under study and that it remains closed for all others (background particles). In principle this can be accomplished by using the gate circuit built into the TPC. However, the gate pulse must be made wide enough to include the input pulses emanating from S1 and S3 over the entire velocity range of the particles in the spectrometer. Since this would require pulses in excess of 30 nsec wide, this could lead to random coincidences in the flight time system as a result of the high background count rate in S1, leading to an erroneous spectrum. For this reason, the following principle is applied: The pulses from S1 and S3 which are used to measure the flight time must always coincide with the main coincidence pulse prior to reaching the TPC (Fig. 8c).

These coincidences, however, must be so designed that they ob-

serve strictly the time relationships between counter pulses.
This can be accomplished by making the counter pulse arrive in
the particular coincidence circuit later than the main coin-
cidence pulse.
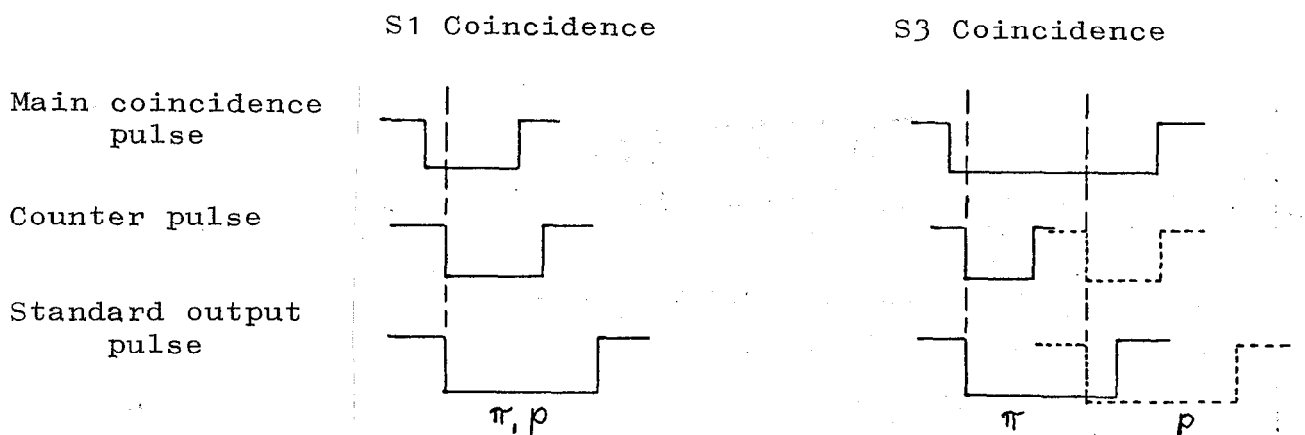
Fig. 14: Flight time coincidences

Fig. 14 contains time diagrams of the pulses. If we take care,
as assumed in Fig. 14 that S1 is "time determinant" in the main
coincidence circuit (see section 6.1), the flight time coin-
cidence with S1 can be made narrow ($\leq$ 10 nsec) and thus the back-
ground is suppressed. The flight time coincidence with S3 must
then be selected so wide that the total delay interval between
pions and protons is included. However, the main coincidence
pulse may be selected sufficiently wide since S3 is barely hit
by the background. The output pulses of the coincidences which
are strongly related under the present conditions to the counter
pulses regarding their time position are standardized with re-
spect to amplitude (-300 mV) and length (15 nsec, 93-Ω clip
cable, 2-m long). They are made to overlap in the TPC according

to the method described in section 6.2.1. The amplitude of the
analogue signal is digitalized in a 128 channel anaglogue-to-
digital converter (ADC) and stored in a flip-flop register prior
to being fed into the computer. The flight time system yields
a linear relationship between the flight time difference against
pions and output amplitude in a variation range of about 10 nsec.
Fig. 15 shows the positions of the pion and proton maxima in the
spectrum as a function of pulses for a large number of measure-
ments in the average angular range. The position of the pion
maximum is practically constant which represents a good test
of the stability of the system over a long period of time while
the position of the proton maximum coincides fairly well with
the flight time difference between proton and pion as a function
of the pulse calculated for a flight path of 15 m. Below 1.9
GeV/c this condition is no longer met since the protons travel
now so slowly that they no longer satisfy the time relationships
for the main coincidence.

II.7) Data Processing Equipment

7.1) Considerations regarding the Computer Connection

An event is characterized by its flight time and the response of
a certain counter in the angular and pulse hodoscope. If this
information is to be retained in a general form throughout the
entire measurement, 192 electronic coincidences would be re-
quired to record the 12 x 16 combinations between angle and
pulse counters alone. Any further expansion of the system using
additional hodoscopes or Cerenkov counters would multiply the
number of possible classifications and thus the electronic re-

calculated position for
protons (flight path ~
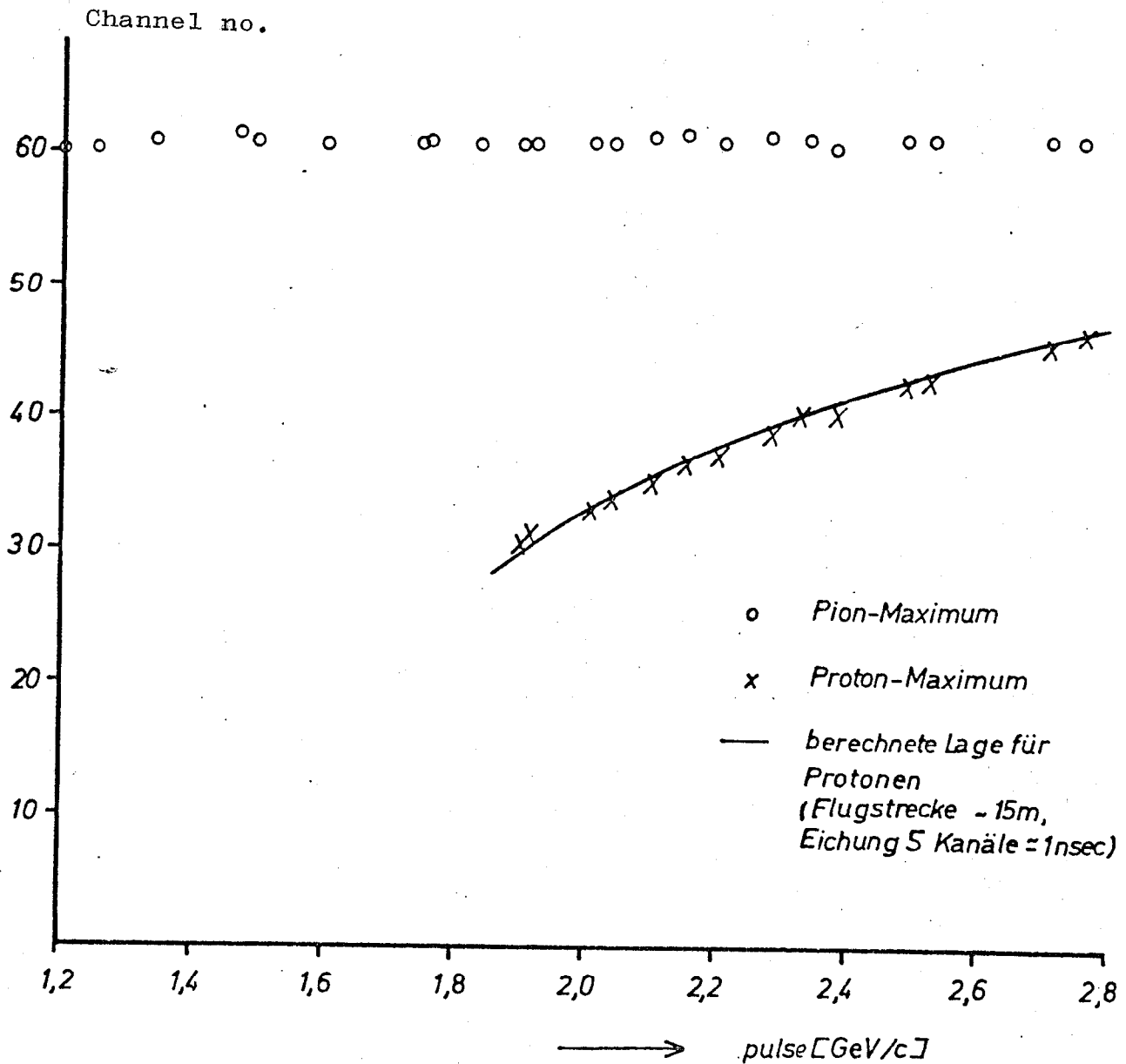15 m, calibration 5
channels ~ 1 nsec)

Fig. 15: Position of the pion and proton maximum in the
flight time spectrum as a function of the pulse.

requirements. Therefore, a concept was being pursued from the
beginning in which the high-speed electronice logic must make
only relatively few decisions during the measurement process,
such as the determination of the fact that a charged particle
passed through the spectrometer and the measurement of its
flight time. A large amount of the classification work is per-
formed in an electronic computer. This requires that the im-
portant information is not simply summed up during a measure-
ment but it is stored for each event individually in order to
have available afterwards all possibilities of classification.
For storage purposes a magnetic tape is used on which the re-
cordings are entered by a PDP-5 computer [22]. The advantage
in the use of a computer lies in the fact that it can perform
other tasks as will be shown below.

7.2) PDP-5 System Design

The PDP-5 computer has two core memories with 4096 twelve bit
words and a 6 μsec cycle, for magnetic tape units (DEC tapes),
a programmed oscillograph tube subject to selection, a teleprinter
unit with punched tape readout and puncher and the capability
to control external instruments by means of special commands
as well as a capability to read data directly into one of the
core memories, using the data break mode. The primary function
of the equipment consists of providing the necessary identifi-
cation characteristics for the data obtained during the exper-
iment and to enter them on the magnetic tape. Following the
conclusion of the measurement, the tape content is send via

data lines to the IBM 7044 unit of the DESY computer center where
it can be evaluated. Due to the short 12 bit word only a 128
words can be addressed directly in the core memory. Consequent-
ly, the memories are divided into "pages" of 128 words each.
The same division is maintained for arranging the information
in the form of blocks on the magnetic tape.

7.3) Computer Tasks during the Experiment

The operation of the PDP-5 is controlled by a system of EXSYS
programs (experimental system), operating in the first core
memory. The second core memory is used as an intermediate
storage device for the data.

7.3.1) Preparation of a Measurement; Structure of the Data Tape

The data emanating from the experiment are arranged on the data
tape in the form of 128-word blocks. They are framed by one
identification flock each (FDB = fixed data block) at the be-
ginning and at the end of the measurement which contains the
number of the measurement as well as a series of important
physical parameter such as the energy of the synchrotron, the
pulse and the angle of the spectrometer, etc. During the first
phase, EXSYS requires the input of these parameters via the tele-
printer. The content of the electronic counters which record
the count rates of the high-speed electronic that are of any
interest, are also read in by the PDP-5 before and after the
measurement and recorded in a special block (SDB = scaler data
block) on the data tape.
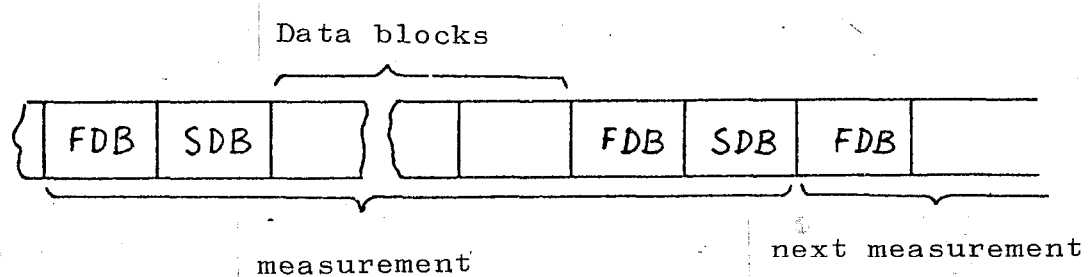
Fig. 16: Structure of the Data Tape

The two non-data blocks receive as their identification as the first word a number with positive parity; 7777 (octal) for FDB, 7774 for SDB, while data words have a negative parity.

7.3.2) Data Phase

Since the information for one event includes more than 12 bits, it is distributed over 4 PDP-5 words (Fig. 17).

The highest bit designated with a "p" is so set for each word that an odd overall parity results. The bits designated with ">1" in the first and third word are set at 1 by special electronic units if more than one counter responded in the angle and pulse hodoscope so that the particle path is no longer clearly capably of being reconstructed. The input of these 4 word per event proceeds in the data break mode (Fig. 18).

If an event has occurred, the main coincidence pulse (HK) sets a flip-flop connected to the "break request" input of the PDP-5.

The unit still performs the operation just started during the running program, an then stops the program. At the beginning of the measurement, the external address register is set to 1 and the word counter operating in cycles is set to 1 so that the first word of the first event is placed in location 1 of the data memory. Once it is completed, the PDP finishes a "ready" signal which is used to switch the external address register and the word counter by 1 digit. Now, the second word on the next core memory place is recorded. After the fourth word has been read in, the next "ready" pulse resets the main coincidence flip-flop and the hodoscope and ADC flip-flop register. The PDP-5 now leaves the data break mode and resumes its work at the interrupted program. As long as the HK flip-flop is set, that if data are being read in, the high-speed electronics are blocked so that during this time no further events are accepted. This "dead time" is of the order of magnitude of 60 μsec and is given primarily by the conversion time of the ADC of 35 μsec. Count rate losses resulting from this are corrected similar to the quantameter correction by using a monitoring telescope.

During the measurement, the main program operates as a sorting program which calculates from the incoming data the particular hodoscope counters and which continuously sums up the flight time spectra and the count rate profiles in the hodoscopes and records them on the oscillograph screen. Therefore, continuous

control over the proper operation of the apparatus is provided.

| P | θ10 | | θ1 | >1 | first word |

| P | Flight time (9 bits) | θ12 | θ11 | second word |

| P | P10 | | P1 | >1 | third word |

| P | free for additional P16 | | P11 | fourth word |
| | information | | | |
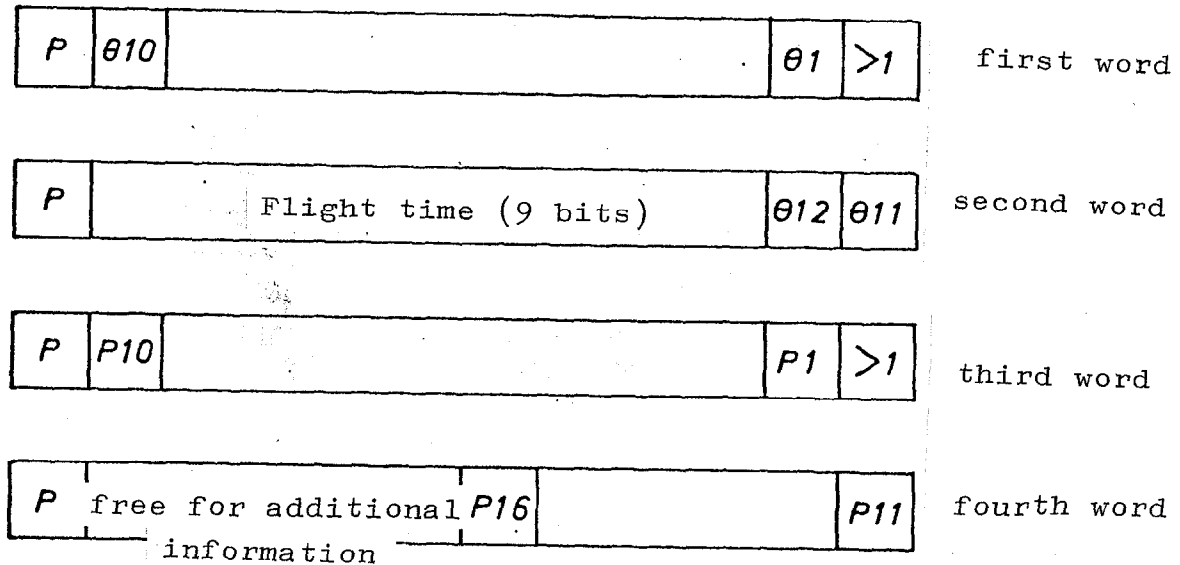
Fig. 17: Distribution of the information of one event
over four PDP-5 words.

The data memory is divided into two halves. If one half is
full, an interrupt signal calls up a program which records
this data on tape while the read-in of the events continues in
the other half. Following the completion of the measurement,
the last data block started is filled up with a call word (7600
octal) which will be needed during the evaluation in order to

Hodoscope or flight time electronics

Fig. 18: Read-in of one event per data break.

verify the end of the data. The parameter and counter blocks
(FDB, SDB) are then still recorded on the data tape.

7.3.3) Transmission to the IBM-7044

Following the completion of a measurement, the capability exists
to send collected information from the data tape to the IBM-7044.
An interrupt signal from the PDP causes the IBM unit to inter-
rupt its current program and to store it away, and to load up
on an evaluation program which stores the incoming data in a
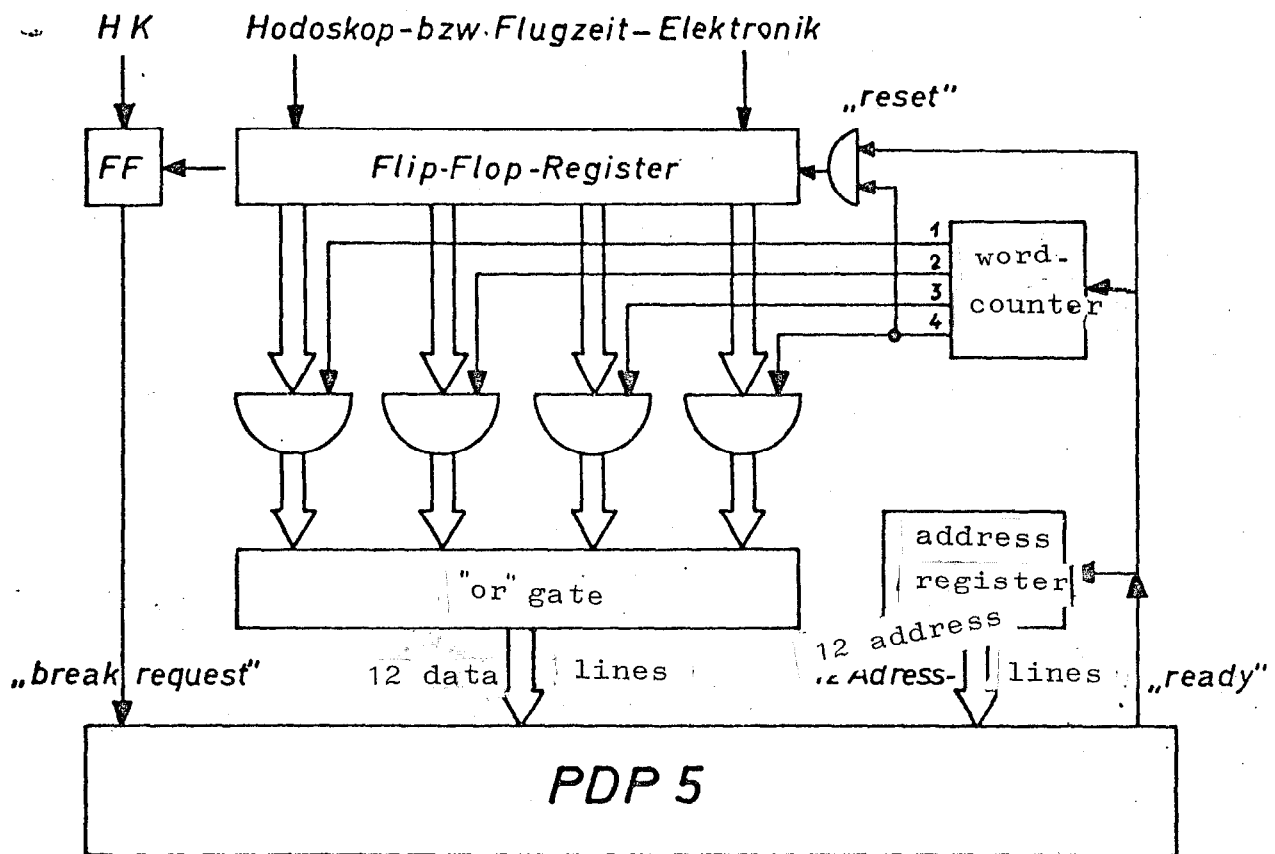disc file temporarily and which then begins to sort it, cal-
culate its dynamics and its effective cross sections. The
required physical parameters are obtained from the FDB. The
analysis results are returned to the PDP and printed out on the
teleprinter. Printing begins about 10 sec after the conclusion
of the measurement.

Once the entire measurement is completed, all PDP data tapes
can be transmitted to the IBM unit via pulse lines and copied
on IBM magnetic tape.

III. Evaluation and Corrections

III.1) Structure of the Evaluation Programs

The data copied on the IBM magnetic tape are subdivided on that
tape and on the PDP-5 magnetic tape into blocks (records) of
128 words each. The measurements are arranged on the tape on
an increasing numerical scale. Before the evaluation program
to analyze a certain measurement can het under way, the cor-

responding data on the magnetic tape must be found. Fig. 19
shows a simplified flow diagram. The tape is read record by
record starting at the beginning. There are two distinct
phases. The program first enters the seach phase (Phase 0 in
the flow diagram); here all data records are ignored and only
the first parameter block (FDB) with the desired number of the
measurement series is searched for. As soon as it has been
found, the program enters the data sorting phase (Phase 1).
The data pertaining to the measurement series are sorted event
by event according to the hodoscope counter and flight time
information until they have all been processed. Optionally,
a group of measurements can be analyzed jointly, for example,
full and empty target measurements under otherwise identical
conditions. In this case the program asks whether any addition-
al measurements exist within the group and if need be it returns
to the search phase in order to find the next measurement. Once
the group is completed, the sub programs to calculate the dy-
namics and the effective cross sections are called up and the
results are printed out.

In another version of the evaluation program, a fixed matrix is
assumed in a plane $k-\theta^*$ and all measurement series are classified
according to their dynamic conditions in the fixed $k-\theta^*$ intervals.

III.2) Averaging in the Computation of Effective Cross Sections
It is the purpose of the computations to find the differential
effective cross section $d\sigma/d\Omega^*$ as a function of the two variables

γ energy k and pion center-of-mass angle θ^* as well as $d\sigma/dt$ as a function of the invariance s, t (cf. VI.1, (A3)). However, the spectrometer covers a considerable band in k and θ so that if a substantial variability of the effective cross section in one of these variables, not always permitting averaging over the entire acceptance window. On the other hand, an effective cross section computation yields no reasonable statistical value for the individual angle and pulse hodoscope counters (θp) combinations which have a very good resolution in k as well as in θ, since the average particle number per θp window is approximately 10. Therefore, suitable averaging over many of these windows is necessary. Pulses and angles are so selected for the various measurements that in a k-θ^* plane the acceptance limits overlap and the entire range covered is practically filled with events at a high energy rate as shown in Fig. 20. An averaging process used by us consists of the following: a line grid with constant k and θ^* having a suitably selected division is assumed to exist in this plane and each θp window of a measurement is classified into the small box corresponding to its dynamic values. The classification is so selected that if the interval values are halved, and if the grid is shifted within statistical variations, no systematic change of the effective cross section is observed as a function of energy or the angle.

Let us now consider a rectangle into which falls a series of θp windows with count rates N_i and acceptances A_i. Assuming that

Start

Read numbers of measurements contained in group

Phase 0

Whole block from tape

FDB? — no

yes

first FDB? — yes

no

last FDB? — no

yes

Additional measurement in the group? — yes

no

Dynamic effective cross section computation

Print out of results

Other groups? — yes / no

End

Measurement of correct number? — no

yes

Phase 1

Measurement parameter determined

Phase 1? — no

yes

Sorting events of data block

Fig. 19: Flow diagram of the evaluation programs (simplified).

DATA TAPE STRUCTURE

data

| FDB | SDB | | | ... | FDB | SDB | FDB | SDB |

Measurement no. N   Measurement no. (N+1)
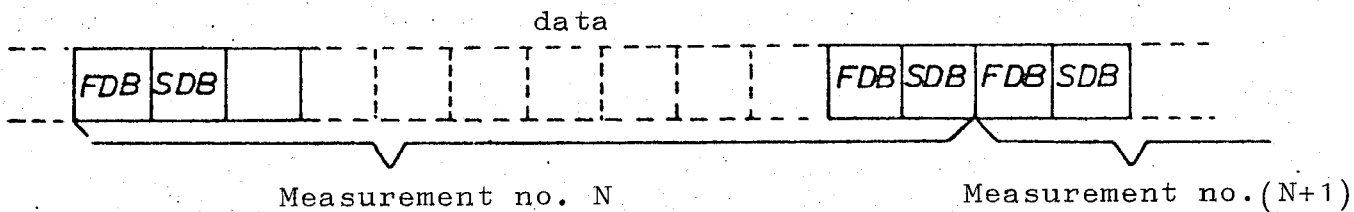
the effective cross section is constant within this rectangle
and that for the count rate in each Θp window Poisson's sta-
tistical method is applicable, there follows a very simple
expression for the optimum statistical value of the effective
cross section using the maximum likelihood method [23].

Let us assume that σ has been found. The average value of the
count rate in the Θp window i is then given by

$$\overline{n}_i = \sigma \, A_i \, F_i$$

where the F_i dynamic factors, the number of target atoms per
cm^2 contain the incident intensity and similar factors. The
acceptances A_i are assumed to be error free.

The likelihood to measure exactly n_i particles for an average
value of $\overline{n}_i$ is

$$W(n_i) = e^{-\overline{n}_i} \frac{(\overline{n}_i)^{n_i}}{n_i!} = e^{-\sigma A_i F_i} \frac{(\sigma A_i F_i)^{n_i}}{n_i!}$$

The likelihood function L is the product over all the i values
of this likelihood.

$$\mathscr{L} = \mathscr{L}(\sigma) = \prod_i e^{-\sigma A_i F_i} \frac{(\sigma A_i F_i)^{n_i}}{n_i!}$$

Evidently the optimum value for σ has been found when L is max-
imum. To simplify matters, the maximum of

$$w = \log \mathscr{L} = -\sigma \sum A_i F_i + \log \sigma \sum n_i + \sum n_i \log(A_i F_i)$$
$$- \sum \log(n_i!)$$

will be sought.

From $dw/d\sigma = 0$ it follows immediately that

$$\sigma = \frac{\sum n_i}{\sum A_i F_i}$$

The variance of σ is given by [23]

$$(\Delta\sigma)^2 = \left(-\frac{d^2 w}{d\sigma^2}\right)^{-1} = \frac{\sigma^2}{\sum n_i} \quad , \quad \Delta\sigma = \frac{\sigma}{\sqrt{N}} \quad , \quad N = \sum n_i$$

The empty target correction is accomplished in a way that for full as well empty target measurements the effective cross section is calculated as indicated and the effective cross section in hydrogen is then the difference, yielding the error by the quadratic addition of the individual errors (hydrogen gass in the empty gas is taken into account, see below). Similar to the $d\sigma/d\Omega^*$ calculation, the determination of $d\sigma/dt$ is accomplished by classifying it in a lattice s-t frame.

III.3) Calculation of the Effective Cross Sections for π^+
        One-Pion Production

3.1) Formula for the Effective Cross Section

The number of the π^+-mesons detected is given by the following expression

$$N_\pi = \underbrace{\frac{d\sigma}{d\Omega^*}}_{measured} \overline{\frac{d\Omega^*}{d\Omega}} \; Q_{eff} \overline{\left(\frac{1}{k}\right)} \overline{f(k,k_{max})} \; N_p \; f_{zerf} \; f_{abs} \; f \underbrace{\int d\Omega \, dk}_{\substack{Akzeptanz \\ Spektrometer}} \quad ,$$

where

$\dfrac{d\sigma}{d\Omega^*}$ =   The differential effective cross section for

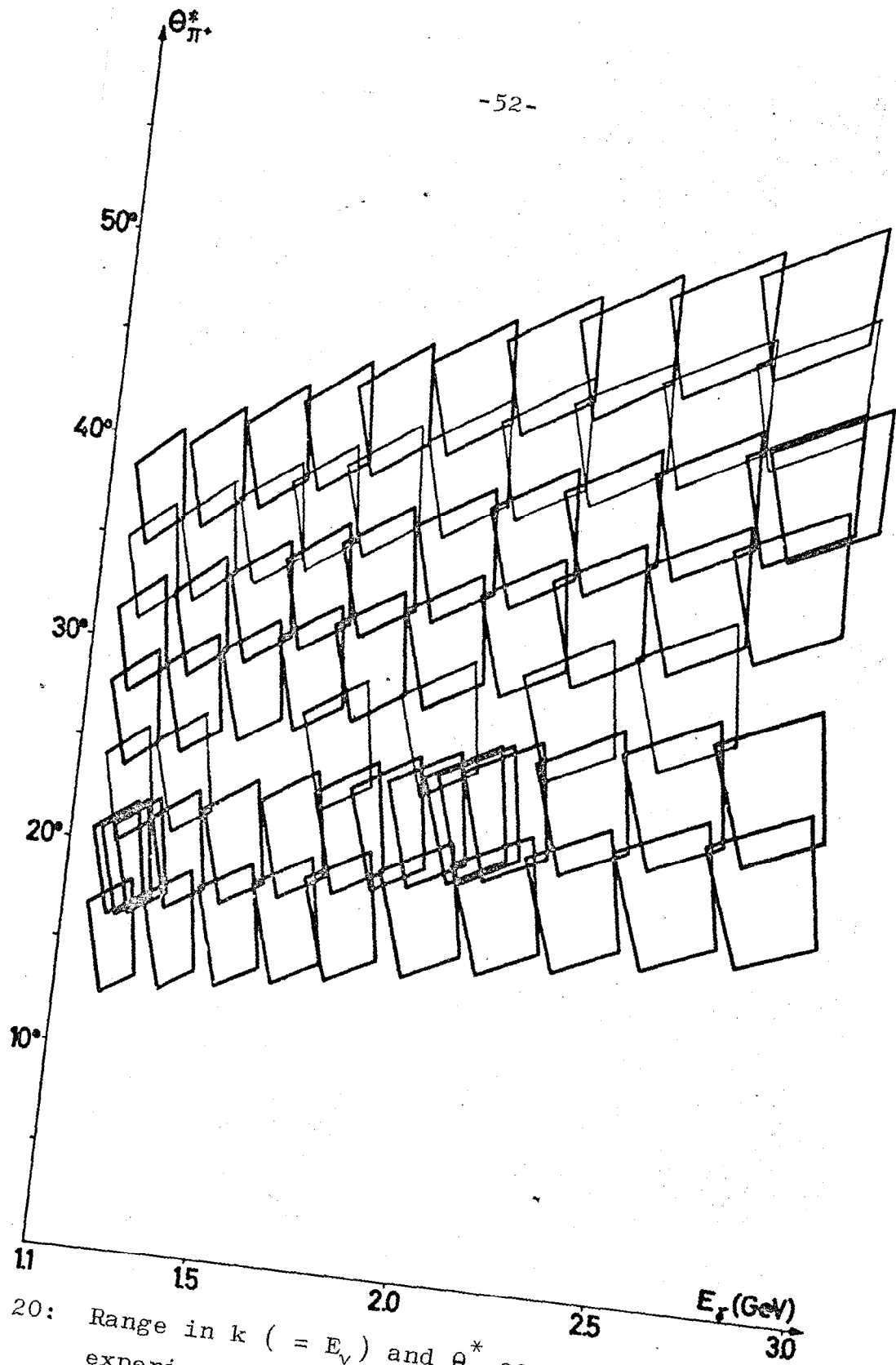$\qquad\qquad\qquad \gamma p \rightarrow \pi^+ n$

Fig. 20: Range in k (= E_γ) and θ^* covered in the present
experiment. The acceptance in the k-θ^* plane is
given by an irregular quadrangle for each spec-
trometer setting (cf. Fig. 7).

$\dfrac{d\Omega^*}{d\Omega}$ = Directional angle conversion from the center-of-mass to the laboratory system

$Q_{eff}\ \dfrac{1}{k}\ f(k,k_{max})\Delta k$ = Number of photons in energy interval k, $k + \Delta k$ (s, see below)

N_p = Number of hydrogen atoms per cm^2 in the target

f_{zerf}, f_{abs}, f = Correction factors for pion decay, nuclear absorption and other smaller corrections (zerf = Zerfall = decay).

The serifs represent an average calculation of the values $d\sigma/d\Omega^*$ assumed as slightly variable, over the spectrometer acceptance.

The integral

$$\int_{Akz.} d\Omega\, dk \qquad [Akz = \text{acceptance}]$$

whose integration variable are Θ and k, are to be converted into the new variable Θ, p since it can then be expressed by the "acceptance" expression $A = \Delta\Omega\ \dfrac{\Delta p}{p_0} = \int_{Akz} d\Omega\ \dfrac{dp}{p_0}$.

$$\int_{Akz.} d\Omega\, dk = \int_{Akz.} \frac{\partial(k,\Theta)}{\partial(p,\Theta)}\, d\Omega\, dp = p_0 \int_{Akz.} \frac{\partial(k,\Theta)}{\partial(p,\Theta)}\, d\Omega\ \frac{dp}{p_0}$$

The functional determinant is

$$\frac{\partial(k,\Theta)}{\partial(p,\Theta)} = \left.\frac{\partial k}{\partial p}\right|_{\Theta} \left.\frac{\partial \Theta}{\partial \Theta}\right|_{p} - \left.\frac{\partial k}{\partial \Theta}\right|_{p} \left.\frac{\partial \Theta}{\partial p}\right|_{\Theta} = \left.\frac{\partial k}{\partial p}\right|_{\Theta}$$

Therefore,

$$\int_{Ak z} d\Omega \, dk = p_o \overline{\left(\frac{\partial k}{\partial p}\right)_\theta} \cdot A$$

For the effective cross section computation we now do not
average over the total acceptance of the spectrometer but only
over a hodoscope counter combination $\theta_i p_j$. The angle and pulse
interval thus included is so small that all values may be
considered constant and the average value formation may be omit-
ted. The total result which is a combination between the mea-
sured particle number and the effective cross section, yield
the formula

$$N_{\pi gem.} = \frac{d\sigma}{d\Omega^*} \cdot \frac{d\Omega^*}{d\Omega} A \left(\frac{\partial k}{\partial p}\right)_\theta \frac{p_o}{k} Q_{eff} f(k, k_{max}) N_p f_{zerf} f_{abs} f \tag{3}$$

$d\Omega^*/d\Omega$ and $\left(\frac{\delta k}{\delta p}\right)_\theta$ are values which can be calculated from the
dynamics of the π^+ photo production (VI.1, Eqs. (A8 and A9)).
For the assumed average pulse p_O and the average angle θ_o for
the spectrometer, a particle must have the defined deviations
Δp_{ij} and $\Delta \theta_{ij}$ from these values in order for it to reach the
given θ-p window characterized by subscripts i and j (angle
hodoscope counter no. i, pulse hodoscope counter no. j) (cf.
Fig. 7). The values for these deviations are calculated for
a variation program [18] and fed in as external data in the
evaluation programs. Thus, the values $p_{ij} = p_o + \Delta p_{ij}$,
$\theta_{ij} = \theta_o + \Delta \theta_{ij}$ are known for each θp window (ij) and thus also
all the other dynamic values, such as $(d\Omega^*/d\Omega)_{ij}$. The Monte

Carlo programs to calculate the acceptance determine the acceptances A_{ij} for each individual window, so that all the required values for the averaging process explained in section III.2 are known.

Q_{eff} is an abbreviation for the number of "effective quanta," i.e. the number of γ quanta with maximum energy k_{max} which would yield the same total energy as the integrated spectrum:

$$E_{total} = \int_0^{k_{max}} k\, N(k)\, dk = Q_{eff}\, k_{max}$$

From the total charge Q measured in the quantameter, the calibration constant of the quantameter [17] and the maximum γ energy, we calculated

$$Q_{eff} = \frac{Q\,[Coul]\; 3.35 \cdot 10^{18}\,[MeV/Coul]}{k_{max}\,[MeV]}$$

The additional factors in Eq. (3) are dealt with in the following sections.

The connection between $d\sigma/d\Omega^*$ and $d\sigma/dt$ results from

$$t = m_\pi^2 - 2k^* E_\pi^* + 2k^* p_\pi^* \cos\theta_\pi^* \tag{A3}$$

and yields
$$\frac{d\sigma}{dt} = \frac{\pi}{k^* p_\pi^*} \cdot \frac{d\sigma}{d\Omega^*}$$

3.2) Available Range and Form of the Brems Sprectrum

In accordance with Fig.1, the energy distance between the one-pion production and multiple-pion production is about 150 MeV, rather independent of energy and angle within the intervals covered during the experiment. If we select the average momentum p_o of the spectrometer in such a way that the respective γ energy is approximately 100 MeV from the Brems edge, a large part of the acceptance window is accessible only to pions resulting from one-pion production for a momentum acceptance of $\pm$ 5% up to the highest energies (3 GeV). To calculate the effective cross sections, the spectrum is not utilized up to the Brems edge, but is cut off 50 MeV below since the γ intensity at the upper edge of the spectrum is a highly variable function of the energy and small variations in the terminal energy of the electrons have an extremely pronounced effect. The lower cutoff limit was made 200 Mev less than k_{max}. This was to include no major portion of multiple processes, primarily since these can only be triggered by photons stemming from the vicinity of the Brems edge whose number is small, and also since the phase space slightly beyond the threshold is still small. This selection of the lower limit is justified by the fact that for the effective cross sections and with the narrowing of the energy interval included to the range a k_{max} - 150 MeV $\leq k \leq k_{max}$ - 50 MeV and for expanding the range k_{max} - 250 MeV $\leq k \leq k_{max}$ - 50 MeV yields tolerable values within the statistical error limits.

The number of photons in an energy interval k, k + Δk is given by

$$N(k) \; \Delta k = Q_{eff} \; \frac{\Delta k}{k} \; f(k, \; k_{max}),$$

where the function f (k, k_{max}), in addition to the exact form of the Bethe-Heitler effective cross section also takes into account that the Brems radiation in the synchrotron is produced in a relatively thick target of a high order --0.06 or 0.125 radiation lengths of tantalum, in which the electrons undergo considerable energy losses and scattering prior to the Brems radiation process.* Near the Brems edge, this is particularly effective. The systematic error that is introduced is estimated at 2% (for a more detailed discussion, see Reference [12]).

The reliability of the correction can be tested experimentally: Effective cross sections with two different upper cutoff energies were calculated k_{max} - 200 MeV $\leq$ k $\leq$ k_{max} - 50 MeV

and k_{max} - 200 MeV $\leq$ k $\leq$ k_{max} - 100 MeV

within the error limits, the results are compatible, but the values calculated with 100 MeV cutoff energy are almost always a few per cent higher.

3.3) Target Thickness, Empty Target Effect

---

*Because of the relationship $Q_{eff} \cdot k_{max} = \int_{o}^{k_{max}} k \; N(k) \; dk$, f is

normalized as follows: $\int_{o}^{k_{max}} f(k, \; k_{max}) \; dk = 1$

The cell used for the liquid hydrogen has an internal diameter
of 69.7 $\pm$ 0.2 mm. Since the total width of the γ-ray at the
target is 35 mm following the target acceptance, the thickness
change of the target over the beam cross section is not neg-
ligible. To calculate an effective target thickness, the in-
tensity profile of the γ-ray must be taken into account; an
average thickness results in the following

$$\overline{D} = \int_{-17.5}^{+17.5} D(x)\, I_\gamma(x)\, dx \bigg/ \int_{-17.5}^{+17.5} I_\gamma(x)\, dx$$

where $D(x)$ represents the cell thickness and $I_\gamma(x)$ the intensity
of the γ-ray at a distance of x mm from the center. Using a
measured intensity profile [20], an effective target thickness
of

$$\overline{D} = 67.5 \text{ mm}$$

was calculated. The thickness of the liquid hydrogen at 760 torr
is 0.071 g/cm^3 [25] so that an average proton density of

$$N_p = 2.86 \cdot 10^{23} \text{ protons}/cm^2$$

results.

Empty Target Effect, Correction for Gas Bubbles in the Liquid

Hydrogen

The cell is emptied by pressing the liquid hydrogen back into
the reservoir by means of helium gas. The cell is then filled
with cold hydrogen gas with some helium admixture. Using the
ideal gas equation, we obtain for the density of the hydrogen
gas at the boiling point

$$\rho_{H_2 \text{ gas}} = 0.0013 \text{ g/cm}^3 \qquad\qquad (T = 20.4^\circ K, \text{ 760 torr}).$$

The density of helium is almost double this value, i.e. the same number of protons per cm^3. In calculating this correction, it may be assumed that the π^+ photo production at the two protons of a helium nucleus is incoherent. (π^+ production at the neutrons requires at least an additional negative charged particle and can therefore not interfer as a multiple process for dynamic reasons.) A contribution of $0.0013/0.071 = 2\%$ of the rate in liquid hydrogen is therefore expected of the gas in the cell, quite independent of the fact whether pure hydrogen gas or helium is contained therein. From the measured empty target rate which was in most cases near 5 to 8% of the full target rate, this amount must still be deducted to obtain the true empty target effect.

The contribution of the gas bubbles in liquid hydrogen in the cell can be estimated as follows. The consumption of liquid hydrogen is 130 cm^3 per hr, and this corresponds to 7000 cm^3 of gas per hr (gas at $20.4^\circ K$). If it is assumed in the worst case that total evaporation occurs in the cell, the total volume of the gas bubbles in the cell must be divided by their average time of stay within the liquid (according to optical impressions it is small with respect to 1 sec) and must be equal to the gas flow, i.e. 2 cm^3/sec. The total gas volume is thus small compared to 2 cm^3, if we compare it with a liquid volume of 550 cm^3, so that the correction thus produced is

negligible.

3.4) Pion Decay

If a pion decays on its flight path prior to reaching the deflection magnets, the muon thus produced generally has such a highly changed momentum that it no longer remains within the spectrometer acceptance. The pion would thus not be counted. However, if the decay occurs behind the magnet, the probability is increased that the muon is collected since the angle changes in the laboratory system is very small for the decay in most cases. A Monte Carlo calculation[*] which follows the muons resulting from the π decay through the system, provided the following relationship relating the measured and the "real" pion rate

$$f_{zerf} = \exp\left(-0.338/p_o\right) + 0.106 \left(1 - p_o \cdot 0.08\right)$$

$$\left(p_o = \text{spectrometer momentum in GeV/c}\right)$$

The first term follows from the conventional law of decay: The number of the pions not decayed after time t is given by $e^{-t/\tau}$, where $\tau = \gamma \, \tau_o$ which represents the lifetime increased by the Lorentz factor and is approximately the flight time from the target to the last counter. The second term which is also slightly momentum-dependent, takes into account the muon fraction which is still being detected in the system.

3.5) Absorption of Pions due to Strong Interaction

[*]DAMUON program by R.D. Eandi

A pion must cross on its path through the spectrometer an average of 3.5 cm of liquid hydrogen, about 5 m of air and 3.5 cm of scintillator until it reaches the last counter. The absorption in helium can be neglected. The effective cross sections for absorption and scattering of π^+-mesons in heavy nuclei is not too well known. Longo and Moyer [26] indicate 3 GeV/c π^+-mesons:

	σ abs	σ el	
π^+-Be	192 $\pm$ 8	41.5 $\pm$ 3.5	mb
π^+-C	213 $\pm$ 8	66.6 $\pm$ 7	mb
π^+-Al	428 $\pm$ 15	160 $\pm$ 14	mb

For 1.65 GeV/c π^--mesons, the following applies according to Bowen et al [27].

$$\pi^- \text{-C} \quad \sigma_{atten} = 219 \pm 11 \text{ mb}$$

$$\sigma_{el} \approx 80 \text{ mb}$$

hence of the same order of magnitude.

However, if we multiply the very well known π^+-p effective cross section (for example [28]) by a factor of $A^{2/3}$, substantially smaller values result.

The elastic scattering of pions at neucleons is characterized by the defraction mechanism. If the same nuclei are assumed and if we assume a radius of the interaction of $R = r_o A^{1/3}$, the resulting angle distributions for pulses of approximately 2 GeV/c are still very wide compared to the coulomb-multiple scattering, mainly in the order of magnitude of several degrees

of half-widths. A pion which is scattered in one of the front
scintillation counters, is therefore very likely to be de-
flected considerably so that it no longer flies through the
entire remaining system. A Monte-Carlo calculation confirmed
this reasoning. Up to and including counter S2 the total pion-
nucleon effective cross section is therefore utilized to cal-
culate the particle loss.

For control purposes, measurements were made with pions of 1.5
GeV/c in which 4 cm scintillators were placed as absorbers at
various points of the system. For an absorber at the location
of S2, a count rate change of 9 $\pm$ 4% as compared to the arrange-
ment without the absorber resulted. The change in the accept-
ance as a result of the additional coulomb scattering is 1.5 $\pm$ 1%
so that the particle loss resulting from the pronounced inter-
actions is calculated at 7.5 $\pm$ 7%. For a 4 cm scintillator,
a particle loss of 6% results with the total effective cross
sections at 3 GeV/c [26]. The above consideration therefore
appears justified. This does not apply to the adjacent coun-
ters of the pulse hodoscope S3 and S4 at the end of the
system. The elastic scattering is to yield no major loss, but
even for inelastic interactions of the pions, a response of the
subsequent counters resulting from secondary particles may be
expected with a certain amount of probability. The test mea-
surement with the absorber at this point yielded also only
count rate changes of 1.2 $\pm$ 1.4 %.

The material present up to and including S2 (3.5 cm liquid hydrogen, 4 m air, 1.5 cm scintillator) under the conditions mentioned above, results in a particle loss of 3.5%; for the pulse hodoscope and S3, a sum of 1% is assumed. We therefore obtain

$$f_{abs} = (-0.045) = 0.995$$

with an error of about 2%.

3.6) Survey of Other Corrections

The measured particle rate must be corrected for random coincidences, dead time, non-response of the main coincidence, unclear events in the hodoscope, uncertainty in the separation of pions from protons, background in the fligh time spectrum. These points are investigated in greater detail in the Appendix VI.2 to VI.4. The following results are obtained:

a) The main coincidence result contains an error of less than 1% due to the effects listed above, so that no correction need be made;

b) Unclear events in the hodoscope lead to a deterioration of the angle and pulse definition in several per cent of the events; a correction for count rate losses as a result of non-response of the hodoscope is made;

c) Uncertainty in the pion/proton separation leads to an increase in statistical error of the measurement points only at the highest pulses (a factor of 1.2 at 2.7 GeV/c, cf

Fig. 34); the correction for the pion rate reaches a max-
imum of 2% for high pulses and is negligible for low
pulses;

d) A correction is made for the background in the flight time
spectrum by increasing the measured pion rate by 1% (0.5%)
at $\theta = 8^o$ (10°) and this is added linearly to the statis-
tical error of 1% (0.5%) for $12^o \leq \theta \leq 20^o$, the correction
disappears.

Finally, the quantameter indication must be corrected with the
aid of a monitor telescope (see II.2.5). The change usually
was clearly below 1%.

III.4) Systematic Errors

Table 2 shows a summary of the systematic errors estimated in
III.3 and in the Appendix in greater detail.

Table 2: System Errors	
Quantameter and integrator	± 5%
Acceptance	± 5%
Correction factor for the Brems spectrum	± 2%
Density of target atoms, empty target correction	± 1%
Absorption correction	± 2%
Response capability, dead time, random co-incidences in the main coincidence	± 1%
Unclear events in the directional hodoscope	± 1 to 3%
Unclear events in the pulse hodoscope	± 2%
Background in the fligh time spectrum	± 0 to 2%

Under the assumption that these errors are independent, a total systematic error of $\pm$ 9% results. (The individual errors are added quadratically.)

IV. Events and Theoretical Interpretation

IV.1) Effective Cross Sections[*]

1.1) Tables

The differential effective cross sections dσ/dt are given in Table 4 as a function of the square of the 4-pulse transfer t with γ energy k as a parameter. The values were calculated in accordance with the averaging process described in section III.2, taking into account all the corrections given in section III. For the classification into t and k the following interval limits were selected:

---

[*]Results of the experiments have already been published [29]. In the earlier values, the following corrections have not yet been taken into account: change of quantameter constants based on new measurements (cf [16,17]), consideration of intensity profile of γ-ray, correction for gas in the empty target, smaller nuclear absorption in the counters at the system end, errors due to flight time separation and background in the flight time spectrum. These relatively small individual effects almost cancel each other when added so that the effective cross sections at $\theta \geq 12^\circ$ by less than 1% as compared to [29]. At 8° a change of about 1% occurs as against [29], at 10°, 0.5%; the errors of the measurement points at these angles are now 1% and 0.5% greater.

Table 3:   Limits in k and t for calculating dσ/dt (-t)

Limits in k (GeV)							
1.13	1.27	1.415	1.55	1.69	1.875	2.075	2.275
2.50	2.75	3.00	3.45				

Limits in -t ((GeV/c)^2)							
0.01	0.033	0.058	0.083	0.108	0.133	0.160	0.193
0.230	0.273	0.323	0.375	0.430	0.490	0.550	0.613
0.678	0.748	0.823	0.895	0.965	1.038	1.113	1.188
1.263							

The limits are so dimensioned that in averaging over the corresponding intervals, no substantial amount of structure is lost. On the other hand, the statistical error is kept sufficiently small (about 5%).

The errors of the effective cross sections given in Table 4 contain the statistical errors resulting from the count rates in which the effect of the empty target subtraction is also taken into account. Furthermore, the error produced by the pion-proton separation (VI.4.3) and for the data at 8° and 10° laboratory angle an uncertainty of 1% and 0.5% for background in the flight time spectrum. This is added linearly to the statistical] errors. Systematic errors which would affect all measurement points roughly in the same manner were not taken into account (III.4). The absolute values therefore contain an uncertainty factor of $\pm$ 9%.

Table 6 shows the differential effective cross sections dσ/dΩ*

as a function of the γ energy k for fixed pion center-of-mass angles Θ* with the interval limits given in Table 5. The values for the effective cross sections and their errors were determined accordingly as above.

Table 5:   Limits in k and Θ* for calculating the $\frac{d\sigma}{d\Omega *}(k)$

Limits in k (GeV)							
1.145	1.25	1.28	1.40	1.42	1.55	1.69	1.85
1.90	2.05	2.10	2.25	2.30	2.45	2.55	2.70
2.80	2.95	3.10	3.22	3.35			

Limits in Θ^{*} (degrees)							
7.5	12.5	17.5	22.5	27.5	32.5	37.5	42.5
47.5	52.5	57.5					

1.2) Graphic Representation

Fig. 21a to k show $\frac{d\sigma}{dt}$ as a function of -t in semi-logarithmic representation for γ energies of 1.20 to 3.25 GeV. Above 1.75 GeV, we obtain in this representation an approximately linear decrease as the pulse tranfer proceeds. A function in the form of

$$\frac{d\sigma}{dt} = A \exp(Bt)$$

is matched to the effective cross section. Table 7 shows the values for A, B, X^2 and the number of the degrees of freedom NF.

Table 4: $\frac{d\sigma}{dt}$ for the reaction $\gamma + p \rightarrow \pi^+ + n$ as a function of $-t$

dσ/dt (μbarn/(GeV/c)²)

Laboratory energy of photons in GeV

$-t(\frac{GeV}{c})^2$	1.20	1.34	1.48	1.62	1.78	1.98
0.02	29.7 ±1.3	21.7 ±1.5				
0.05	28.2 ±1.1	20.8 ±0.7	18.9 ±0.8	17.9 ±0.9	16.1 ±0.9	14.7 ±2.1
0.07	34.4 ±0.9	24.8 ±0.9	19.0 ±0.7	14.4 ±0.6	14.5 ±0.5	12.8 ±0.6
0.10	34.7 ±1.1	26.1 ±0.8	18.8 ±2.7	14.2 ±0.8	13.6 ±0.5	11.9 ±0.5
0.12	33.7 ±1.2	24.9 ±1.0	18.5 ±0.6	15.2 ±1.0	13.6 ±0.5	11.2 ±0.5
0.15	33.2 ±1.1	26.7 ±1.0	16.5 ±0.7	14.3 ±0.5	12.1 ±0.5	10.6 ±0.4
0.18	31.5 ±1.2	22.7 ±0.7	17.0 ±0.7	10.9 ±0.5	11.6 ±0.4	8.90±0.32
0.21		22.8 ±0.9	15.7 ±0.4	11.2 ±0.4	9.79±0.39	8.76±0.29
0.25		19.4 ±3.5	14.1 ±0.5	9.60±0.29	8.07±0.28	6.89±0.29
0.30			11.5 ±1.4	7.89±0.29	6.76±0.21	6.20±0.28
0.35				5.68±0.72	5.95±0.22	5.04±0.18
0.40					5.13±0.53	4.54±0.16
0.46						3.46±0.20

$-t(\frac{GeV}{c})^2$	2.18	2.39	2.63	2.88	3.23
0.05			7.25±0.88		
0.07	9.86±0.57	7.33±1.01	6.77±0.50		
0.10	9.20±0.42	6.93±0.38	5.62±0.44		
0.12	9.78±0.37	6.23±0.34	5.71±0.37	4.65±0.50	
0.15	8.75±0.33	6.66±0.30	4.45±0.29	4.00±0.30	
0.18	7.77±0.46	5.58±0.26	4.21±0.23	3.31±0.25	
0.21	7.45±0.44	5.81±0.25	4.05±0.22	3.18±0.26	
0.25	6.84±0.26	5.36±0.24	3.93±0.21	3.17±0.22	
0.30	5.03±0.22	3.94±0.17	3.47±0.15	2.79±0.30	
0.35	4.55±0.22	3.45±0.15	2.82±0.16	3.11±1.20	
0.40	3.99±0.15	2.93±0.15	2.25±0.12	2.31±0.20	
0.46	2.86±0.11	2.52±0.12	2.35±0.12	2.05±0.13	
0.52	2.29±0.11	2.21±0.10	1.75±0.11	1.36±0.11	
0.58	1.45±0.22	1.67±0.09	1.39±0.07	1.39±0.10	
0.65		1.17±0.13	1.13±0.07	1.11±0.09	
0.71			0.97±0.07	0.95±0.05	0.75±0.14
0.79			0.80±0.09	0.76±0.05	0.62±0.06
0.86				0.62±0.06	0.51±0.04
0.93				0.64±0.09	0.41±0.05
1.00					0.35±0.06

Table 6: The differential effective cross section $\frac{d\sigma}{dt}$ for the reaction $\gamma + p \to \pi^+ + n$ as a function of the pion center-of-mass angle and the laboratory energy of the photon.

k(GeV)	$d\sigma/d\Omega^*$ (µbarn/sterad) Pion production angle in the center-of-mass system							
	15°	20°	25°	30°	35°	40°	45°	50°
1.20	3.68±0.15	4.05±0.15	4.37±0.11	4.36±0.14	4.41±0.11	4.06±0.20		
1.34	2.96±0.13	3.60±0.13	3.77±0.09	3.75±0.12	3.55±0.09	3.37±0.13		
1.48	3.23±0.15	3.15±0.11	3.32±0.17	2.87±0.08	2.70±0.07	2.44±0.07		
1.62	3.43±0.17	2.72±0.10	2.87±0.14	2.43±0.07	2.03±0.06	1.61±0.04	1.05±0.11	
1.77	3.31±0.17	2.91±0.10	2.72±0.07	2.36±0.06	1.78±0.06	1.39±0.04	1.17±0.06	
1.98	3.01±0.18	2.88±0.08	2.47±0.06	2.04±0.05	1.64±0.06	1.19±0.03	1.00±0.03	
2.18	2.63±0.20	2.45±0.07	2.35±0.06	1.86±0.07	1.42±0.05	1.04±0.03	0.69±0.02	0.38±0.07
2.38	2.15±0.25	1.92±0.07	1.71±0.05	1.51±0.05	1.04±0.03	0.81±0.03	0.58±0.02	0.41±0.03
2.63	2.16±0.12	1.65±0.08	1.38±0.04	1.19±0.04	0.83±0.03	0.67±0.03	0.42±0.02	0.33±0.02
2.88		1.47±0.08	1.14±0.06	1.07±0.09	0.80±0.05	0.53±0.04	0.37±0.02	0.26±0.01
3.16							0.25±0.03	0.22±0.03
3.29							0.25±0.03	0.17±0.01

Fig. 21 a,b: $\frac{d\sigma}{dt}$ as a function of t cf with measurements obtained by Kilner [5].

Fig. 21 c,d,e

f) 1.98 GeV

g) 2.18 GeV

Fig. 21 f,g

h) 2.39 GeV

i) 2.63 GeV

Fig. h,g
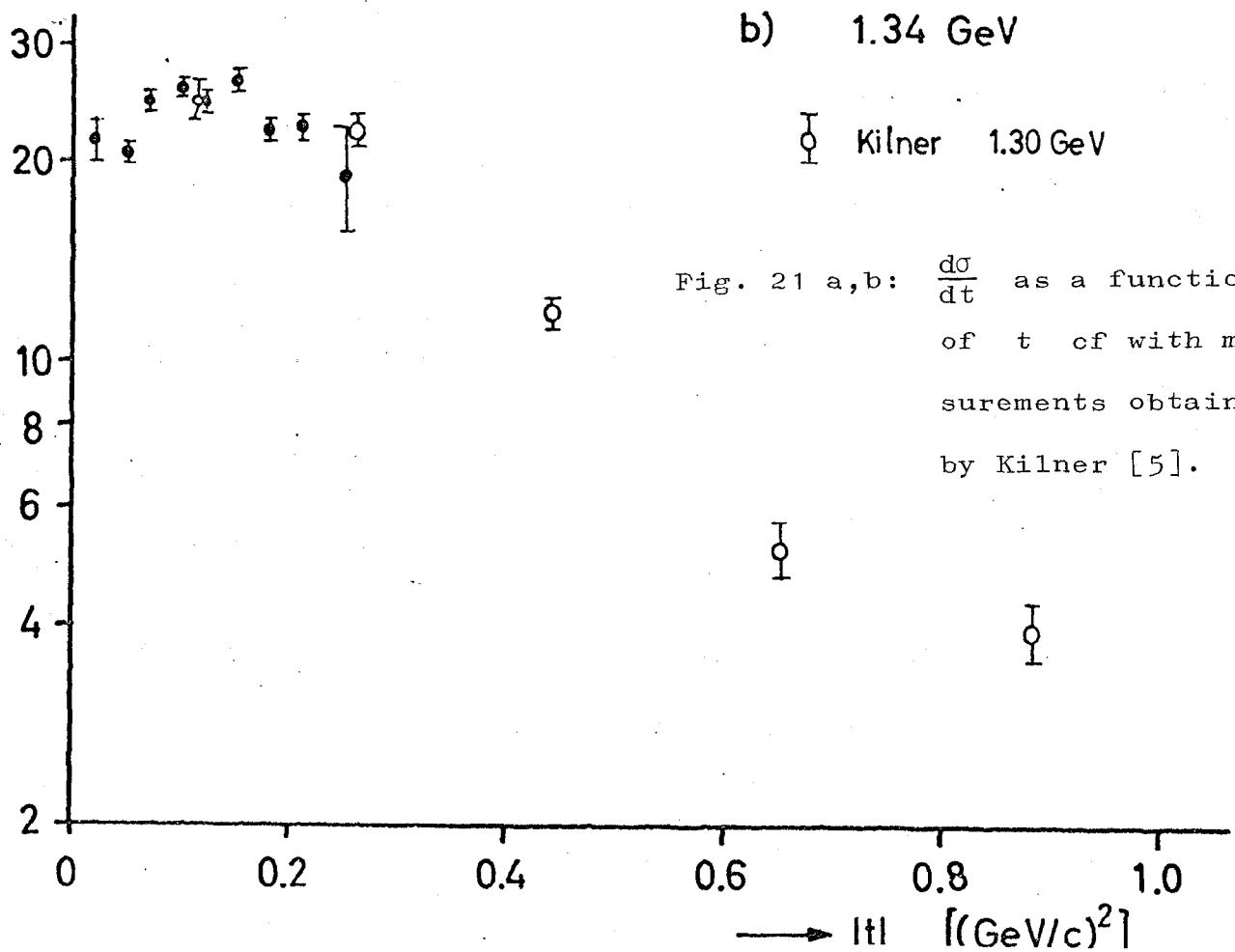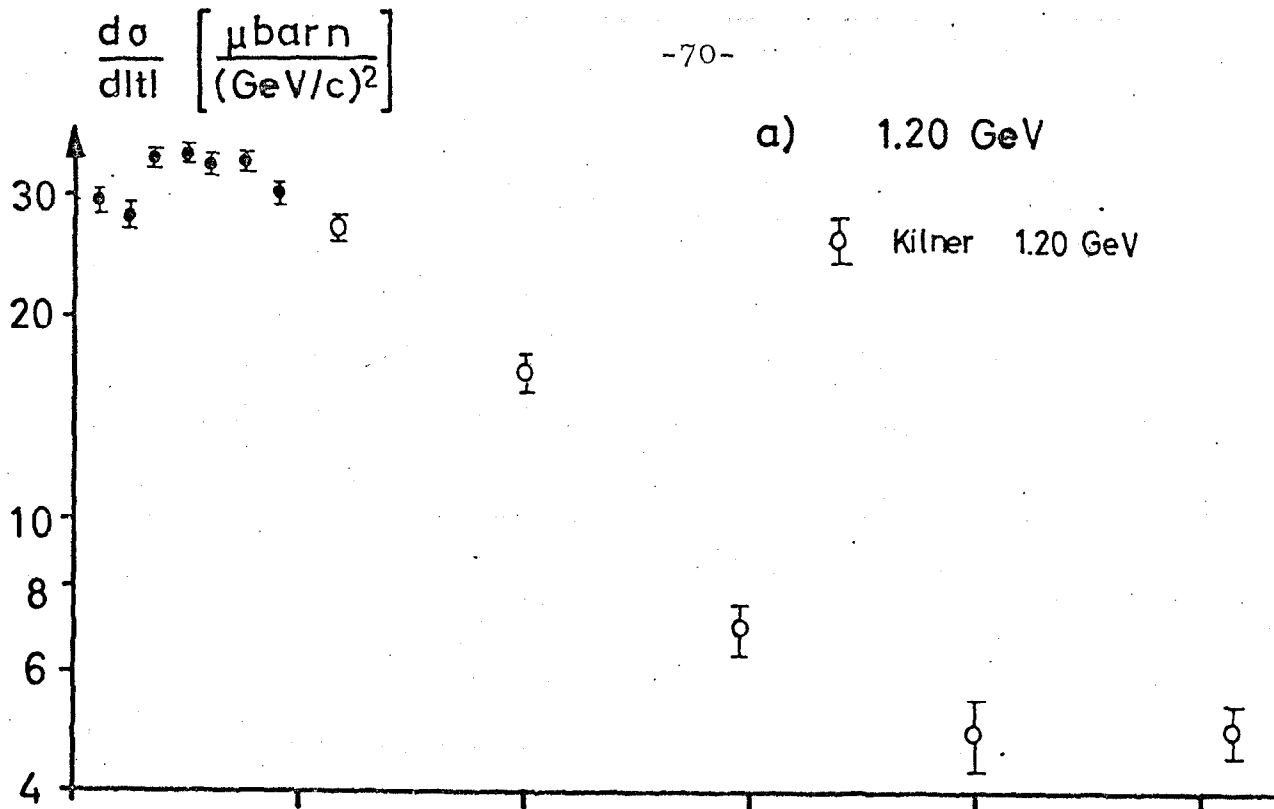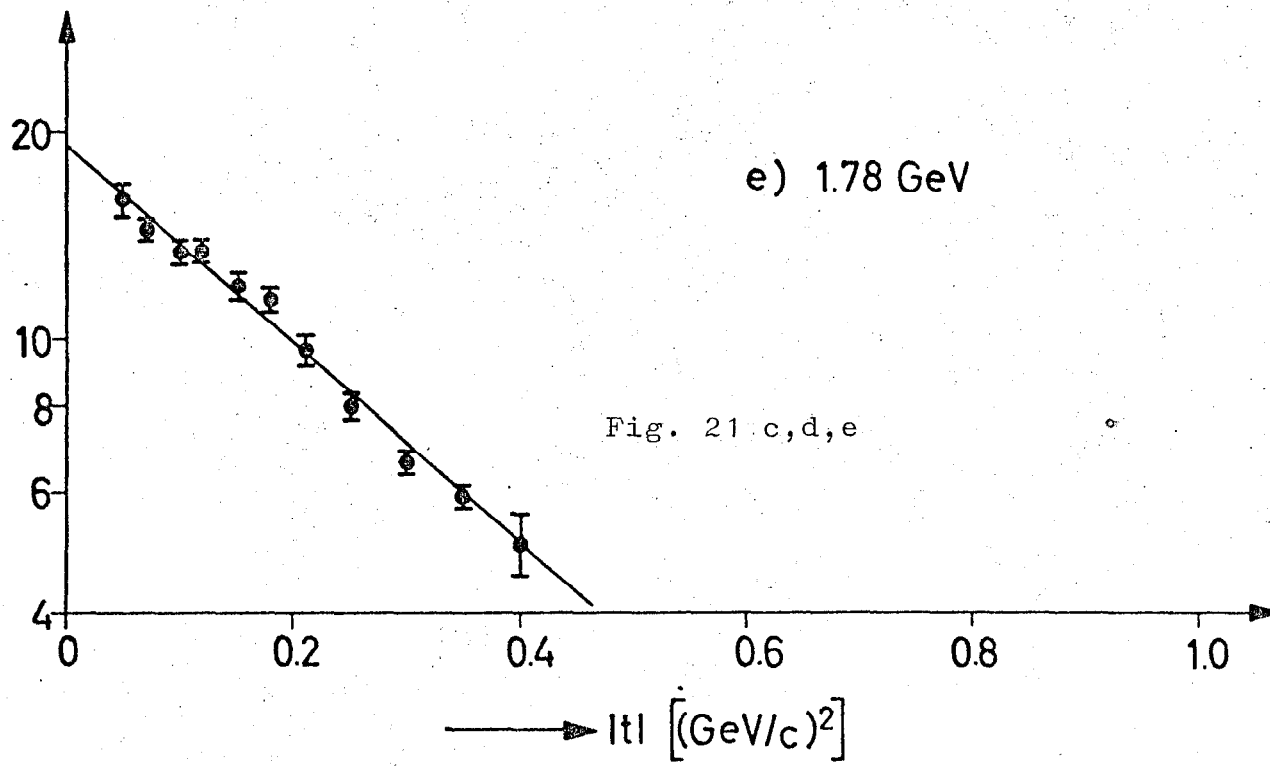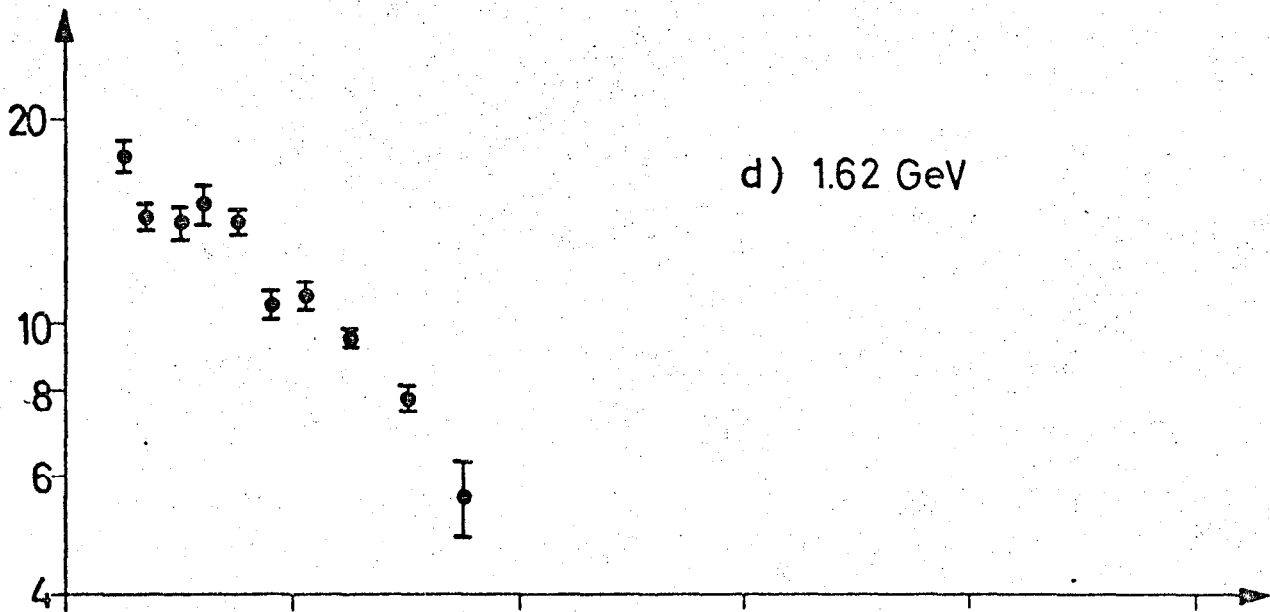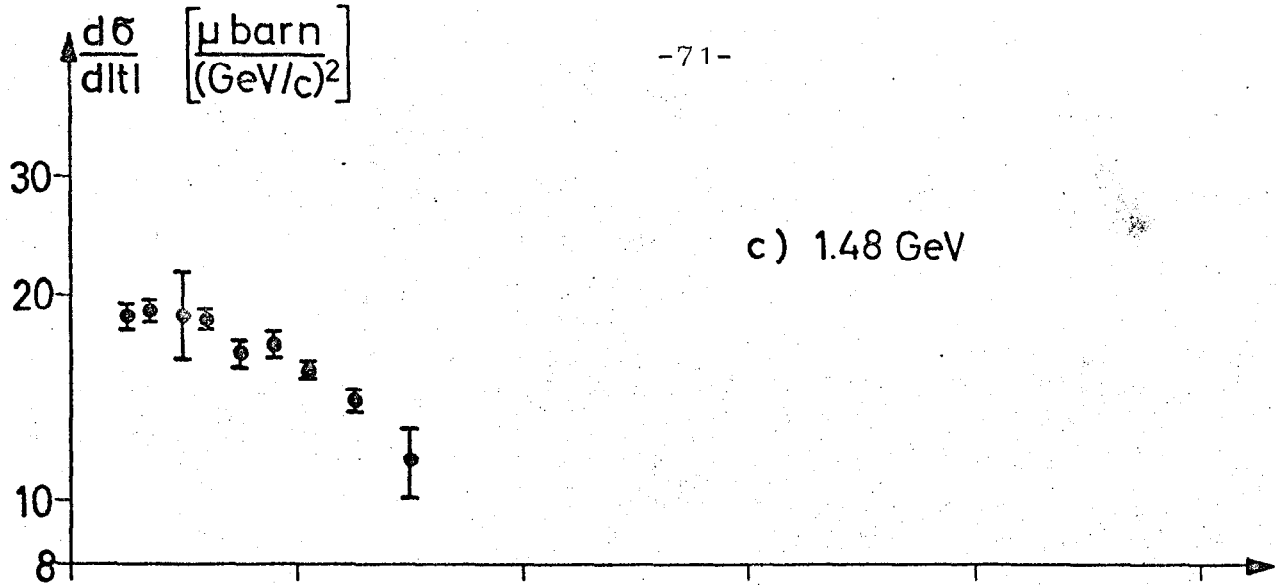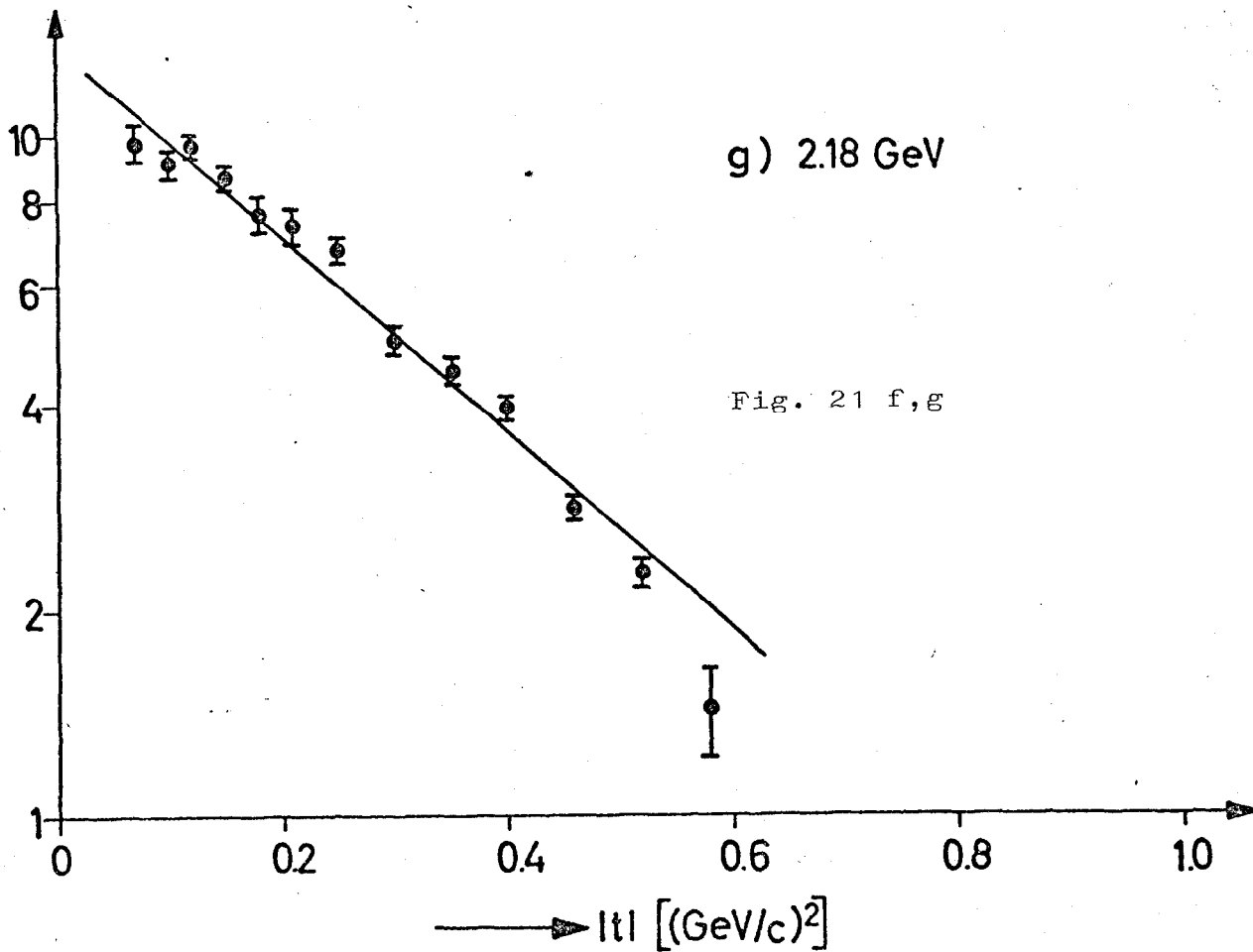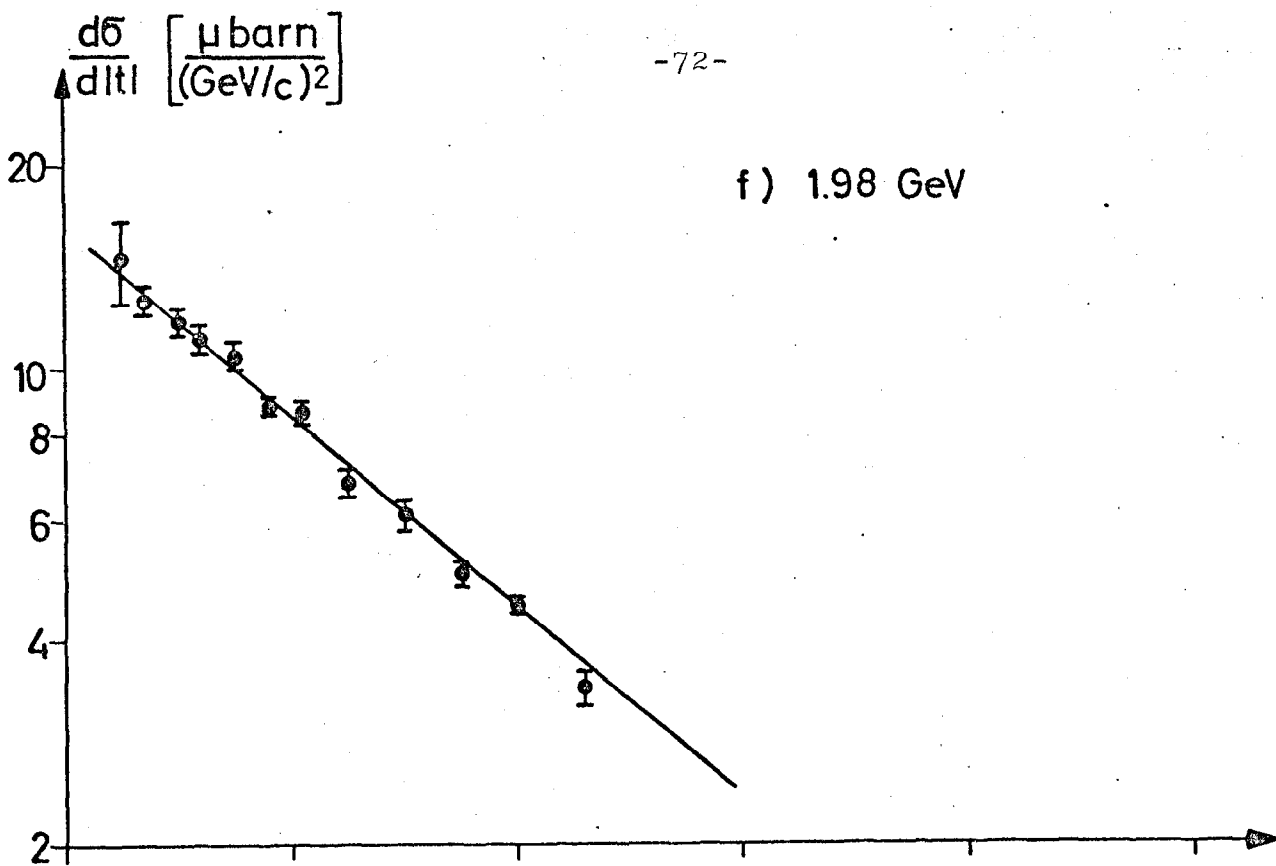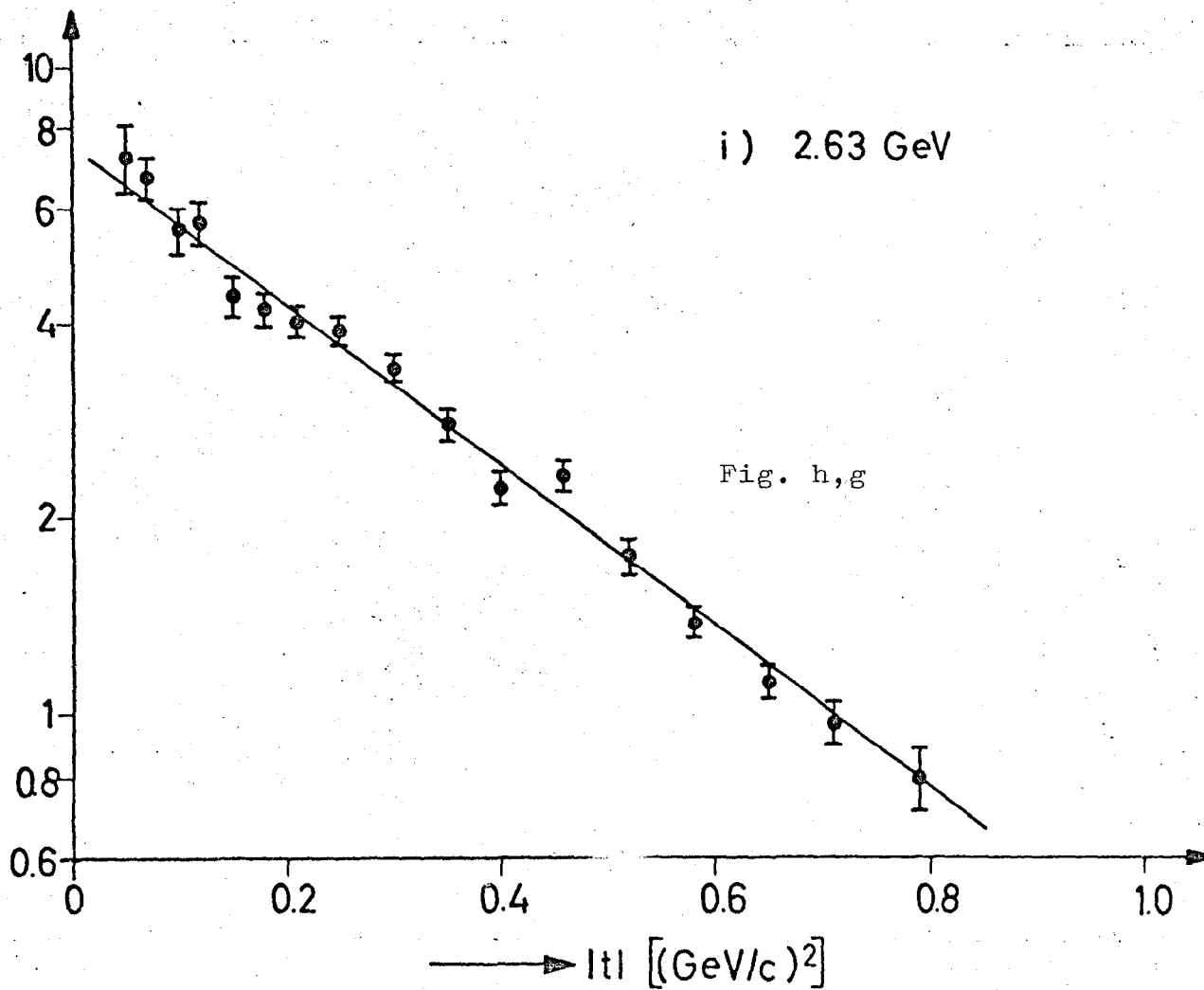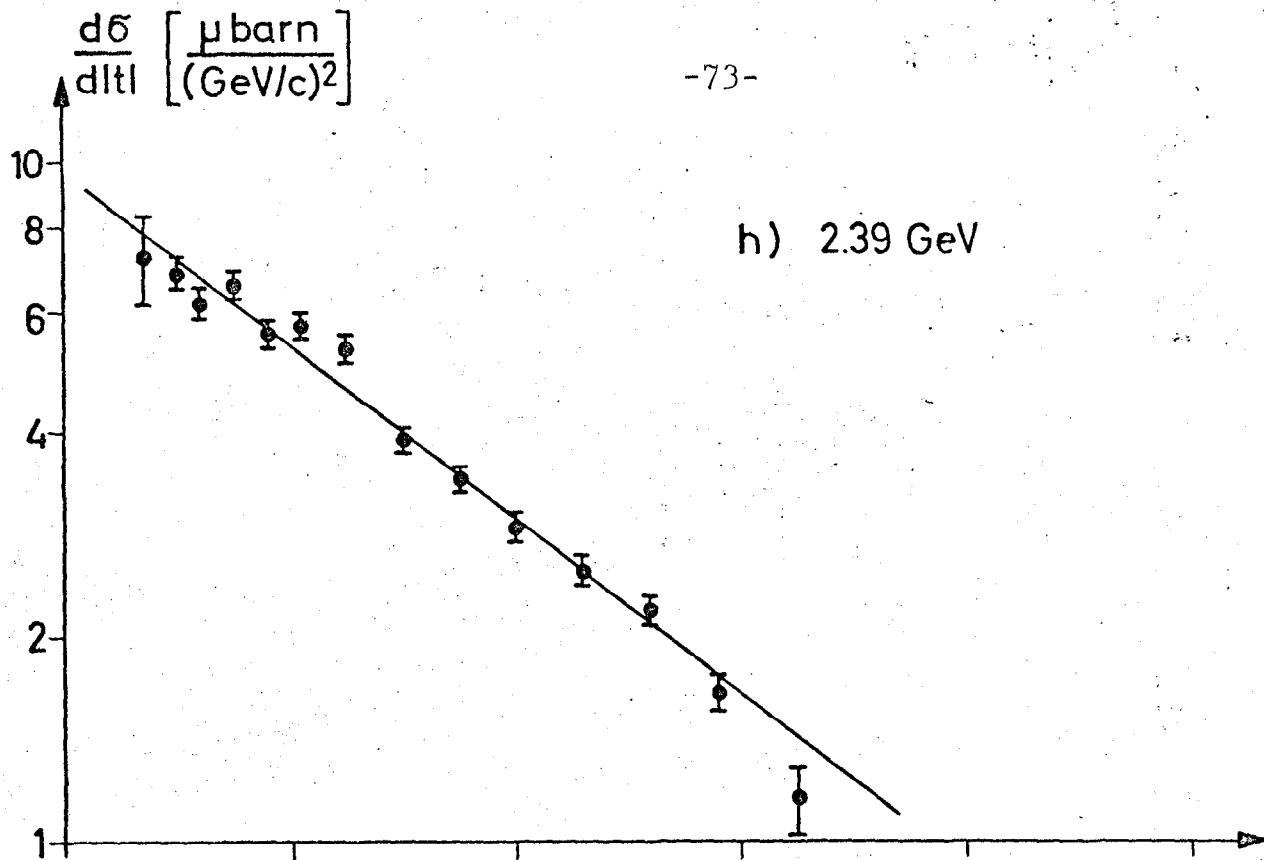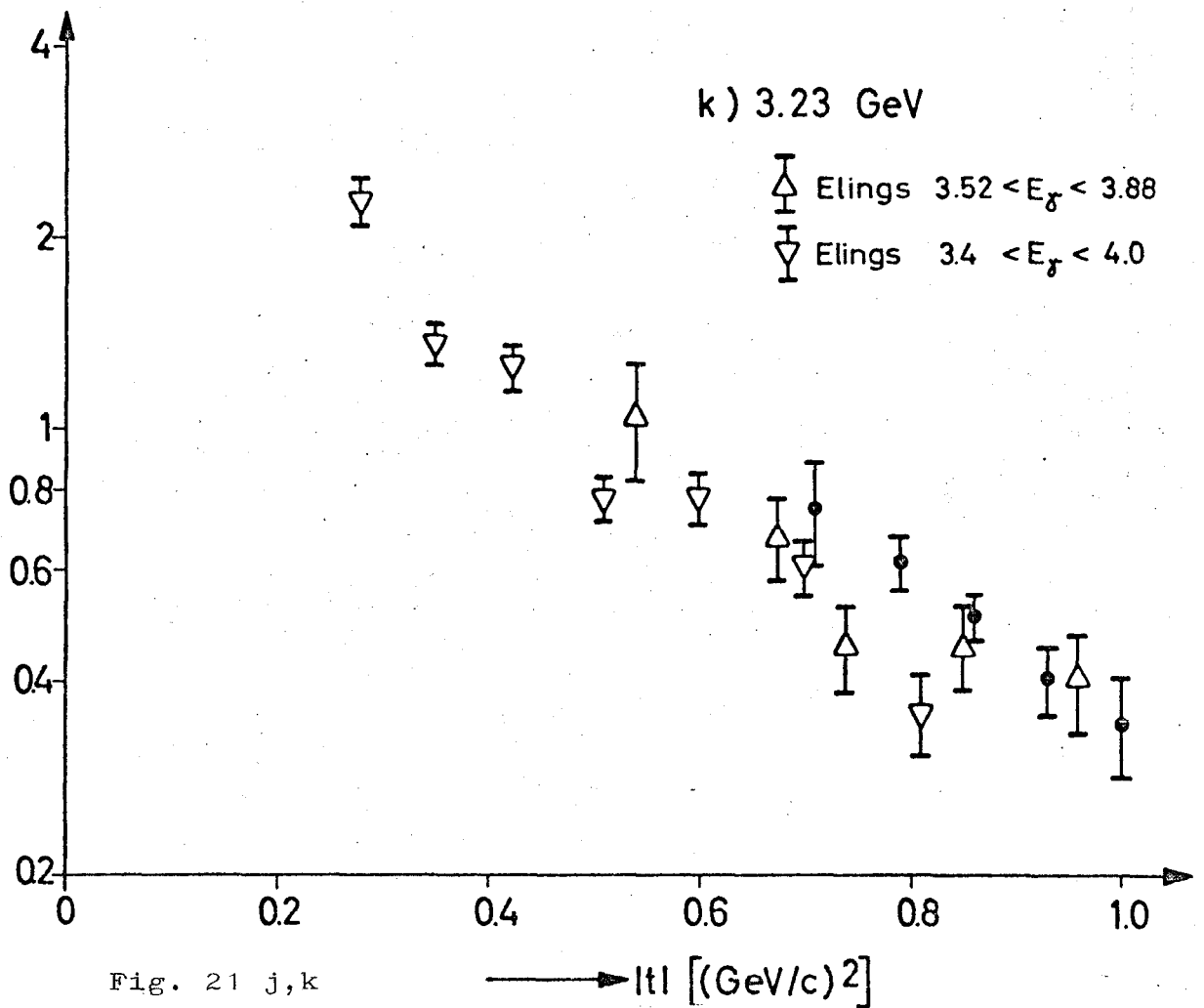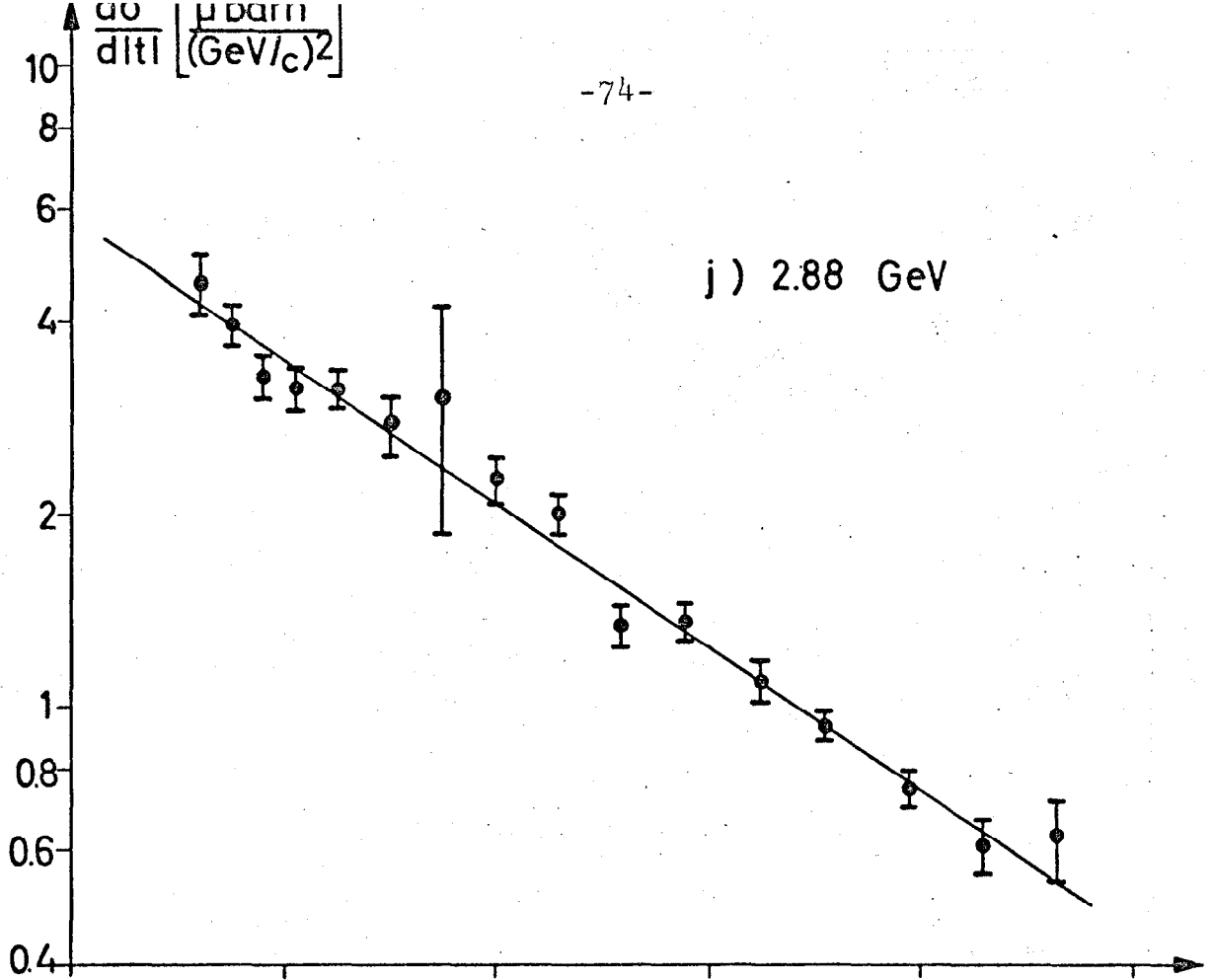
Fig. 21 j,k
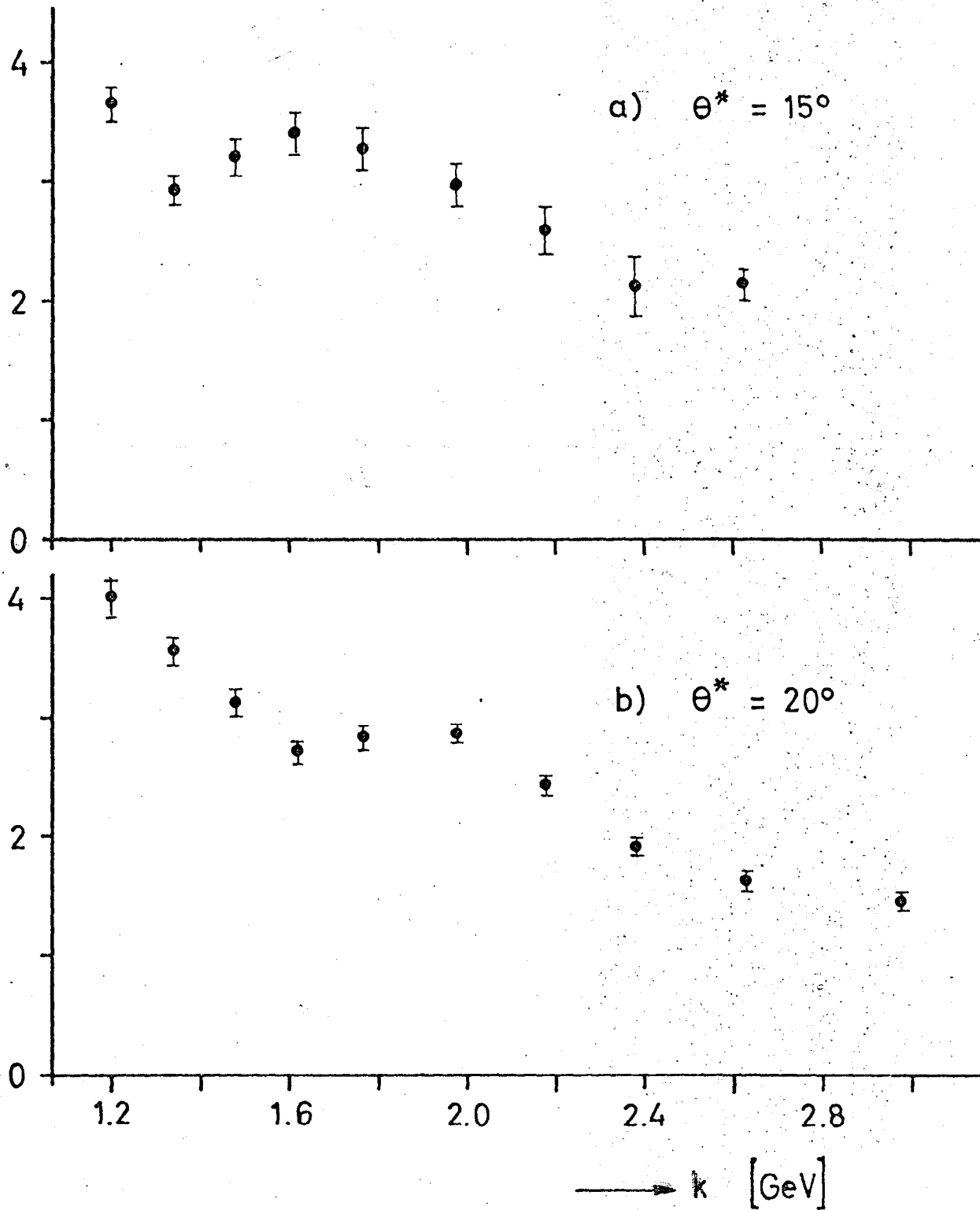
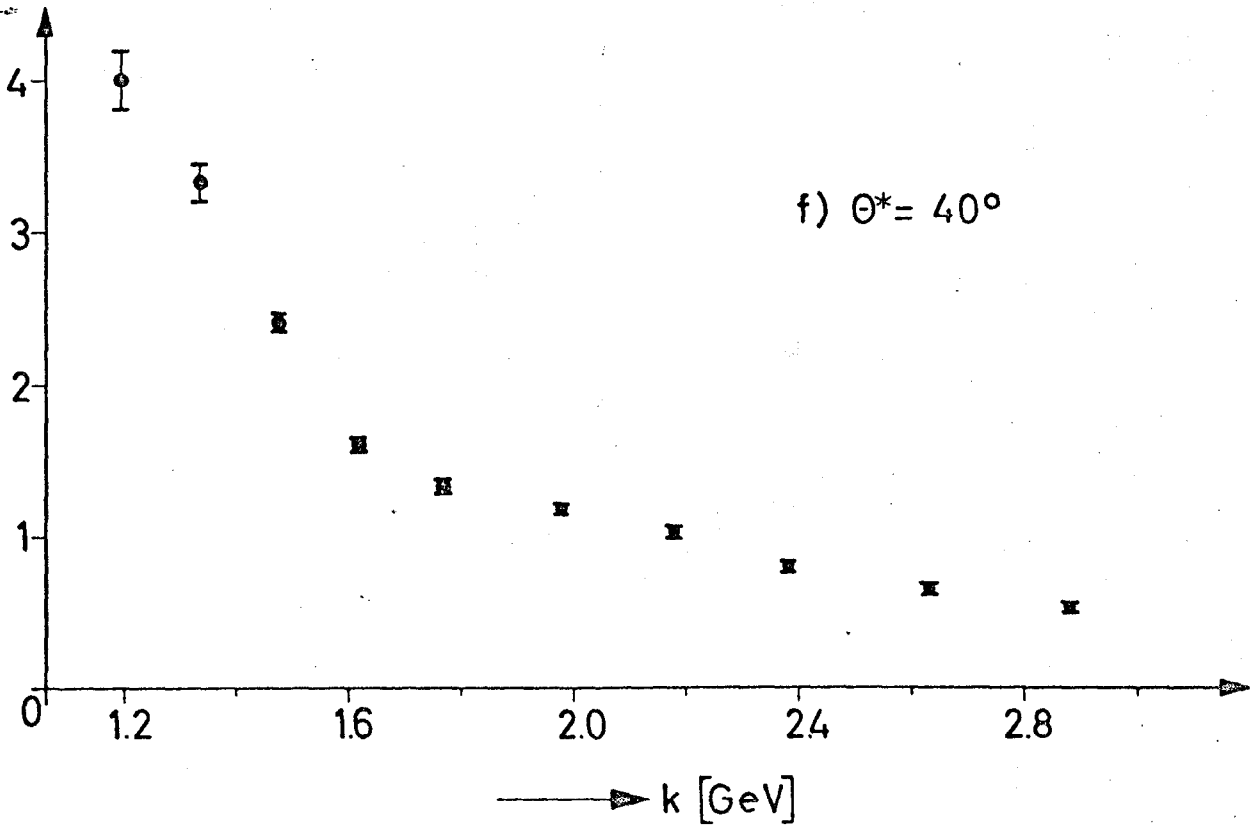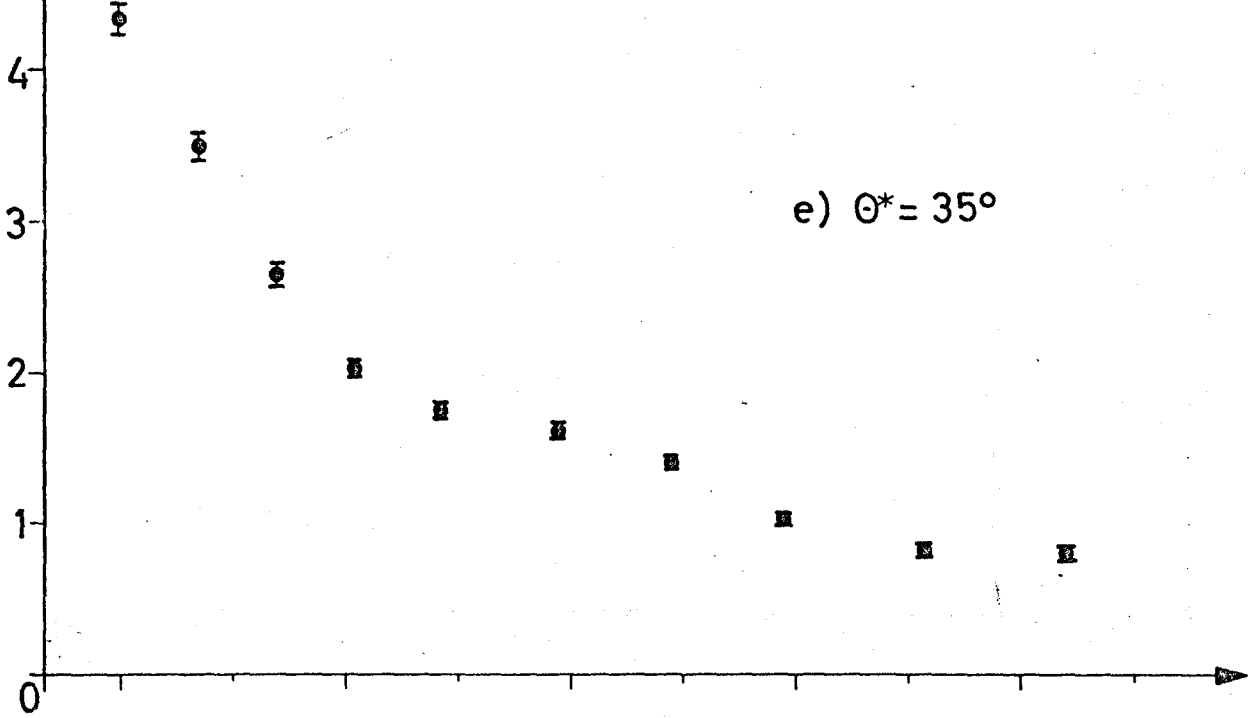Fig. 22 a,b: $\frac{d\sigma}{d\Omega}*$ as a function of γ energy k.
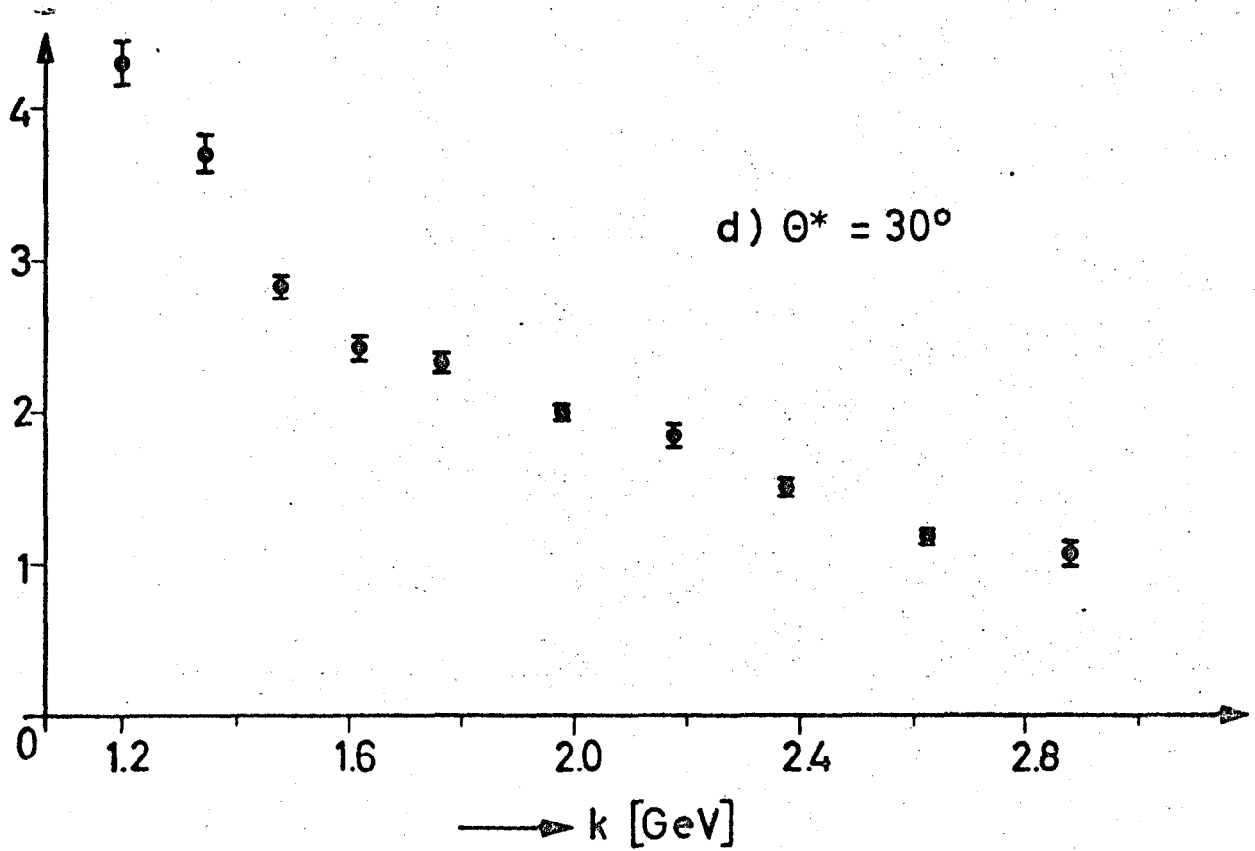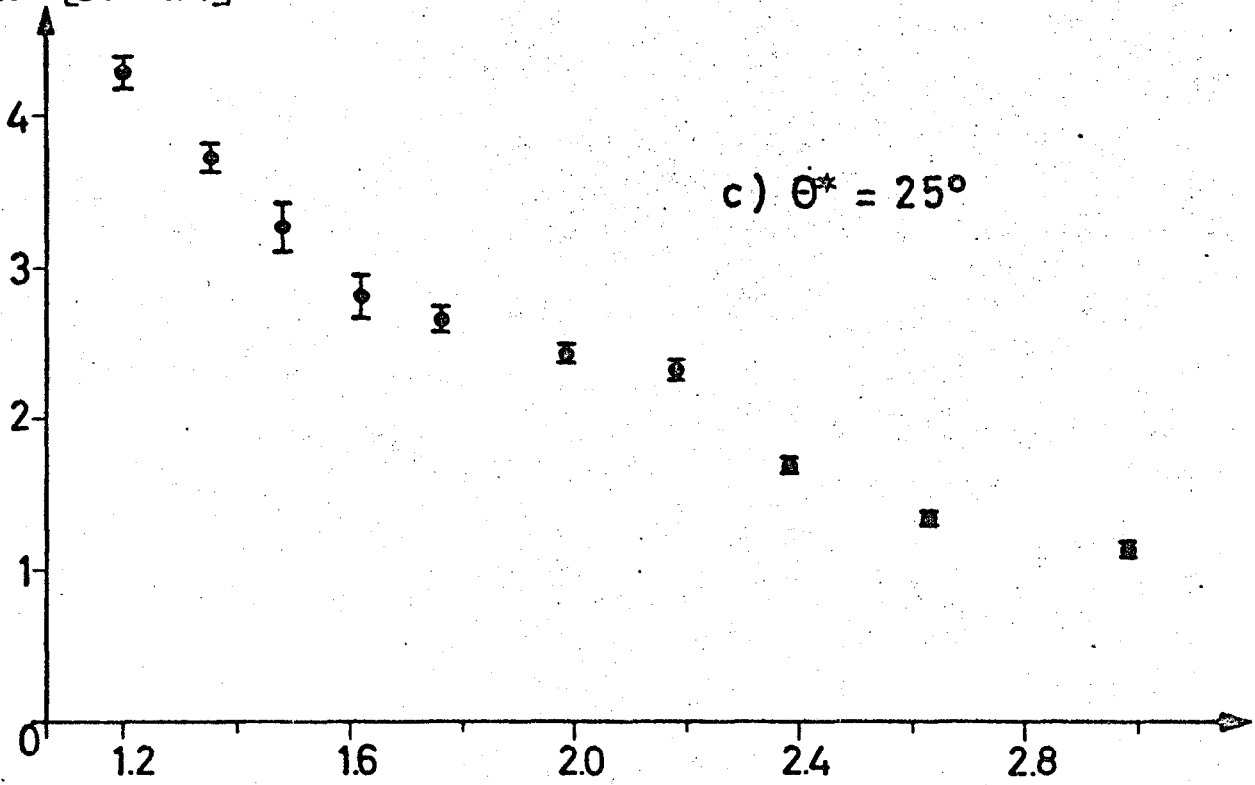
Fig. 22 c,d

Fig.22 e,f
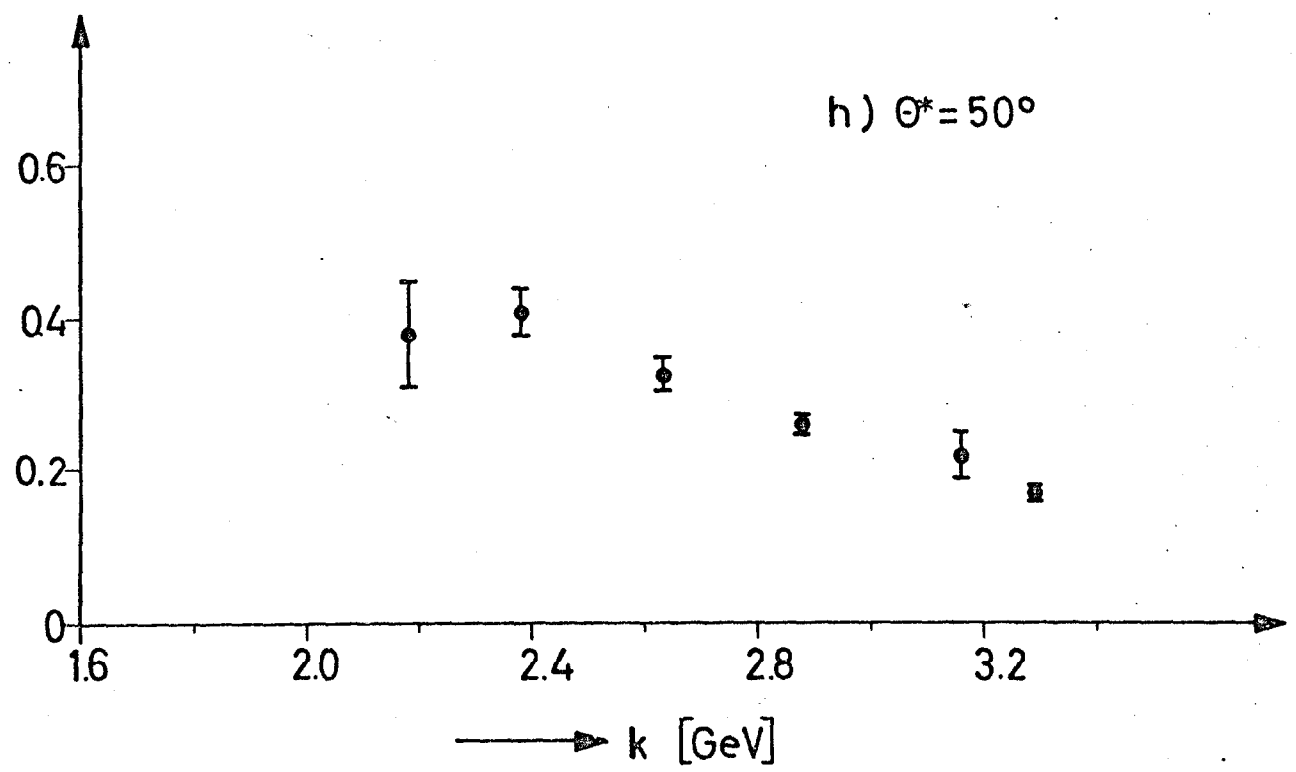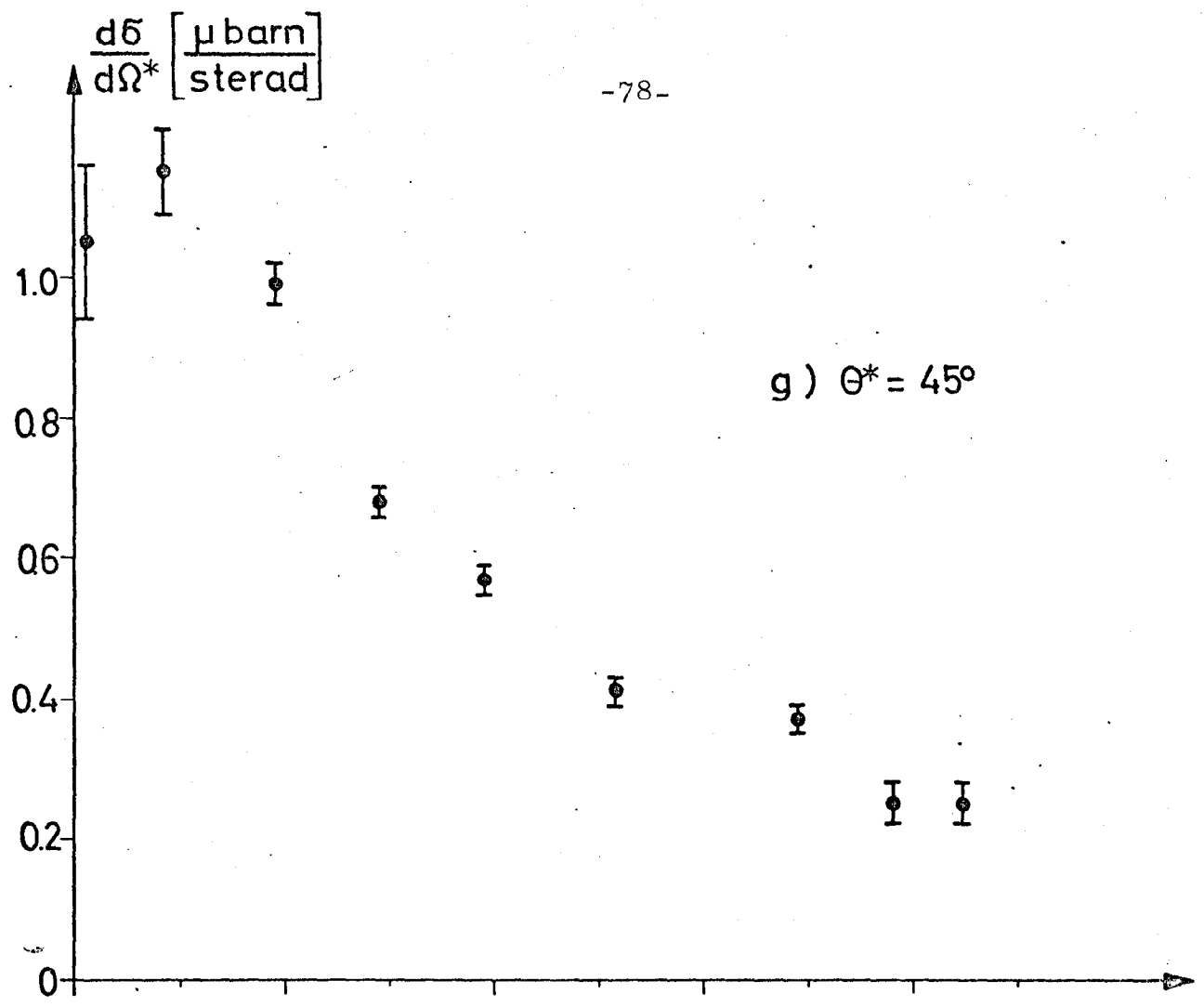
Fig. 22 g,h

Table 7 : Adaptation of a function A exp(Bt) to the effective

cross section $\frac{d\sigma}{dt}$

k(GeV)	A(μbarn/(GeV/c)^2)	B((GeV/c)$^{-2}$)	χ^2	NF
1.78	19.10 ± 0.45	3.32 ± 0.11	17.8	9
1.98	16.20 ± 0.40	3.22 ± 0.10	9.7	9
2.18	13.70 ± 0.31	3.31 ± 0.08	47.1	11
2.39	9.65 ± 0.25	2.94 ± 0.08	32.0	12
2.63	7.56 ± 0.19	2.86 ± 0.07	27.7	15
2.88	5.78 ± 0.20	2.55 ± 0.07	20.6	14

Although a parameter representation of this type describes the general behavior quite well, the adaptation at some energy values is rather poor since it results from the ratio χ^2 : N_f. As the photo energy increases, the exponential decrease of the effective cross section becomes less pronounced.

For the π^+ photo production data obtained by Elings et al [9,10], which were averaged for energy values from 3.52 to 3.88 GeV, a similar behavior resulted with a value B = 3.0 ± 0.3 (GeV/c)$^{-2}$. Likewise, the π^o photo production [30] and the $K^+\Lambda^o$-, $K^+\Sigma^o$ photo production [9,10] show an approximately exponential t dependence in the GeV range for large values of |t| (up to about 1 (GeV/c)^2. Since for π^+ photo production incoming and outgoing particles have different quanta numbers, a simple comparison is not feasible with the defraction scattering observed during the interaction of hadrons which for B yields values of ~8 (πN scattering) and ~10 (NN scattering). In section IV.5, however,

a model is being observed which connects the pion-photong production with the ρ production at pion-nucleon interactions for which an approximately exponential t relationship has also been found.

The effective cross sections agree fairly well for the low energy values (1.20, 1.34 GeV) with the Kilner [5] values. The coincidence with the Elings et al [10] measurements is also satisfactory, although here some uncertainty is present since in this experiment the highest γ energy was approximately 3.25 GeV, while in [10] an average was obtained over an interval ranging from 3.4 to 4.0 GeV. π^+ photo production measurements recently were also being conducted by Caldwell et all [31]. In the overlapping range, the results are compatible.

The variation of the differential effective cross section $\frac{d\sigma}{d\Omega}*$ as a function of the γ energy k is shown in Fig. 22 a to h for the center-of-mass angle from 15° to 50°. The curves first decay steeply at the lower energies and less steeply at the higher energies. However, a maximum or a shoulder always occurs for photon energies between 1.5 and 2 GeV. In this range, the nucleon-isobars can be produced with the masses 1924 and 2190 GeV. For very small angles ($\theta^* = 5^\circ$ and 2.5°), the structure becomes significantly clearer [12]. The maximum shifts systematically toward the smaller energy values as the angles decrease.

IV.2) The Peripheral Model

Within the range of several GeV we observed a clear preference

for small scattering and production angles and thus of small

pulse transfers to the nucleon [32] in many pion-nucleon and

kaon-nucleon reactions as well as in the π^+ photo production

measurements shown here. This means that partial waves with a

high angular momentum, hence with a large shock parameters pre-

dominate, i.e. that the interaction is tranferred by peripheral

shocks. The "peripheral model" describes these processes as a

single particle exchange in the t channel (cf Fig. 22 a).

Taking into account the laws of conservation for charge, spin,

parity, and G parity, π^+ and ρ^+ exchanges are permitted in π^+

photo production.

As in all cases where the exchange of an elementary vector meson

has been calculate, an energy dependence of the effective cross

section also results here for a ρ exchange which is in sharp

contradiction to the experiment. The calculated effective cross

section $\frac{d\sigma}{dt}$ tends toward a non-disappearing constant for s → ∞,

while the experimental values decrease faster than $\frac{1}{s^2}$. By intro-

ducing form factors or by taking into account terminal state in-

teractions, the erroneous energy behavior can hardly be affected;

the only method so far known to avoid this "high energy catas-

trophy" consists of treating the ρ-meson as a Regge particle

(see IV.4).

One-pion exchange as shown in Fig. 23a yields an approximately

correct energy behavior (see below), however, the difficulty arises that the matrix element calculated from this diagram is by itself not calibration independent [32] and therefore no defined value can be attributed to it.
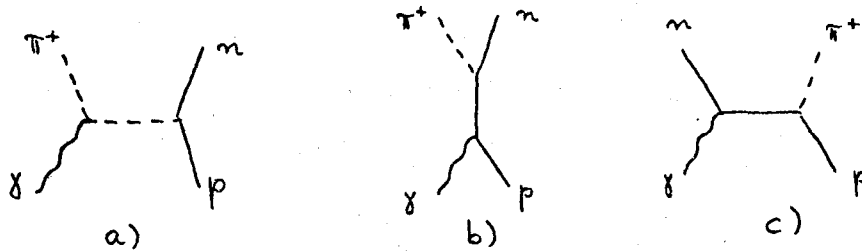

Fig. 23:   Some Feynman graphs of the lowest order for π^+ photo production (t, s and u channel)

Graph b) by itself is also not calibration independent, but the sum of the matrix elements a) and b) is calibration independent. Since the portion of Graph b) which spends from the normal magnetic moment (Dirac moment) of the proton, is already calibration invariant, it is sufficient to add the remaining "trajectory current portion" of b) to Graph a) ("minimum calibration independent expansion of the one-pion exchange"). In the limit case of none-too-small energy values we obtain for the sum of Graphs a) and b)

$$\frac{d\sigma}{dt} = \frac{1}{8\pi} (eg)^2 \cdot \frac{1}{s^2} \cdot \frac{m_\pi^4 + t^2}{(m_\pi^2 - t)^2} \tag{4}$$

and for the minimum calibration invariant expansion:

$$\frac{d\sigma}{dt} = \frac{1}{8\pi}(eg)^2 \frac{1}{s^2} \cdot \frac{2t^2}{(m_\pi^2 - t)^2} \tag{5}$$

$$\left(e^2/4\pi = \alpha = 1/137 , \quad g^2/4\pi = 14.5 \right) \qquad \text{(cf [33])}.$$

It becomes evident that two difficulties emerge: For one, due to the calibration independent expansion a basic assumption of the peripheral model is being violated since non-peripheral portions will have to be added. On the other hand, it has not been established how a calibration independent expansion must look --whether Form (4) of Form (5) is better or even if other diagrams must be added, since for example, the coupling to the anomalous magnet moment of the nucleons yields comparable contributions to the scatter amplitude for Graphs b) and c).

The effective cross sections according to Eqs. (4 and 5) increase for large values of $|t|$ toward a constant in strict contradiction to the experiment. Eq. (5) disappears for $|t| \to 0$, while Eq. (4) reaches a maximum in the forward diretion and a minimum for $|t| = m_\pi^2$. Qualitatively, the latter would be absolutely tolerable for the variation observed at the low energy values [3,4,5,12] if it could be accomplished that the calculated effective cross section is lowered for large values of $|t|$.

The t dependence of the differential effective cross section can be better adapted to the experimental results if the absorption corrections are taken into account (IV.3) or if the exchanged

particle is treated as a Regge pole (IV.4). In contrast with the πN interaction, a useful t dependence cannot be attained here with the aid of a form factor F(t) since this would violate the calibration independence.

IV.3) The Absorption Model*

The absorption model modifies the peripheral model by taking into account the interaction of the particles in the initial and terminal states where we can limit ourselves to the final state in photon-induced reaction. In the calculation it is assumed that the pion and the nucleon produce defraction scattering whereby partial waves with a low angular momentum are highly absorbed. Thus, the angular distribution predicted by the peripheral model is bunched in front and thus better matched to the experimental change. In the helical representation submitted by Jacob and Wick [34] the amplitudes are multiplied by the following factor:

$$g(j) = \left(1 - C \exp\left(-\alpha j^2 \right) \right)^{1/2}$$

(Model I in [33]),

where

j = Total angular momentum

$C = \sigma_{tot}/(4\pi A)$

$\alpha = 1/(2Aq^2)$

σ_{tot} = Total effective cross section of π-N defraction scattering

*For this section, cf specifically [33].

$A = R^2_{eff} /4$, R_{eff} = range of interaction

q = Pion momentum in the center-of-mass system

From the pion-nucleon scattering there results a value $C \approx 0.8$; for C = 1, s waves are almost fully absorbed (j = 1/2).

Fig. 24 shows the result of the calculation for a γ energy of 2 Gev and the experimental results. All electrical Born terms, i.e. the summation of Graphs a) and b) are taken into account. For C the maximum value of 1 was assumed since for C = 0.8 the calculated effective cross section decreases even less as a function of |t| . The following notations can be made:

(1) The order of magnitude of the effective cross section is correctly reproduced. The energy dependence which is largely unaffected by the absorption correction, is approximately correct.

(2) Despite the assumption of maximum absorption (C = 1) the calculated effective cross section decreases less for large values of |t| than the experimental cross section.

(3) The characteristic minimum at $t \approx m^2_\pi$, which stems from the interference between one-pion exchange and nucleon pole, is present in the calculated curves at all energy values. In the present experiment, however, it occurs only for energy values below 1.5 GeV [3,4,5,12], while for higher energy values it disappears completely so that for

$|t| \lesssim m_\pi^2$ very large discrepancies occur [35].

In the present form, the peripheral model with absorption correction is unable to describe satisfactorily the behavior for small momentum transfers in the high energy ranges. If in addition, we admit interferences with a spin 7/2 resonance $N_{1/2}^*$ (2190), we are better able to adapt the change of the experimental effective cross section at 2 GeV following estimation, by making the proper selection of the coupling constants [36].

IV.4) The Regge Pole Model

In the exchange of an elementary particle with spin j, there results in the limit case of high energies (cf [32])

$$\tag{6a}$$

For $j \geq 1$, the total effective cross sections diverge for high energy values. If the exchanged particle is treated as a Regge pole, we obtain an energy dependence value of the from

$$\tag{6b}$$

which stems formally from the above relationship if j is replaced by the value $\alpha(t_o)$ of the Regge trajectory at the particular point $t = t_o$. If $\alpha(t)$ is small or negative in the physical range of the reaction $(t < 0)$, Eq. (6b) yields a completely different energy response from that given by Eq. (6a).
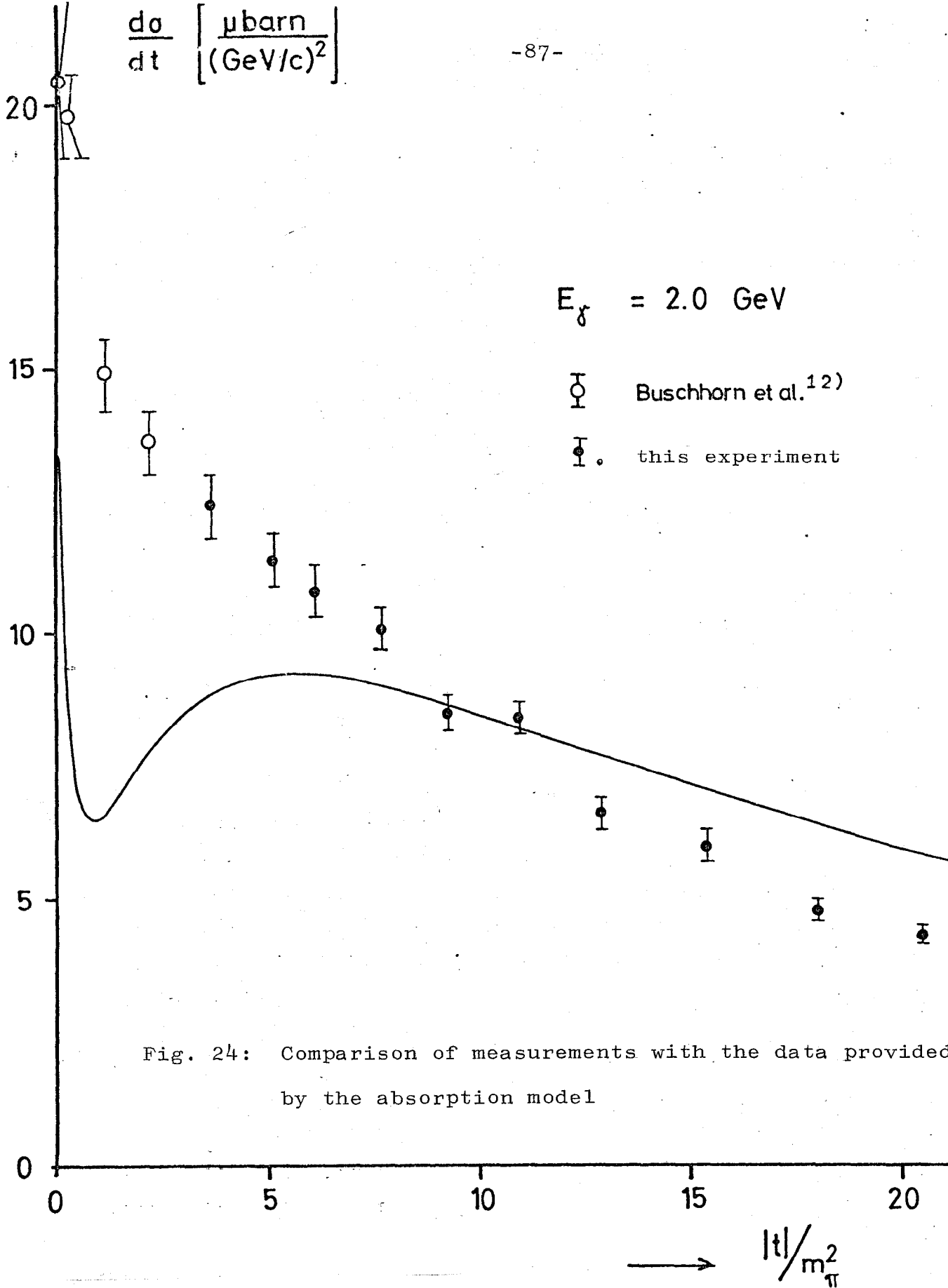
Fig. 24: Comparison of measurements with the data provided
by the absorption model

Regge models for the π^+ photo production have been proposed by several authors [37,38,39]. Caldwell et al [31] compared the t dependence of their π^+ photo production effective cross sections with the expression provided by Kramer and Stichel for the Regge π^+ exchange [37]. For higher values of t the coincidence is satisfactory. For $|t| \to 0$ there follows from the Regge model a lowering of the effective cross section which is incompatible with the results shown in Fig. 21. In addition, it should be noted that the data on the t dependence represents no accurate test of the Regge model since in the effective cross sectional formula an unknown function $\tilde{\beta}(t)$ emerges which had been assumed constant in Reference 31. A substantially more critical test is the s dependence of $\frac{d\sigma}{dt}$ for a constant value of t which in accordance with Eq. (6b) is to be written out as a power law. Fig. 25 shows as a typical example for the behavior of the experimental data at two t values the relationship between $\ln(\frac{d\sigma}{dt})$ and $\ln s$. The straight lines drawn in do not furnish a good adaptation (χ^2 per degree of freedom is 5 or 3). If we determine the values $\alpha(t)$ from the slope of the particular line involved, these do not show a simple response as a function of t as can be seen in the following table.

$-t$	0.045	0.070	0.095	0.120	0.25	0.35	0.40
$\alpha(t)$	+0.23	−0.14	−0.43	−0.30	−0.34	−0.15	−0.20

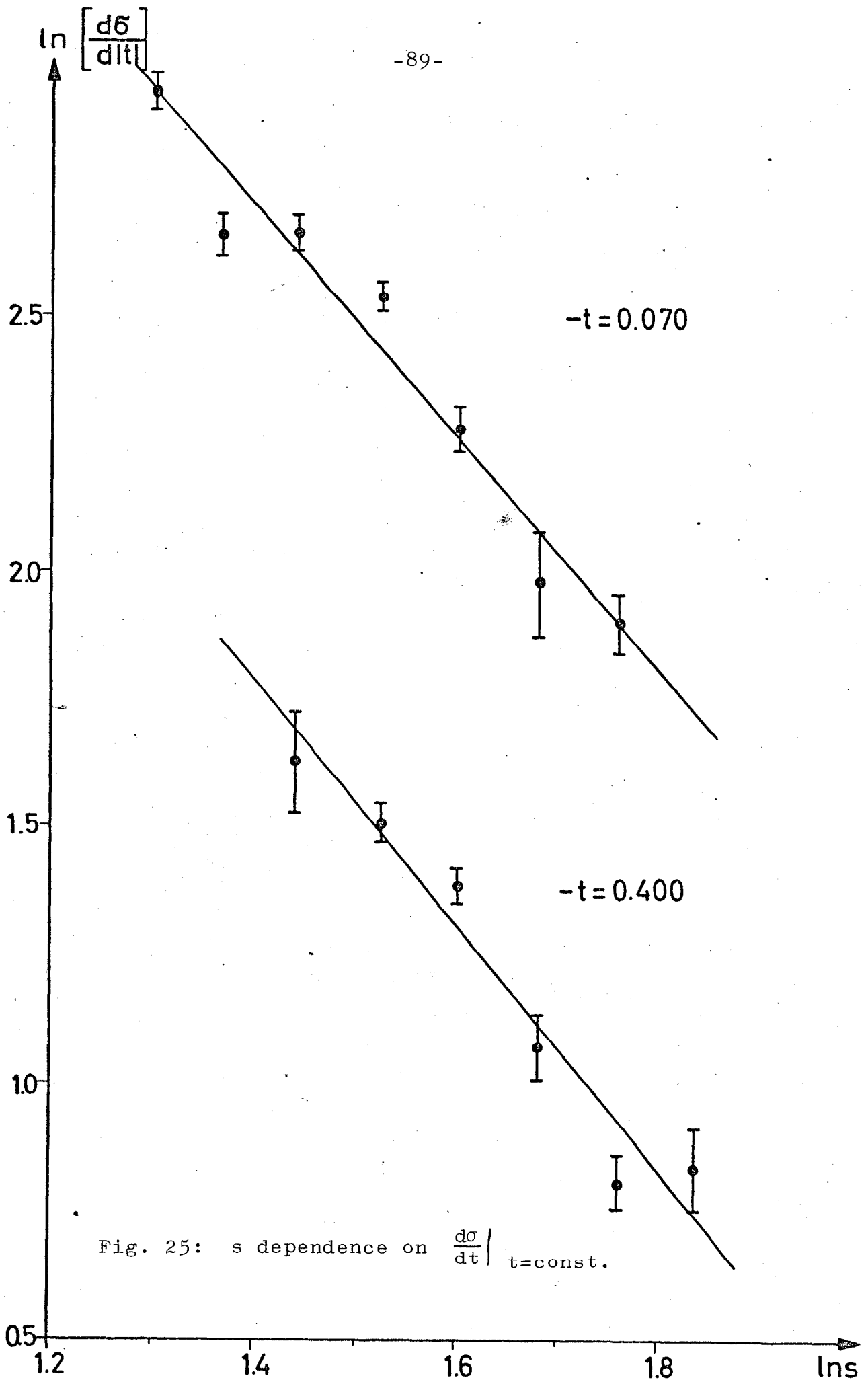Fig. 25: s dependence on $\frac{d\sigma}{dt}\Big|_{t=\text{const.}}$

The use of a Regge pole model appears to be doubtful in the present case for the following reasons:

a) The effective cross sections present a clear resonance structure so that we are surely still removed from the "asymptotic range" for which the simple Regge model (exchange in the p channel) provides data;

b) According to section IV.2, π and ρ exchanges are possible, but it is not known which one predominates; calculations regarding the interference of two Regge trajectories are not available.

In contrast with this, we were able to adapt measurements of the π^{o} photo production at 2 GeV [30] by the Regge ω exchange and an admixture of a multi-pole amplitude of the 2190 MeV pion-nucleon resonance by approximation [40]. The ω trajectory was assumed to be parallel to the ρ^{o} trajectory by Hohler et al [41].

IV.5) Vector Meson Predominance Model

In the vector meson predominance model, a coupling of the electromagnetic current to the vector meson currents of the form [42]

$$ j_{\mu}(x) = e \sum_{V} \frac{m_{v}^{2}}{2 \gamma_{v}} \, j_{\mu}^{V}(x) $$

was considered, where based on their quanta numbers, the vector mesons ρ^{o}, ω, φ were being considered. The strong interactions

of the photons, according to this model, proceed via intermediate vector meson states. Thus, the pion photo production according to Fig. 26 could be reduced to the reaction $V + p \rightarrow \pi^+ + n$.
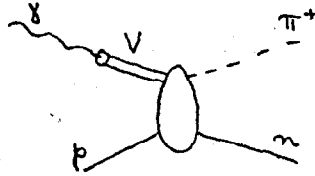

Fig. 26: Vector meson predominance model of the pion photo production.

In order to connect the two processes, it is assumed that the matrix element is only a slightly variant function of the 4-pulse square of the incoming particle and for $k^2 = 0$ (virtual vector meson) it has approximately the same value as for $k^2 = m_v^2$ (real vector meson).

The ρ^o meson is to supply the main component since according to SU(6) the following relationship applies [42]

$$\frac{1}{\gamma_\rho^2} : \frac{1}{\gamma_\omega^2} : \frac{1}{\gamma_\varphi^2} = 9 : 1 : 2$$

Using the inverse time independence and isospin conservation, a relationship can be established [43] to the experimental observed process

$$\pi^- + p \rightarrow \rho^o + n$$

The photo production effective cross section can then be expressed as follows [42]

$$\frac{d\sigma}{dt}(\gamma p \rightarrow \pi^+ n) = \frac{1}{2}(1 - X_{oo}) \cdot \frac{p_\pi^*}{p_\rho^*} \cdot \frac{\alpha \cdot \pi}{\gamma_\rho^2} \cdot \frac{d\sigma}{dt}(\pi^- p \rightarrow \rho^o n) \qquad (7)$$

X_{oo} is the density matrix element of ρ^o between the states whose helicity is 0. This component must be subtracted since only transversally polarized vector mesons can be coupled to real photons. X_{oo} has the approximate value of 1/2 [43]. The coupling constant results from the ρ predominance model of the pion form factor and of the experimentally known decay width of the ρ meson as [44,42]

$$\gamma_\rho^2 / 4\pi \approx 0.57$$

Experimental investigations of the ρ^o production at π-p interactions are available for pion momentum values of 1.7 [45], 2.75 [46], 3.0 [47,48,49], 4.0 [50,51] GeV/c.

Table 8 shows a comparison of the total ρ^o production cross section as well as the calculated "theoretical" π^+ photo production effective cross sections in accordance with Eq. (7), with the experimental photo production data. The total effective cross sections for the π^+ photo production were obtained by integrating the approximation formula

$$\frac{d\sigma}{dt} = Ae^{Bt}$$

since the t range covered during the measurements is relatively

small, we must expect errors of approximately 20%. Measurements
made by Lewis [52] for k = 2.7 GeV were utilized which cover
up to $|t| = 2(\text{GeV/c})^2$.

Table 8: Comparison of the total effective cross sections
of the π^+ photo production with the data of the
vector predominance model

P_o (GeV/c)	$\sigma^{exp}(\pi^-p\to\rho^0 n)$	$\sigma^{"theor"}(\gamma p\to\pi^+ n)$ $((1-X_{oo})=1/2)$	$\sigma^{exp}(\gamma p\to\pi^+ n)$
1,7	~ 2 mb[45]	~ 2,3 μb	6 μb
2,75	1,1 mb[46]	1,0 μb	2,9 μb
3,0	1,6 mb[48]	1,5 μb	2,8 μb

The order of magnitude of the photo production effective cross
sections is indeed correctly predicted, but a more accurate
test of the vector meson predominance model fails because of the
relatively large uncertainty of the ρ production cross sections
and density matrix elements. Only about 10% of the ρ component
is to be expected from the ω meson and from the φ meson even
less since the φ production in πN interactions is substantially
lower.

In Reference 45, the differential effective cross section
$\frac{d\sigma}{dt}$ (π^- p → ρ^0n) is shown. If the t dependence of the photo
production cross section is to be compared with it, it is neces-
sary to know the density matrix element X_{oo} as a function of t.
Reference 45 does not indicate the density matrix elements.

However, in order to have at least an estimate, values for it
will be used from the ρ production data at 4 GeV/c, which yielded
$X_{oo} \approx 0.7$ at $\theta^* + \dot{0}^o$ and $X_{oo} \approx 0.5$ at $\theta^* = 60^o$ (cf [43]). Fig.
27 shows the effective cross sections of ρ^o production for 1.7
GeV/c and a "theoretical" variation estimated therefrom for
the photo production in comparison with the experimental data
$\frac{d\sigma}{dt}$ ($\gamma p \to \pi^+ n$). Indeed, a discrepancy of a factor of 2 occurs
with respect to the magnitude, however, in both cases we en-
counter a somewhat exponential t dependence with increases that
do not differ too much from each other. In view of the relatively
large uncertainties, the similarities should not be overestimated.
The ρ production cross sections again increase considerably for
$|t|$ between 1 and 2 $(GeV/c)^2$. It would be interesting to have
available the photo production data in order to test the validity
of the ρ predominance model at large momentum transfers. The
ρ production at 3 and 4 GeV/c does not show a similar resumption
of the increase of the effective cross section as a function of
$|t|$, but at 3 GeV/c [49] a very weak increase toward backward
angles is observed while the 4 GeV/c data [50] continued decreas-
ing up to $|t| = 3.5$ $(GeV/c)^2$. For the 4 GeV/c values [50] we
obtain in the range $|t| \leq 0.5$ $(GeV/c)^2$ a very steep exponential
decay with a slope $B \approx 8.5$ $(GeV/c)^{-2}$, as compared with a value
of $B \approx 2.6$ $(GeV/c)^{-2}$ for the photo production at the maximum
energy of 2.9 GeV investigated in this experiment. Since the
energy dependence of the rise in photo production is not very
pronounced (cf Table 7), it appears somewhat doubtful whether

at 4 GeV/c the vector predominance model is able to describe the
t dependence of the π^+ photo production for $|t| \leq 0.5$ correctly.
For larger values of $|t|$ the ρ production cross sections de-
crease considerably slower so that here a coincidence is more
likely.

V. Summary

An investigation of one-pion photo production of positively
charged π mesons in the γ energy range from 1.2 to 3 GeV and
in the pion laboratory range from 8° to 20° is made. The
differential effective cross sections $\frac{d\sigma}{d\Omega}*$ and $\frac{d\sigma}{dt}$ are deter-
mined as a function of their variables k, θ^* and s $\left(=M_p^2 + 2M_p k\right)$,
t. It is shown that at fixed center-of-mass angles, the effec-
tive cross sections appear as a function of the γ energy
resonance structure in the range of nucleon isobars $N^*_{3/2}$ (1924),
$N^*_{1/2}$ (2190). The effective cross sections $\frac{d\sigma}{dt}$ decrease above
1.7 GeV approximately exponentially in proportion with the
4-pulse transfer. A comparison with theoretical models yields
the following results:

The unmodified peripheral model (calibration indepedent expan-
sion of the one-pion exchange) yields a fully erroneous t de-
pendence;

The absorption model predicts the correct order of magnitude of
the effective cross section, but too little decay as a function
of increasing $|t|$.

The Regge pole model indeed is able to describe the t dependence under certain assumptions for larger values of $|t|$, but an energy dependence which is not in consonance with the experiemtn results if a Regge trajectory variation is assumed such as that known from charge exchange scattering.

The vector meson predominance model establishes a relationship to the ρ production in πN interactions. The predictions regarding the total effective cross sections are fulfilled except for a factor of 2. At 1.7 GeV/c the predicted t dependence agrees approximately with the experiment.

VI.   Appendix

VI.1)   Dynamic for the π^+ Photo Production

For the 4-vectors P_1 to P_4, of the particles participating in the reaction

$$\gamma + p \rightarrow \pi^+ + n \tag{A1}$$

the following applies

$$P_1 + P_2 = P_3 + P_4 \tag{A2}$$

We use the metric relationship $p^2 = E^2 - \vec{p}^2 = m^2$; values without asterisks relate to the laboratory system while those with the asterisks relate to the center-of-mass system. The square of the total energy in the center-of-mass system and in the 4-vector momentum transfer is designated with s and t respectively

$$S = (p_1 + p_2)^2 = (E_1^* + E_2^*)^2 = E^{*2} = M_p^2 + 2kM_p$$

$$t = (p_1 - p_3)^2 = m_\pi^2 - 2k^* E_\pi^* + 2k^* p_\pi^* \cos \Theta_\pi^* \tag{A3}$$

where k = the energy of the γ quantum and Θ^* the production angle of the pion. The total energy as well as the energy of the photon and the pion in the center-of-mass system is calculated as follows:

$$E^* = \sqrt{S} = \sqrt{M_p^2 + 2kM_p}$$

$$E_\pi^* = \frac{E^{*2} + m_\pi^2 - M_n^2}{2E^*} \tag{A4}$$

$$k^* = \frac{M_p}{E^*} \cdot k$$

The connection between the momentum and the production angle of the pion and the γ energy is obtained from

$$p_4^2 = (p_1 + p_2 - p_3)^2$$

$$M_n^2 = 0 + M_p^2 + m_\pi^2 + 2kM_p - 2kE_\pi - 2M_p E_\pi + 2k p_\pi \cos \Theta_\pi \tag{A5}$$

$$\text{at} \quad k = \frac{M_n^2 - M_p^2 - m_\pi^2 + 2M_p E_\pi}{2(M_p + p_\pi \cos \Theta_\pi - E_\pi)}$$

(in the laboratory system).

For an assumed p_π and Θ_π value the γ energy k is clearly defined in process (A1), a fact which essentially is in agreement with the interpretation of the experiment. If we resolve Eq. (A5) for $\cos \Theta_\pi$, we obtain the function $\Theta_\pi(p_\pi)\big|_{k = \text{const}}$ shown in Fig. 1:
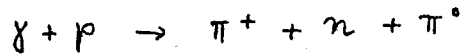
$$\cos \theta_\pi = \frac{M_n^2 - M_p^2 - m_\pi^2 + 2 M_p E_\pi - 2k M_p + 2k E_\pi}{2k p_\pi} \qquad (A6)$$

This equation accordingly applies to every other photo production reaction with two particles in the terminal state; for example, to describe the process

$$\gamma + p \rightarrow K^+ + \Lambda^\circ$$
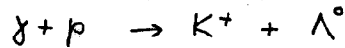
in Eq. (A6) we must only substitute m_π with m_k and M_n with M_Λ.

The energy distance between the one-pion production (A1) and multiple production, such as

$$\gamma + p \rightarrow \pi^+ + n + \pi^\circ$$

can therefore be calculated: The system $(n + \pi^0)$ is considered as a particl x whose effective mass is

$$M_x = \sqrt{(p_n + p_{\pi^\circ})^2}$$

We obtain from Eq. (A5) the γ energy required to produce a π^+-meson with momentum p_π and angle θ_π and a particle x if we substitute M_n with M_x. Evidently

$$\Delta k = k^{multiple} - k^{simple} = k(M_x^2) - k(M_n^2)$$

which is minimum $(= \Delta k_{threshold})$, when M_x assumes its smallest value

$$M_x = M_x^{min} = M_n + m_{\pi^0} \quad .$$

For this case we calculate $\Delta k_{threshold} \approx 150$ MeV. If we substitute in Eq. (A6) M_n with $M_n = m_{\pi^0}$, we obtain the curve designated in Fig. 1 with $(n + \pi^0)$ as the energy threshold of the multiple production.

The relationship between the production angle Θ_π^* in the center-of-mass and Θ_π in the laboratory system can be obtained by calculating the invariance $p_1 p_3$ in both systems:

$$p_1 p_3 = k E_\pi - k p_\pi \cos \Theta_\pi = k^* E_\pi^* - k^* p_\pi^* \cos \Theta_\pi^* \tag{A7}$$

The values k, Θ_π, p_π, E_π are known for assumed reference angles Θ_0 and reference momentum p_0 of the spectrometer for each hodoscope counter combination $(\Theta_i p_j)$ (cf II.4.2); from Eq. (A4) we can calculate k^*, E_π^*, p_π^* so that Eq. (A7) becomes a determinant equation for $\cos \Theta_\pi^*$.

From Eq. (A5) we obtain by differentiation

$$\left(\frac{\partial k}{\partial p_\pi} \right)_{\Theta_\pi = const} = \frac{(k + M_p) p_\pi - k E_\pi \cos \Theta_\pi}{E_\pi (M_p + p_\pi \cos \Theta_\pi - E_\pi)} \tag{A8}$$

The space angle conversion is obtained as follows [53]: Starting with the Lorentz conversion from the laboratory to the center-of-mass system

$$p_\pi^* \cos \Theta_\pi^* = \bar{\gamma} (p_\pi \cos \Theta_\pi - \bar{\beta} E_\pi)$$

$$E_\pi^* = \bar{\gamma} (E_\pi - \bar{\beta} p_\pi \cos \Theta_\pi)$$

$$\left(\bar{\gamma} = \frac{k + M_p}{E^*} \quad , \quad \bar{\beta} = \frac{k}{k + M_p} \right.$$
(Lorentz factor and velocity of the center-of-mass system)

we obtain by differentiation with respect to $\cos \Theta_\pi$ (p_π^*, E_π^* are independent of $\cos \Theta_\pi$; furthermore, $dE_\pi/dp_\pi = p_\pi/E_\pi$):

$$\bar{\gamma} \left(p_\pi + \cos\Theta_\pi \frac{dp_\pi}{d\cos\Theta_\pi} - \bar{\beta} \cdot \frac{p_\pi}{E_\pi} \cdot \frac{dp_\pi}{d\cos\Theta_\pi} \right) = p_\pi^* \cdot \frac{d\cos\Theta_\pi^*}{d\cos\Theta_\pi}$$

$$\bar{\gamma} \left(\frac{p_\pi}{E_\pi} \cdot \frac{dp_\pi}{d\cos\Theta_\pi} - \bar{\beta} p_\pi - \bar{\beta}\cos\Theta_\pi \frac{dp_\pi}{d\cos\Theta_\pi} \right) = 0$$

If $dp_\pi/d\cos\Theta_\pi$ is eliminated it follows that

$$\frac{d\Omega_\pi^*}{d\Omega_\pi} = \frac{d\cos\Theta_\pi^*}{d\cos\Theta_\pi} = \frac{p_\pi^2}{\bar{\gamma} p_\pi^* (p_\pi - \bar{\beta} E_\pi \cos\Theta_\pi)} \qquad (A9)$$

VI.2) Reliability of the Main Coincidence Data

2.1) Counter Efficiency

The probability that a particle passes through all four scintillation counters S1 through S4 and furnishes a main coincidense pulse is given by the product of the counter efficiency of the four counters multiplied by the probability that their output pulses overlap in the main coincidence. If the amplification of the photo multiplers is made sufficiently great, the counter efficiency of the scintillation counter can be easily raised to 99.9%. Prior to every major measurement phase, control tests were conducted on this subject. The resolution of the coincidences was so dimensioned that in the delay curve, a plateau of about 3 ms was present. In this manner, approximately 100% reliability for time overlap was provided.

2.2) Dead Time

Counter 1, which presents the highest single count rate, is provided with a limitor for pulse shaping as mentioned earlier in

which no dead time losses occur. The instantaneous count rates
in the other counters are always clearly below several hundreds
of kc. For a descriminator dead time of 10 ns and an average
distance between pulses of several μs, an erroneous result due
to dead time effects of a maximum of several promills is to
be expected. In the subsequent high speed electronics, dead
time is of no consequence at all since the coincidence rates
are lower by several orders of magnitude. However, there exists
a dead time of another kind which is caused by the PDP-5 data
processing unit: If an event has been accepted, the high speed
electronics will remain closed for about 60 μs and is no longer
able to record the events which occur during this time. The
shortening of the measurement time thus produced is corrected
by a monitor telescope (section II.2.5). However, in all mea-
surements, the event rate was so low that at the most one par-
ticle per γ-ray pulse of 1 ms duration occurred. Therefore, the
monitor correction (2 0/00) which is small anyway, cannot be
attributed to PDP-5 dead time effects but to the fact that part
of the γ-ray intensity lies outside the energy limits selected
(II.2.5).

2.3) Random Coincidences

From the measured main coincidence rate $C3 = (1234)$ those amounts
must be subtracted which do not correspond to the passage of a
particle through the entire system. The delayed coincidenes
$C4 = (1_v 234)$ and $C5 = (1234_v)$ where v represents a delay of the
particular counter by 50 ns, yield an indication of the frequency

of these "simulated" events, but not their number without further ado. Fig. 18 shows that only 1 to 3 o/oO of the C3 quota reaches C5 as a function of the laboratory angle while C4 lies in the range of 12 to 20% for 5o/oO. In contrast, it increases rapidly for small angles: to 3% at 10° and 5% at 8°. This is connected with the fact that the electromagnetic background at the angle focus for small angles is very important.

Let us consider the case where C4 = $(1_v 234)$ furnishes an output pulse. Since Counter 1 enters this coincidencs with a 50 ns delay, at least two particles are required: one which causes a count in (234) and another which passes through S1 50 ns earlier (the background of the counters is fully negligible compared to the individual count rates produced by the particles as a result of beam operation.). Using instantaneous single count rates of less than 100 kc in S2 through S4, as well as the measured quotas of C1 = (23), C2 = $(2_v 3)$, it can be estimated that more than 99% of the pulses furnished by (234) can be attributed to particles which pass through all three counters. A Monte-Carlo calculation now shows that 95% of all particles passing through the spectrometer and (234) also hit S1. In the majority of cases, if C4 produces a count, a "true" particle passed through the entire setup and in addition, 50 ns earlier a "background particle" passed through S1. Accordingly, only approximately 5% of the quota of C4 = $(1_v 234)$ may be deducted from the main coincidence quota C3 = (1234) in order to correct for random coincidences of

this type. Even for the smallest angle of 8°, this is a neg-

ligible effect of 0.05 x 5%.

If the counter is delayed, this does not cover all possibilities

of creating random coincidences. The low quota in C5 = (1234_v)

however, shows that no difficulties should be expected from the

remaining counters since even at (1234_v) a large part of the

pulses present should be attributed to true particles. Altogether,

a pessimistic estimate of the number of the events simulated by

random coincidences is 1% of the measured quota. Compared to

other systematic errors this is negligible.

VI.3) Unclear Events in the Hodoscopes

In all cases where either no counter or more than one counter

responded   in the hodoscope, the respective event can no

longer be clearly analyzed.

3. 1) Multiple Events in the Angle Hodoscope

The number of multiple events in the angle hodoscope increases

considerably as does the quota of C4 = (1_v234) (Fig. 28). For

large angles, in contrast, the multiple quota remains constant

at about 3% of the main coincidence quota while the quota (1_v234)

becomes very small. Therefore, two difference causes for the

multiple events in the angle hodoscope must exist. In general

it can be said in almost all cases, in the presence of a multiple

event in the hodoscope, a true particle also passed through the

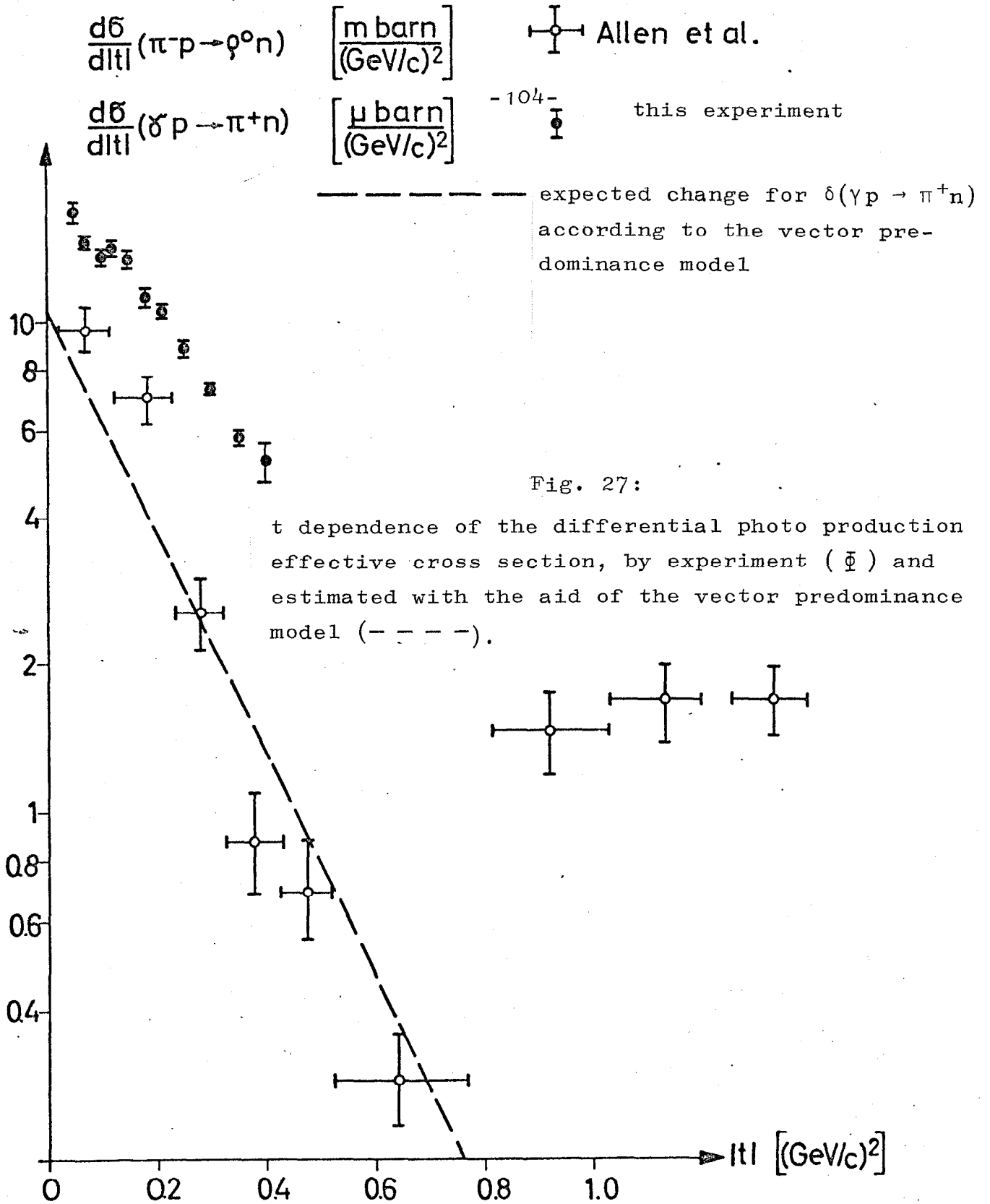system. There are two arguments for this: For one, we saw in

$$\frac{d\bar{6}}{d|t|}(\pi^- p \to \varrho^0 n) \quad \left[\frac{m\,barn}{(GeV/c)^2}\right]$$

$$\frac{d\bar{6}}{d|t|}(\gamma p \to \pi^+ n) \quad \left[\frac{\mu\,barn}{(GeV/c)^2}\right]$$

⊖ Allen et al.

-104-   this experiment

— — — expected change for $\delta(\gamma p \to \pi^+ n)$ according to the vector pre-dominance model

Fig. 27:

t dependence of the differential photo production effective cross section, by experiment (⊕) and estimated with the aid of the vector predominance model (− − − −).
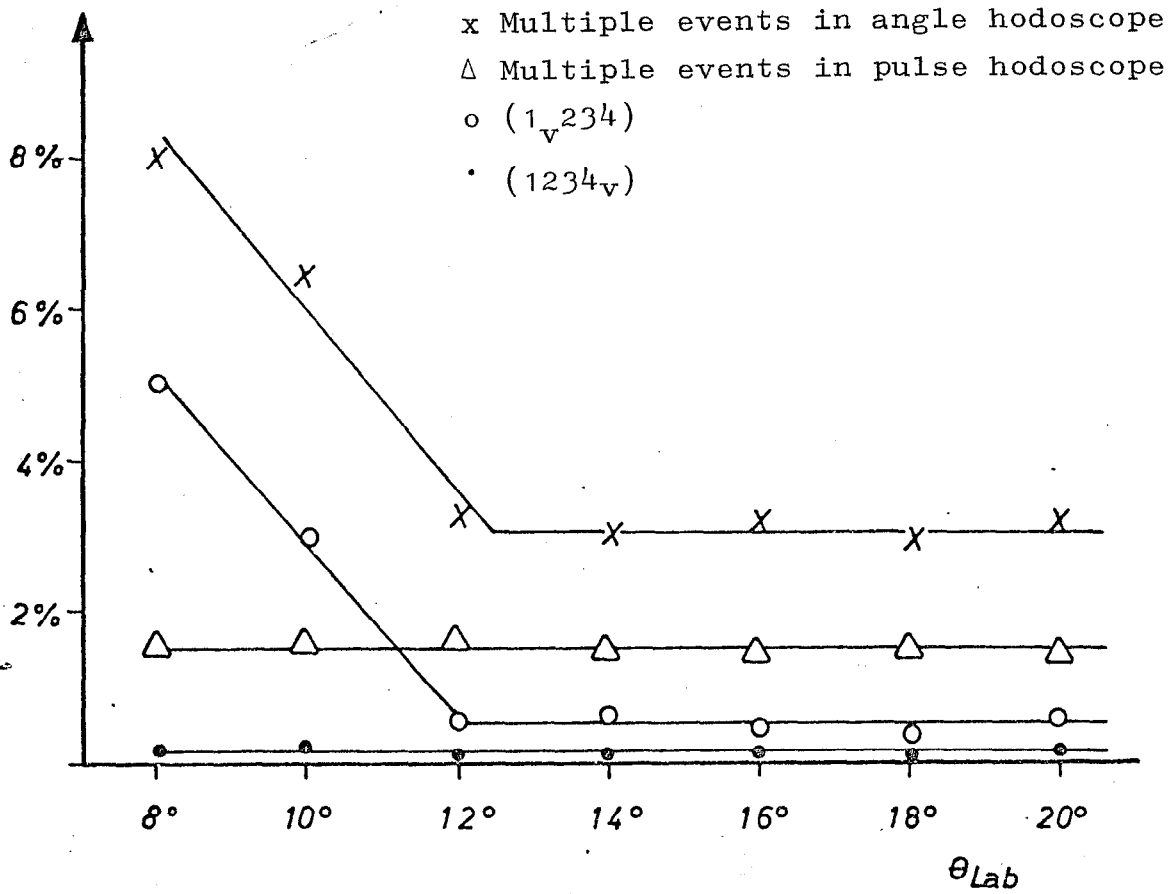
Fig. 28: Contribution of multiple events and delayed
coincidences to the main coincidence quota
as a function of the spectrometer angle. The
values are averaged over all energy values.

in section 2.3) that a main coincidence pulse indicates a "real"
particle with a probability of greater than 99%, secondly, the
frequency distribution of the multiple events, being a function
of the hodoscope counter number, follows quite accurately the
acceptance curve of the hodoscope for "real" particles (Fig. 29).[*]
The preference for the middle hodoscope counters comes about by
the fact that the quadrupoles located behind the directional
focus limit the space angle for the passage of real particles
through the lateral hodoscope counters.

a) Multiple events for large angles

There are many possibilities of getting more than one hodoscope
counter to count by the passage of a single particle, perhaps
a pion. The assumption of insufficient light density between
two counters can be ruled out since otherwise certain pairs
would always be preferred in the distribution of the multiple
events. There remain the possibilities that the pion produces
a δ electron in the material located ahead of the hodoscope or
in the scintillator material itself, which is counted in coin-
cidence with the particle in the hodoscope. Since the half-width
of the counters is only 5 mm, δ electrons of only a few MeV are
sufficient in the latter case to produce multiple events, where-
by adjacent hodoscope counters are given great preference. Fig.
30a shows a frequency distribution of multiple events as a
function of the distance between the respective hodoscope counters

---

[*]This is obtained in such a way that for example for a double e-
event, half an event is attributed to the respective counter.

for a laboratory angle of 20°. About 80% of all multiple events

actually occur between adjacent hodoscope counters which points

to the accuracy of this hypothesis. On analyzing these adjacent

events, the angle definition for the particular event is indeed

lower by a factor of 2 than usual; however, since during the

calculation of the effective cross section over a larger angle

range is averaged out anyway, this is of no importance. In the

evaluation, the adjacent events are therefore treated as "good"

particles and distributed half and half among the two counters.

The remaining multiple events for which the angle determination

is not always possible, rarely amount to more than 0.5% in the

main coincidence rate. Therefore, we only obtain a small error

if we multiple the effective cross section calculated from the

"good" particles with a correction factor for the non-adjacent

multiple events.

b) Multiple events for small angles

Fig. 28 already showed that in the angle range from 20° to 12°

the ratio of multiple events is approximately constant at 3%

and for an angle range of 10° and 8° in parallel with the quota

in (1_v234) it increases to 6 and 8% respectively. Fig. 31 now

shows that in addition, the ratio of the non-adjacent multiple

events increases from 20% to 50% and 60% of the total multiple

rate which also results from the frequency distribution as a

function of the counter distance (Fig. 30b). In addition to

the multiple events which always stem from a single particle and

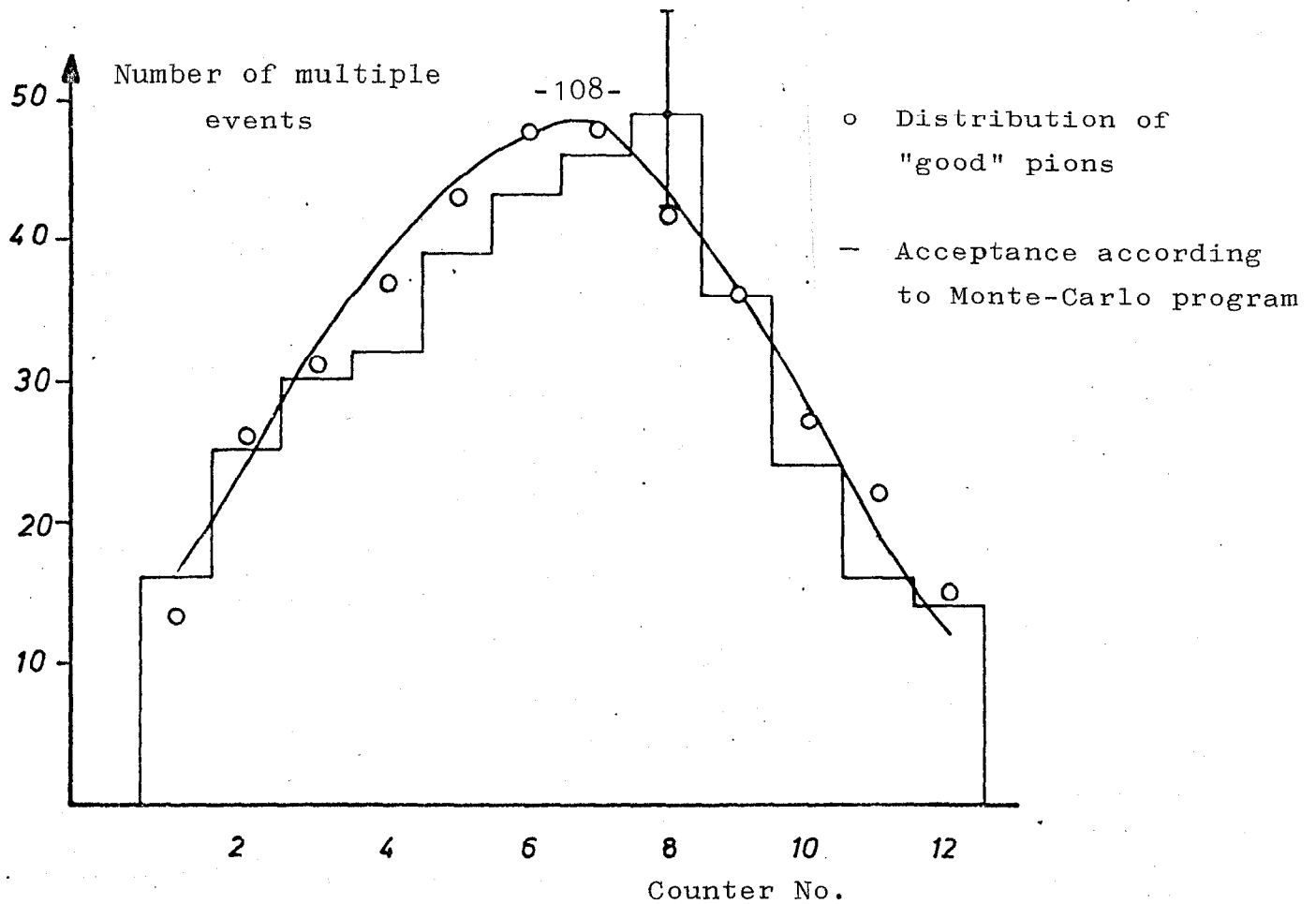which amount to 3% of the main coincidence quota, other events

Fig. 29: Frequency distribution of multiple events in the angle hodoscope. Solid curve: acceptance variation according to Monte-Carlo program.
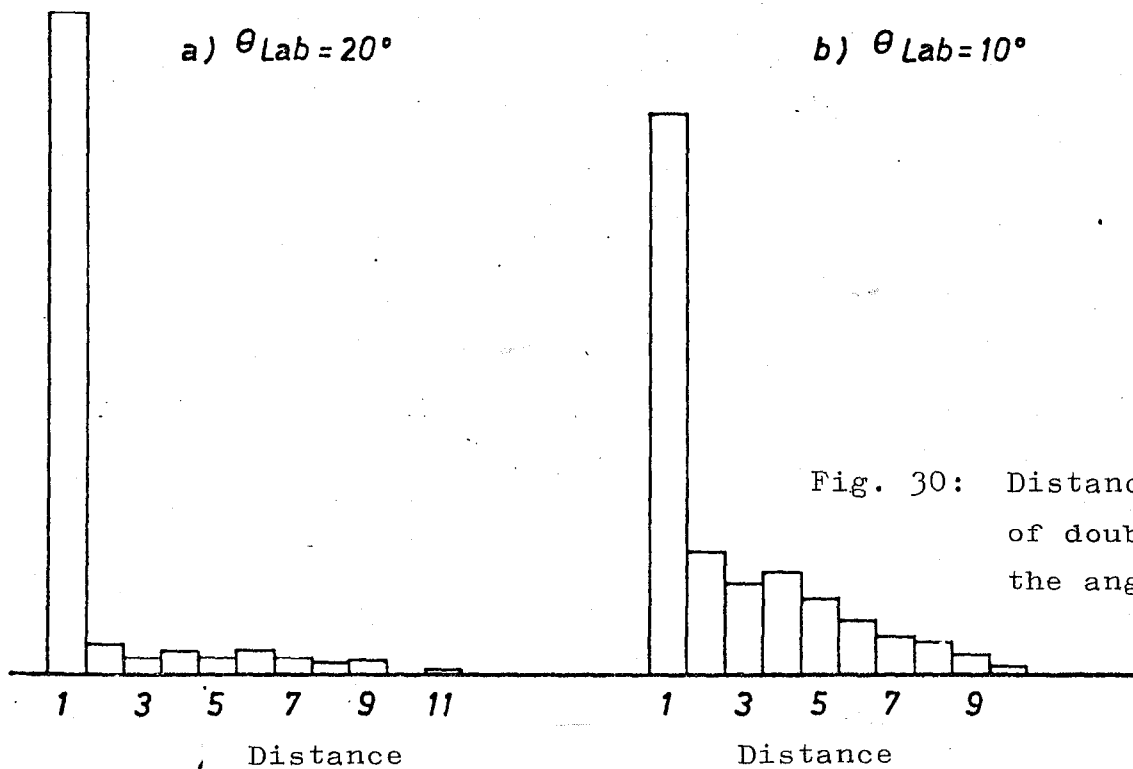

Fig. 30: Distance distribution of double events in the angle hodoscope.

must be added which are created by the fact that during the re-
solving time of a true particle and a background particle pass
through the hodoscope. Since the background is unrelated to the
true particles, there is no reason to assume a preference for
adjacent counters. The distribution of the pions over the hod-
oscope follows the curve calculated by the Monte-Carlo acceptance
program. The probability for a distance d between pion and back-
ground particle can be calculated by folding the acceptance dis-
tribution $F(x)$ and the distribution of the background $G(x)$ where
it should be assumed that the background is distributed evenly.

$$W(d) = const . \int_{-B/2}^{+B/2} F(x) \, G(x+d) \, dx = const' . \int_{-B/2}^{B/2-d} F(x) \, dx$$

$(B = $ width of the hodoscope$)$

The probability distribution for the distance is thus simply
given by the integral over the acceptance curve with a variable
upper limit. The solid curve in Fig. 32 is the result of this
integration.

If we subtract from the distance distribution of the multiple
events the ratio which cannot be attributed to the background
and which was measured at large angles, we obtain the points also
recorded in Fig.32. Due to the subtraction, the errors are sub-
stantial, however, it is shown that the above interpretation pro-
vides a fairly good description.

At 8°, the rate of multiple events is so high that due to the
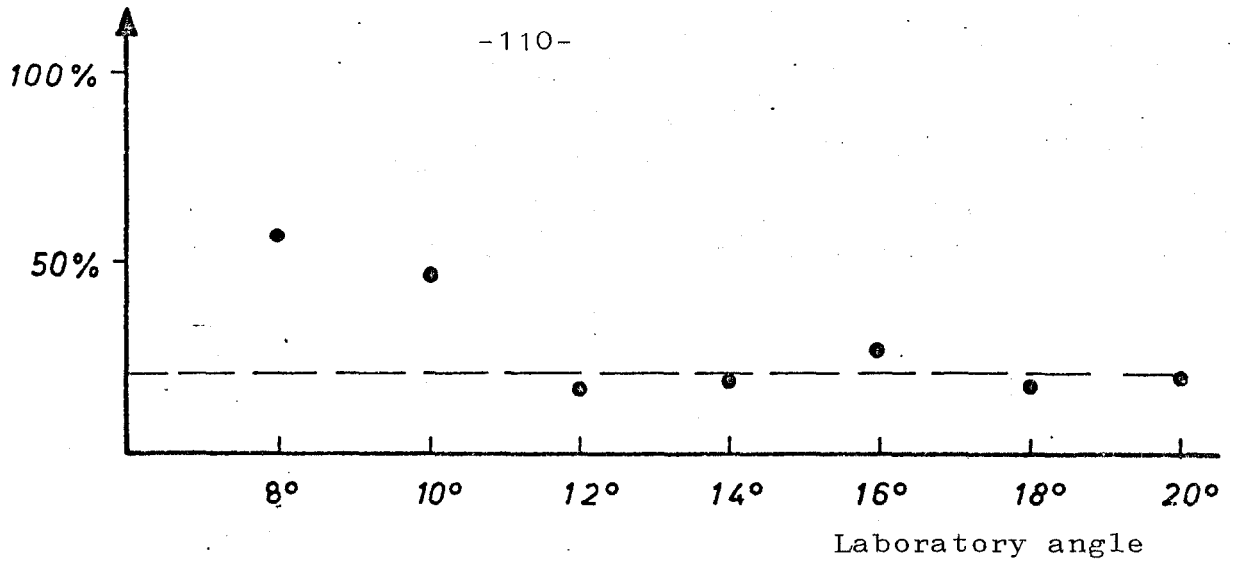uncertainty in the angle determination and the flight time

Fig. 31: Relative ratio of non-adjacent multiple events in the angle hodoscope as a function of the spectrometer angle.
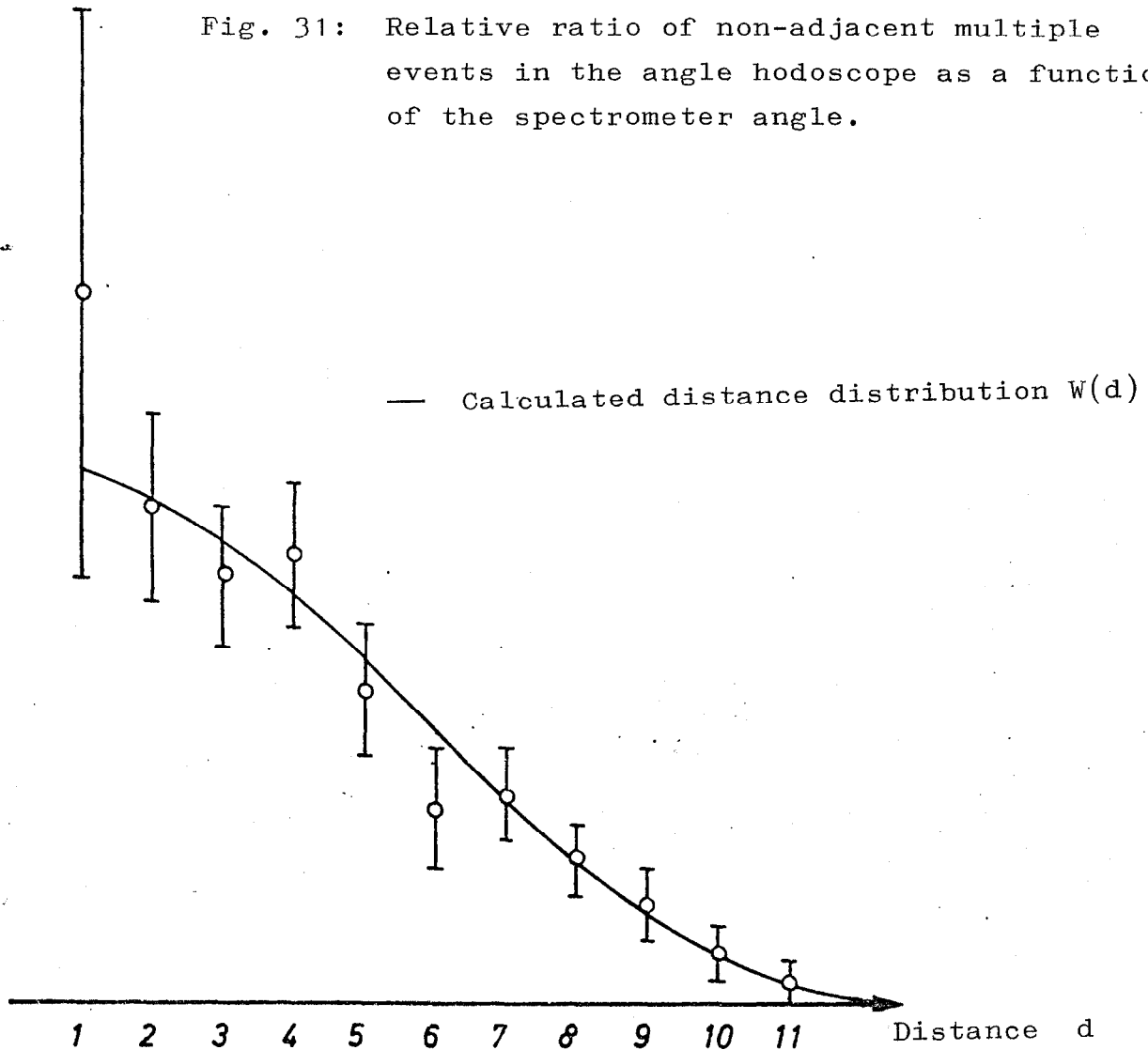

Fig. 32: Distance distribution for multiple events which stem from a coincidence between a true and a background particle.

correction (II.6.2.2) a systematic error of 2% is to be expected.

3.2) Non-Count of the Angle Hodoscope

The gaps between the hodoscope counters are about 1% of the counter width. Therefore, in approximately 1% of all cases a non-response of the angle hodoscope may be expected. This experimentally satisfied almost independent of energy and angle. The effective cross sections were provided with the corresponding correction factor.

3.3) Unclear Events in the Pulse Hodoscope

Multiple Events

The ratio of multiple events in the pulse hodoscope practically amounts to 1.5% regardless of angle and energy. About 60% of these pertain to adjacent counters. Due to the greater width of 2 cm of the pulse counters the probability in the angle hodoscope is relatively smaller that δ electrons bumped in a counter reach an adjacent counter. In contrast, upstream along the beam, there is a greater probability for the formation of δ electrons. Multiple events as a result of background are said to be negligible.

Non-Response

The ratio of gaps to the overall area is approximately 1.3% in the pulse hodoscope. However, in 3% of all cases no signal emanates from the hodoscope. This effect could not be explained and must therefore be included in the system errors. The effective cross sections were corrected similar as in section 3.2.

VI.4)   Quality of Separation of Pions and Protons using Flight

Time Measurement

4.1)   Pion-Proton Separation in the Flight Time Spectrum

In the effective cross section calculation, a particle is clas-

sified as a pion or a proton depending on the flight time chan-

nel above and below a given threshold. For higher pulses, the

overshoots of the pion and proton maxima in the flight time

spectrum and the selection of this threshold contains a certain

arbitrariness. Greater accuracy is obtained if the maxima are

matched by way of Gauss functions and if the threshold is so

selected that the count rate above this threshold corresponds

the the area of the "pion Gauss curve."

4.2)   Matching of the Flight Time Spectrum of a Particle

Category by a Gauss Function

As explained in section II.6.2 a number of independent effects

contribute to the broadening of the flight time distribution.

Due to the statistical nature of the individual effects and their

independence from each other the resulting distribution can be

described with close approximation by a Gauss function (Fig. 33a).

Using a MINIMIZER program [54], a Gauss function was matched to

the experimental distribution. This program determins the "opti-

mum" value for the parameter a_i of the Gauss function (average

value, σ, amplitude), by minimizing χ^2 by a stepwise approxi-

mation, i.e. the likelihood function L is maximized. In addition,

the error matrix

$$\overline{(a_i - \overline{a_i})\ (a_j - \overline{a_j})} = (H^{-1})_{ij} \tag{23}$$

is calculated where $H_{kl} = \dfrac{\delta^2 w}{\delta a_k \delta a_c}$ represents the matrix of the

second derivatives of $w = \log L$. χ^2 is defined here as

$$\chi^2 = \sum_i \frac{(n_i - g(x_i))^2}{(\sqrt{n_i})^2}$$

where x, is the flight time channel involved, $g(x_i)$ the value

of the Gauss function at this point, n_i the measured count rate

in the channel x_i and $\sqrt{n_i}$ their errors. For almost all flight

time spectra investigated we obtained values ranging from 0.5

to 1 for χ^2/N_F (N_F = number of degrees of freedom) whereby the

assumption of a Gaussian distribution of the flight time maxi-

mum is justified.

The area F of the Gauss function so matched in general is some-

what different from the total number of events in the distri-

bution since for a count rate $N = \sum_i n_i$ F should lie only in

2/3 of all cases within the limits $N \pm \sqrt{N}$. Although this was

satisfied, it turned out that the area in all cases investigated

was 2 to 3% smaller than the measured rate (at $N \approx 1000$). This

points to a certain deviation of the distribution from a Gaussian

distribution, be that due to the wider lateral overshoots of to

assymetries in the spectrum. The area error is almost equal to

the statistical error of the particle number. The area under

the Gaussian curve

$$g(x) = a_3 \exp\left(-(x-a_1)^2/(2a_2^2)\right)$$

as a result of normalization,

$$\frac{1}{\sqrt{2\pi}\,\sigma} \int_{-\infty}^{\infty} e^{-x^2/2\sigma^2} \, dx = 1$$

is given by

$$F = \sqrt{2\pi}\, a_2 a_3$$

In accordance with the law of the error propagation, the variance of F

$$(\Delta F)^2 = \sum_{i,j=2,3} \frac{\partial^2 F}{\partial a_i \, \partial a_j} \left(H^{-1}\right)_{ij}$$

$$= 2\pi \left(a_3^2 \, \Delta a_2^2 + a_2^2 \, \Delta a_3^2 + 2 a_2 a_3 \, \overline{(a_2 - \overline{a_2})}\,\overline{(a_3 - \overline{a_3})}\right)$$

$(\Delta F)^2$ is of the same order of magnitude as the particle number N. For the example shown in Fig. 33a, the following applies:

$$N = 1025, \quad F = 1001, \quad (\Delta F)^2 = 1032$$

If we disregard the small systematic difference between the area and particle number, and if we assume a Gaussian distribution, F is a measure of the particle number N and ΔF of the error of the particle number.

4.3)   Matching of the Flight Time Spectrum of Pions and Protons
         by a Sum of Two Gaussian Functions

As in 4.2), a MINIMIZER is used in order to match the measured
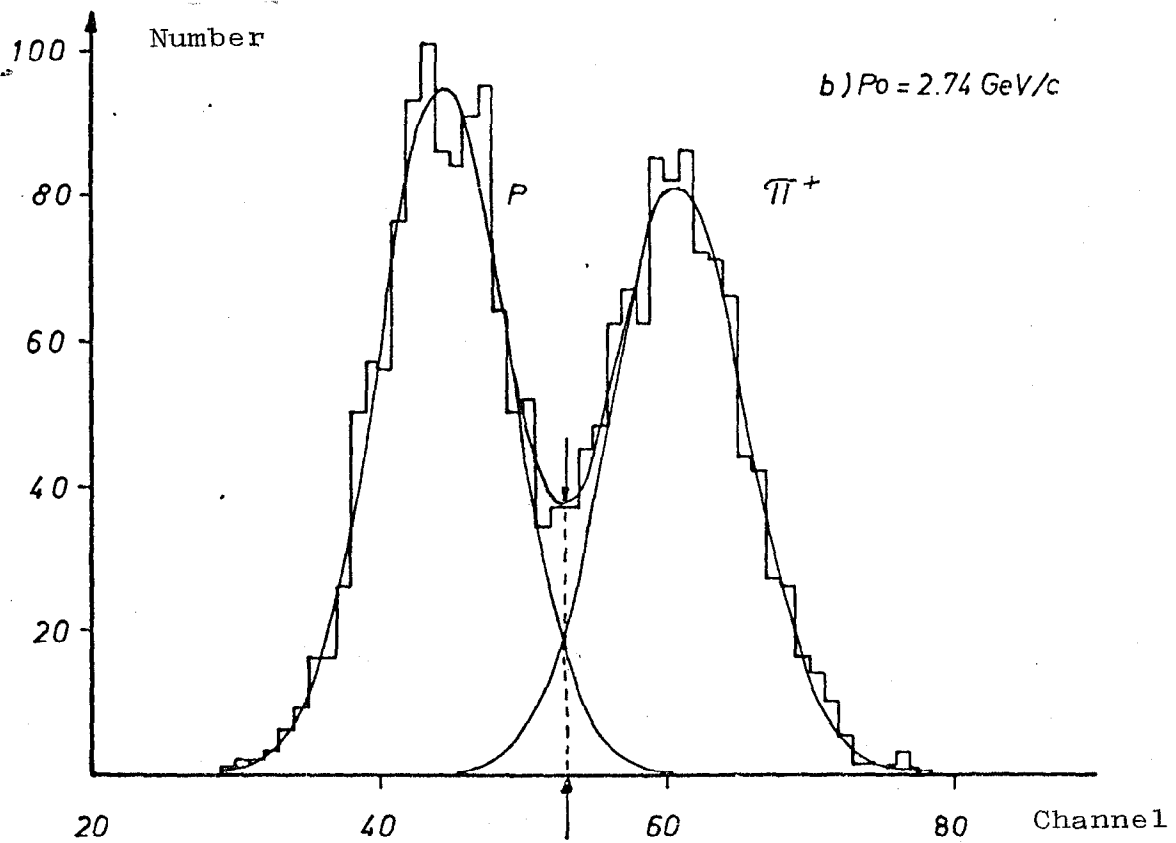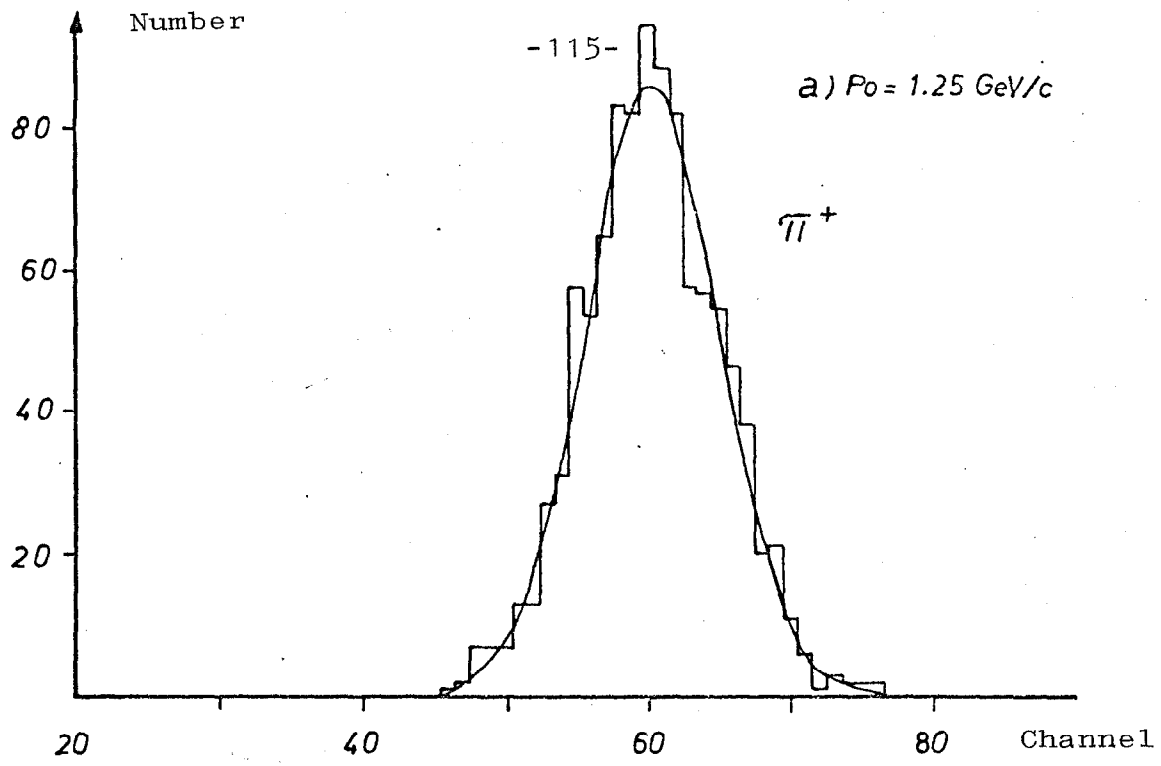
Fig. 33: Matching of flight time spectra by Gauss functions. In the upper spectrum only pions occur while protons of 1.25 GeV/c no longer satisfy the coincidence condition.

distribution with two maxima by the function

$$g(x) = g_1(x) + g_2(x) = a_3 \exp\left(-(x-a_1)^2/(2a_2^2)\right) + a_6 \exp\left(-(x-a_4)^2/(2a_5^2)\right)$$

where again the "optimum" values for all 6 parameters a_i were determined.   Fig. 33b shows for one of the highest pulses of 2.74 GeV/c which occur in the experiment, the result of the matching for which $\chi^2/N_F = 0.6$.   The area ratio of the two Gaussian functions yields the optimum statistical value for the pion to proton ratio.   The threshold in the flight time spectrum must therefore be so selected that the following holds true:

(Events with flight time channel $\geq$ threshold):   (Events with flight time channel $<$ threshold) = F_2 : F_1.

This cannot be satisfied exactly since the threshold must have an integral value (one channel in the flight time spectrum) but the pion number can still be corrected accordingly.   The correction amounted to 2% max.   As earlier, we interpret ΔF_2 as the error in the number of pions but now a larger error than in 4.2) is to be expected due to the overlapping of the two Gauss functions.   For the example selected as shown in Fig. 33b we obtain

$$F_1 = 1079 \qquad\qquad F_2 = 975$$
$$N_1 = 1107 \qquad\qquad N_2 = 974$$

for a threshold in Channel 53.

$(\Delta F_2)^2$ has a value of

$$(\Delta F_2)^2 = 1467$$

and is therefore in fact greater than N_2. This means that in
this case the statistical error of the measurement point was
raised from 3.2% to 3.9% due to the uncertainty in the pion-pro-
ton separation. For lower pulses, this effect rapidly decreases.

Fig. 34 shows the correction factor as a function of the pulse
by which the purely statistical error $\sqrt{N}$ of the measurement
pionts must be multiplied in order to take into account the
error which occurs during the pion-protong separation.

4.4) Error Introduced in the Flight Time Measurement by the
     Background Particles

The flight time coincidence for S1 has almost the same resolving
time as the angle hodoscope counter coincidences (10 ns). There-
fore, at 8°, about 5% random coincidences with background par-
ticles are to be expected. If the background particle arrives
later than the real one, it does not affect the flight time
measurement because the flight time coincidence has already
counted the real particle and due to its long dead time (350 ns)
it does not record another input pulse. However, if it arrives
earlier, the earlier output pulse of the coincidence simulates
a longer flight time. In fact, the flight time spectra frequent-
ly present events with longer flight times for small angles
whose ratio is 2 to 3% at 8° and 1 to 1.5% at 10°. Since through
this effect pions can indeed be identified as protons, but not
vice versa, the pion rate determined must be raised. A reason-
able way is to increase the rate by one-half the correction value,

hence 1% at 8° and 0.5% at 10°, and to add to the statistical errors a symetric error of 1% and 0.5% (of the pion ratio).
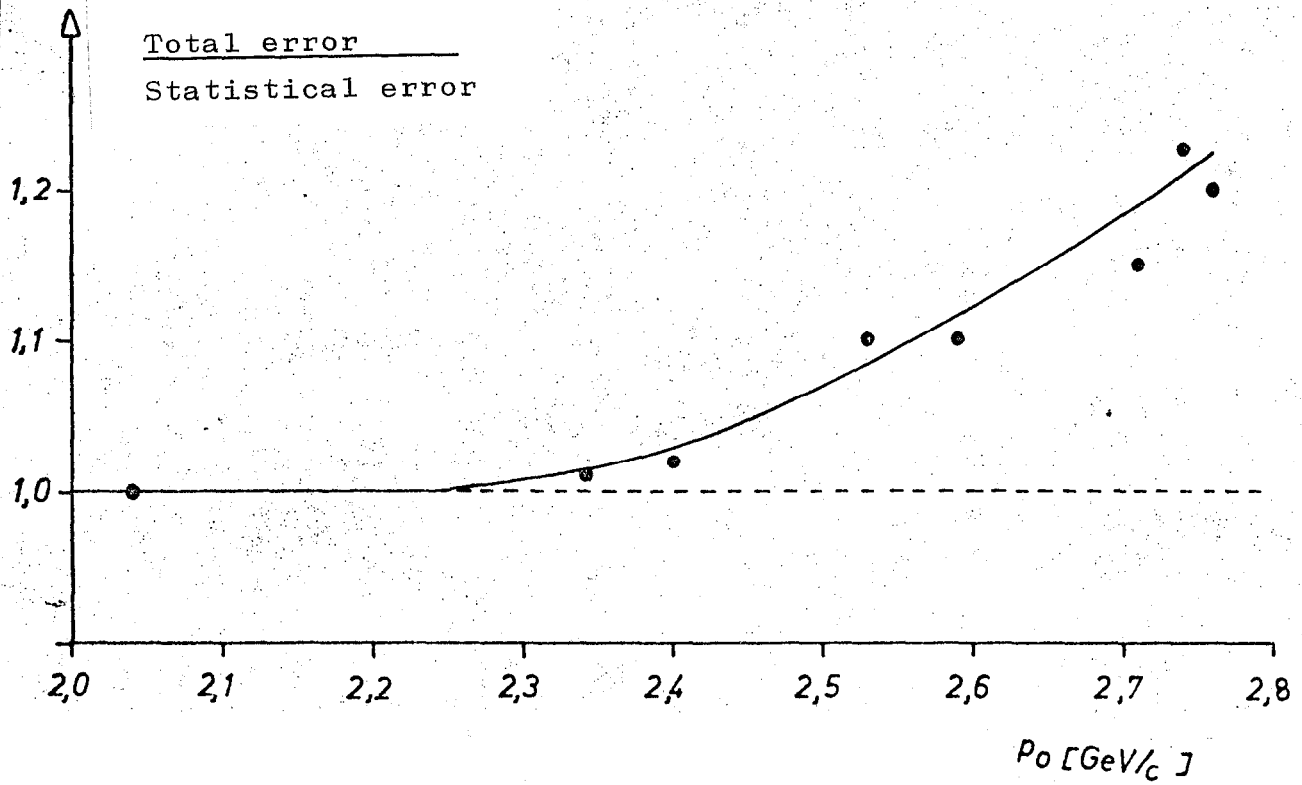

Fig. 34: Increase of the purely statistical error by the uncertainty in the pion-proton separation.

Bibliography

[1] Cf for examples P. Stichel, <u>Photo Production of π-Mesons</u>,
     lecture, Part 1, Fortschr. d. Phys. <u>13</u>, 73 (1965)

[2] G.F. Chew, M.L. Goldberger, F.E.Low, Y. Nambu, Phys. Rev.
     106, 1345 (1957)

[3] F.P. Dixon, Dissertation Caltech 1960 (unpublished)

[4] J.H. Boyden, Dissertation Caltech 1961 (unpublished)

[5] J.R. Kilner, Dissertation Caltech 1963 (unpublished)

[6] S.E. Ecklund, R.L. Walker, Proceeding of the International
     Symposium on Electron and Photon Interactions at High
     Energies, Hamburg 1965, Vol. II, 249

[7] H.A. Thiessen, Dissertation Caltech 1967 (unpublished)

[8] L.S. Osborne, Proceedings of the Internation Symposium on
     Electron and Photon Interactions at High Energies, Hamburg
     1965, Vol. I, 91

[9] V.B. Elings, K.J. Cohen, D.A. Garelick, S. Homma, R.A. Lewis,
     P.D. Luckey, L.S. Osborne, Phys. Rev. Lett. <u>16</u>, 474 (1966)

[10] V.B. Elings, Dissertation MIT 1966 (unpublished0

[11] M.J. Moravcsik, Phys. Rev. <u>104</u>, 1451 (1956)

[12] U. Kotz, Dissertation Hamburg 1967; G. Buschhorn et al.,

publication in preparation

[13] W. Bertram, J. Carroll, R. Eandi, R. Hubner, W. Kern, U. Kotz, P. Schmuser, H.J. Skronn, G. Buschhorn, Phys. Lett. 21, 471 (1966)

[14] DESY Internal Communication S2/F35, 27. 10. 1965

[15] R.R. Wilson, Nucl. Instr. 1, 101 (1957)

[16] A. Ladage, H. Pingel, DESY Report 65/12 (1965)

[17] DESY Internal Report A2/13, Aug. 1966

[18] R. Hubner, Dissertation Hamburg 1967

[19] Valve Handbook: Photo Electronic Components 2, 1965-66

[20] G. Charpak, L. Dick, L. Feuvrais, Nucl. Instr. 15, 323 (1962)

[21] C. Ward, A. Berick, E. Tagliaferri, C. York, Nucl. Instr. 30, 61 (1964)

[22] Made by the Digital Equipment Corporation, Maynard Mass. For the definition of the concepts data break, interrupt, etc,, see PDP-5 Handbook.

[23] cf J. Orear, UCRL Report 8417 (1958)

[24] F. Peters, private communication

[25] High   Energy and Nuclear Physics Data Handbook, Rutherford
      High Energy Laboratory, Chilton (1964)

[26] M.J. Longo, B.J. Moyer, Phys. Rev. 125, 701 (1962)

[27] T. Bowen, M. Di Corato, W.H. Moore, G. Tagliaferri, Nuobo
      Cim. 9, 908 (1958)

[28] M.N. Focacci, G. Giacomelli, CERN Report 66-18 (1966)

[29] G. Buschhorn, J. Carroll, R.D. Eandi, P. Heide, R. Hubner,
      W. Kern, U. Kotz, P. Schmuser, H.J. Skronn, Phys. Rev. Lett.
      17, 1027 (1966)

[30] M. Braunschweig, D. Husmann, K. Lubelsmeyer, D. Schmitz,
      Phys. Lett. 22, 705 (1966)

[31] D.O. Caldwell, J. P. Dowd, K. Heinloth, T.R. Sherwood,
      CEA preliminary printing 1966 and private communication

[32] cf P. Stichel, Photo Production of π-Mesons, Lecture, Part 2,
      DESY Report 66/2 (1966)
      For a comparison of the peripheral model including ab-
      sorption corrections with experiments, see particularly
      article by P. Soding and G. Wolf in this study.

[33] K. Schilling, DESY Report 66/9 (1966)

[34] M. Jacob, G.C. Wick, Annals of Physics 7, 404 (1959)

[35] An application of the absorption model to the π^+ photo pro-

duction may also be found in:

Harun Ar Rashid, M. Kawaguchi, Triest Report IC 66/61 (1966)

Since here only a minimum calibration variant expansion of

the one-pion exchange is used, considerably greater dif-

ferences from the experiment result for small values of $|t|$.

[36]   K. Schilling, private communication

[37]   G. Kramer, P. Stichel, e.g. Physik 178, 519 (1964)

[38]   G. Zweig, Nuovo Cim. 32, 689 (1964)

[39]   A.P. Contogouris, F. Hadjioannou, R. Kinoshita, Nuovo Cim.
       29, 192 (1963)

[40]   M.P. Locher, H. Rollnik, Phys. Lett. 22, 696 (1966)

[41]   G. Hohler, J. Baacke, H. Schlaile, P. Sonderegger, Phys.
       Lett. 20, 79 (1966)

[42]   H. Joos, private communication

[43]   D.S. Beder, Phys. Rev. 149, 1203 (1966)

[44]   M. Gell-Mann, D. Sharp, W.G. Wagner, Phys. Rev. Lett. 8,
       261 (1962)

[45]   D.D. Allen, G.P. Fisher, G. Godden, J.B. Kopelman, L. Marshall,
       R. Sears, Phys. Rev. Lett. 17, 53 (1966)

[46]   Saclay-Orsay-Bari-Bologna Collaboration, Nuovo Cim. 35,
       713 (1965)

[47] W. Selove, V. Hagopian, H. Brody, A. Baker, E. Leboy, Phys. Rev. Lett. $\underline{14}$, 721 (1965)

[48] R.A. Zdanis, L. Madansky, R.W. Kraemer, S. Hertzback, Phys. Rev. Lett. $\underline{14}$, 721 (1965)

[49] V. Hagopian, W. Selove, J. Alitti, J.P. Baton, M. Neveu-Rene, Phys. Rev. $\underline{145}$, 1128 (1966)

[50] Aachen-Birmingham-Bonn-Hamburg-London (I.C.)-Munich Collaboration, Nuovo Cim. $\underline{31}$, 729 (1964)

[51] I. Derado, V.P. Kenney, J.A. Poirier, W.D. Shephard, Phys. Rev. Lett. $\underline{14}$, 872 (1965)

[52] R.A. Lewis, Dissertation MIT 1966 (unpublished)

[53] W.S.C. Williams, An Introduction to Elementary Particles. Academic Press, New York, London (1961)

[54] W.P. Swanson, private communication and DESY Report 66/17 (1966)